In situ/operando spectroscopic studies on selective catalytic reduction mechanisms of NO and N_2O

(*In situ/operando* 分光法による NO と N_2O の選択還元の反応機構研究)

Qian Yucheng
銭　宇澄

2026

Graduate School of Chemical Sciences and Engineering

Hokkaido University

Contents

Chapter 1. General Introduction

1.1 Environmental issues for NOx

1.2 *In situ/operando* spectroscopic study

1.3 Modulation excitation spectroscopies

1.4 Outline of thesis

Chapter 2. Low-temperature NOx capture and reduction via NO oxidation by O_3 on Cu-CHA

2.1 Introduction

2.2 Experimental Section

2.3 Results and discussions

2.4 Conclusion

2.5 References

Chapter 3. Redox-Half-Cycle Dynamics of NH_3–SCR on Sulfate-Modified CeO_2 Revealed by Modulation-Excitation Spectroscopy

3.1 Introduction

3.2 Experimental Section

3.3 Results and discussion

3.4 Conclusion

3.5 References

Supporting information

Chapter 4. Mechanism of Selective Reduction of N_2O by CO over Fe–ß Catalysts Studied by *In-situ/Operando* Spectroscopy

4.1 Introduction

4.2 Experimental Section

4.3 Results and discussion

4.4 Conclusions

4.5 References

Supporting information

Chapter 5. General Conclusion

Acknowledgments

Chapter 1

General Introduction

1.1 Environmental issues for NOx and N_2O

The major anthropogenic source of nitrogen oxides (NOx) is the combustion of fossil fuels, such as petroleum in vehicle engines and coke in thermal power plants. NOx is emitted mainly as NO and NO_2, together with N_2O.[1–5] Although internal-combustion engines and large-scale power generation are indispensable for modern society, the associated NOx emissions cause serious air-quality problems and adverse effects on human health and ecosystems. Consequently, effective NOx abatement has become essential. At the same time, the global vehicle fleet continues to expand every year, while emission regulations become increasingly stringent (Figure 1, https://www.ascea.auto/figure/nox-emissions-from-the-eu-heavy-truck-fleet-by-euro-classes/). Exhaust-gas regulations for automobiles were first introduced in 1974, and international awareness of environmental issues has since intensified, as exemplified by the adoption of the Sustainable Development Goals (SDGs) in 2015. In Europe, the current standards “Euro 7” for light-duty vehicles stays at the same level as Euro 6, but “Euro VII” for heavy-duty vehicles, especially diesel engines, has further tighten these limits on NOx emission.[6–8] To comply with such regulations, denitrification (deNOx) technologies based on lean-burn deNOx catalysts have become the mainstream approach for removing NOx from exhaust gases.

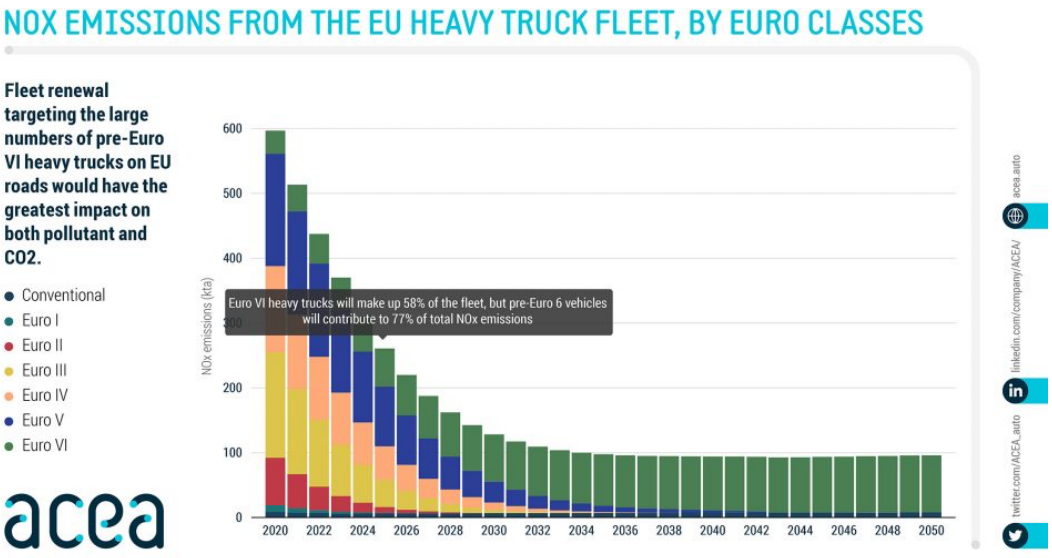

Figure 1 Aggregated fleet and NOx emissions from the EU heavy truck fleet, by Euro classes.

1.2 Selective catalytic reduction (SCR) system for DeNOx

Among these, selective catalytic reduction of NOx with NH_3 (NH_3-SCR) is widely implemented for both mobile[9–14] and stationary sources[14–18] that rely on thermal energy produced by fossil-fuel combustion. In the NH_3-SCR process, NOx is selectively converted into N_2 and H_2O according to Eq. (1-1):

$$4NH_3 + 4NO + O_2 \rightarrow 4N_2 + 6H_2O \quad (1\text{-}1)$$

Vanadium-based catalysts such as V_2O_5–WO_3/TiO_2 are typically employed in stationary deNOx systems for power plants and waste-treatment facilities, whereas Cu-exchanged CHA-type zeolites (Cu-CHA) are key components in urea-SCR systems for diesel vehicles. Despite their commercial success, these industrial catalysts were introduced with limited mechanistic understanding, and further insight into their structure–reactivity relationships is required to guide the development of next-generation deNOx technologies.

Diesel engines are widely used in automobiles and industrial machinery because of their high thermal efficiency and excellent torque characteristics. However, direct injection of diesel fuel leads to high emissions of particulate matter (PM) and NOx. Modern diesel emission control systems therefore employ a combination of a diesel oxidation catalyst (DOC), a diesel particulate filter (DPF), an NH_3-SCR catalyst, and an ammonia slip catalyst (ASC). The DOC oxidizes hydrocarbons (HC) and CO and converts part of the NO to NO_2, which strongly affects the efficiency of the downstream SCR step.[19] The first commercial application of SCR in automobiles around 2005 relied on urea-SCR and required substantial on-board urea storage. Although urea-SCR can provide high NOx removal efficiency, it also introduces challenges such as incomplete urea decomposition and potential secondary emissions (e.g., isocyanic acid). Consequently, NH_3-SCR systems have been intensively studied and optimized and are now installed in both heavy-duty vehicles and passenger cars. Cu-exchanged SSZ-13 with CHA topology is the benchmark catalyst in these systems. SSZ-13 is a small-pore zeolite (maximum ring size ≈ 3.8 Å) composed of double six-ring (d6r) units and chabazite cages. Screening studies by the Research Association of Automotive Internal Combustion Engines (AICE) demonstrated that zeolites containing d6r cages, such as CHA and AFX, show outstanding SCR activity and hydrothermal stability when exchanged with Cu, leading to their widespread adoption as diesel-deNOx catalysts.[9–12] In the

presence of equimolar NO and NO_2, the so-called fast SCR reaction (Eq. (1-2)) markedly enhances low-temperature activity:[11,17,19]

$$2NH_3 + NO + NO_2 \rightarrow 2N_2 + 3H_2O \quad (1\text{-}2)$$

At low temperatures and under NO_2-rich conditions, the behavior of Brønsted acid sites and the rapid formation of ammonium nitrate are particularly important, because these species can control N_2 selectivity and overall deNOx performance.

Similar deNOx concepts are applied to stationary sources. In thermal power plants, fuel is burnt in boilers to generate electricity, and the resulting flue gas contains NOx, SOx, and particulate matter (fly ash). This flue gas is treated by a series of environmental control units before release to the atmosphere. Typically, the exhaust gas passes through a denitration unit, where NOx is reduced in an SCR reactor, then an air preheater for heat recovery, an electrostatic precipitator for dust removal, and finally a desulfurization unit for SOx abatement before discharge through the stack. Supported vanadium(V) oxide catalysts, such as V_2O_5/TiO_2 and $V_2O_5–WO_3/TiO_2$, have been successfully employed for decades in these stationary SCR applications and remain industrial workhorses because of their robustness and tolerance to typical flue-gas compositions. [14,17,20–22]

For nitrous oxide (N_2O) is a potent greenhouse gas with a long atmospheric lifetime, making its mitigation an urgent environmental challenge across agriculture, transportation, and chemical industries. Catalytic approaches for controlling N_2O emissions from diesel exhaust include direct decomposition and selective catalytic reduction (SCR). Although Rh-based catalysts are highly active for N_2O decomposition, they require high temperatures and suffer strong inhibition by excess O_2, limiting their practical use and motivating the search for non-PGM alternatives. Fe-containing zeolites have emerged as effective catalysts for the SCR of N_2O with CO, CH_4, hydrocarbons, or NH_3 and have been widely studied as model systems for N_2O reduction. Among the few reports on CO-SCR, Fe-ß enables N_2O conversion at relatively low temperatures, while Fe-MFI with cationic Fe species shows higher O_2 tolerance owing to preferential activation of N_2O over O_2 at α-Fe sites.[23–25]

As emission regulations continue to tighten for both mobile and stationary sources, detailed elucidation of the NH_3-SCR reaction mechanism on these catalysts, and the development of new materials capable of high activity and selectivity under increasingly demanding operating conditions (e.g., cold start,

low-temperature operation, and high sulfur tolerance), are crucial for the rational design of future deNOx technologies.

1.2 *In situ/operando* spectroscopic study

Understanding how a catalyst functions requires access to its real-time structure, surface chemistry, and electronic state under working conditions. Conventional ex situ characterization often fails to capture these transient features because catalysts can restructure, change oxidation state, or form short-lived intermediates only during reaction. For this reason, *in situ/operando* spectroscopies have become indispensable tools for elucidating catalytic reaction mechanisms.[11,24,26–31]

Through tons of research papers within catalysts filed, *in situ* spectroscopies have been applied to various of different heterogeneous catalysis researches. Under real reaction conditions, monitoring adsorption and desorption is now becoming a trend in heterogeneous catalysis research. Researchers are trying to relate the reactive species with the reactivity directly to illustrate that the superior activity is due to larger number of reactive intermediates. The problems, that there being weak or few direct evidence for supporting the relation between reactive intermediates and final products, arise when lacking *operando* results.

When it comes to the products monitoring, few efforts have been devoted to it. The *operando* measurements give a clear insight into the reaction itself and what is happening over catalysts. People spent years applying *in situ* spectroscopies to tracking the possible intermediates under reaction conditions. It is also important to know how the intermediates turn into the products. Thus, *operando*, which allows people to measure spectroscopies and reaction simultaneously, become crucial for figuring out how reaction occurs over catalysts surface and is still insufficient.[32,33]

By monitoring catalysts under realistic gas-phase environments, these techniques provide time-resolved insight into the dynamic interplay between structure and reactivity. Our group has utilized *in situ/operando* approach, especially with FTIR, to reveal reaction mechanisms and design novel catalysts. In our previous study, *in situ/operando* FTIR was applied to revel the NH_3—SCR over Fe-zeolite. The key intermediate, NO^+, was formed via HONO utilizing Fe^{3+}-OH and Bronsted acid sites. The formed NO^+ reacts with NH_3 to produce nitrosamide (H_2NNO), which is observed by *in situ* FTIR, and its decomposition into N_2 and H_2O monitored by mass spectrometry (MS).[26] Similar studies were

conducted over H-CHA, Cu-CHA, Rh-BEA, WOx/CeO_2 and P/CeO_2.[11,27,29,31–35] Moreover, *in situ/operando* spectroscopy can relate the states of redox center with the products. Our group recently applied XAS and UV-Vis to figure out the relationship between redox center and reactivity. This approach gives the redox cycle of P/CeO_2 between Ce^{4+} and Ce^{3+}, showing that the NO + NH_3 are reducing Ce^{4+}, giving Ce^{3+} and NO^+, which then turned into NH_4NO_2. And the N_2 formation is observed as Ce^{4+} is being reduced.[32]

Combing various means of spectroscopies, *in situ/operando* measurements can give not only fundamental reactions of adsorbed intermediates but also the dynamic change of active sites. These reported studies emphasize importance of developing *in situ/operando* spectroscopies and it potential of unraveling the indeterminate reaction mechanisms. Thus, there is an urgent need for further development and wider application of *in situ/operando* spectroscopies for variety of catalytic reaction.

When these operando observations are integrated with density functional theory (DFT) calculations and *ab initio* thermodynamics, the experimental signatures can be assigned to specific molecular structures and elementary steps, providing a coherent and mechanistic picture of the reaction network.

Together, these *in situ/operando* approaches enable researchers to uncover how catalysts respond to their environment, which intermediates control activity, and which structural motifs govern selectivity—insights that are inaccessible by static, *ex situ* characterization. As such, they play a critical role in guiding the rational design of next-generation catalytic materials.

1.3 Modulation excitation spectroscopies

Among the *in situ/operando* method, the reaction conditions, however, make it hard to observe the adsorption, desorption and products formation simultaneously, causing the crowded spectra which is hard to interpret. Meanwhile, the active species are usually generated in small quantities, making it even harder to observe. Therefore, a new, powerful, highly sensitive spectroscopic tools should be developed and utilized for heterogeneous catalyst researches.[36,37]

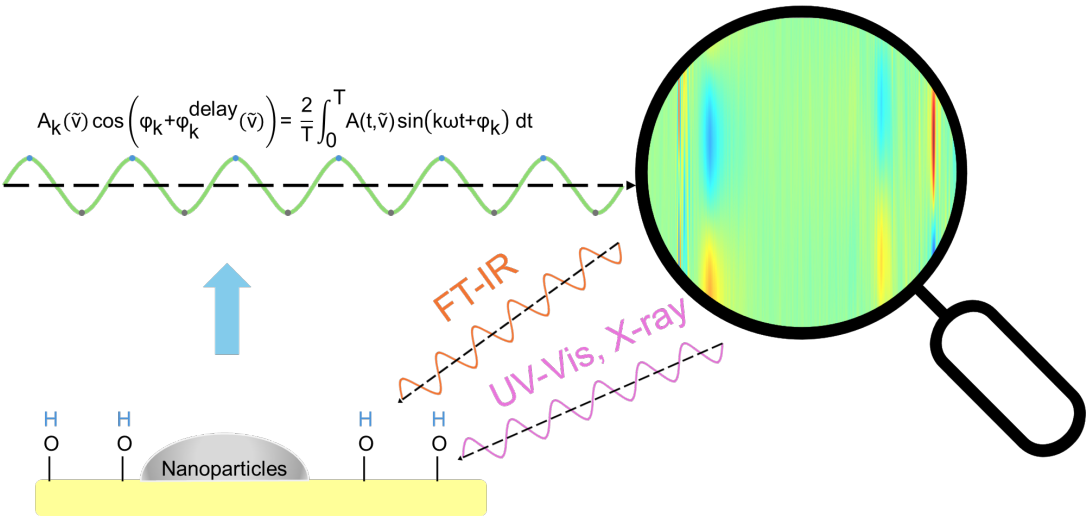

Figure 2 Scheme of modulation excitation spectroscopy (MES) used in this thesis.

Modulation Excitation (ME) spectroscopy (Figure 2) is a powerful method for probing the dynamic behavior of reactive intermediates involved in catalytic processes. By periodically perturbing the reaction environment—such as by alternating reactant concentrations—ME highlights species that respond synchronously to the stimulus. When combined with diffuse reflectance infrared Fourier transform spectroscopy (DRIFTS), the resulting ME-DRIFTS technique makes it possible to selectively extract the spectral features of active, reaction-coupled species, while suppressing signals from spectator or inactive surface species.[37–44]

Phase-sensitive detection (PSD) converts the time-domain response into phase-resolved spectra, isolating bands that track the imposed modulation. This greatly enhances the visibility of short-lived intermediates and transient surface species, offering insight that is difficult to obtain from steady-state measurements alone. ME-DRIFTS has been widely applied to a variety of catalytic systems to monitor intermediate formation, transformation, and decay under realistic conditions, demonstrating its utility as a general tool for unraveling the mechanistic steps of heterogeneous reactions.

Although, the combination of ME and DRIFTS has been introduced and applied for a while. The researches that apply ME-DRIFTS is still minority among millions of *in situ* spectroscopic studies.[36,43] Our group has published 2 papers that use modulation excitation spectroscopies.[18,33] For WOx/CeO_2, with the help of ME-DRIFTS, the covered intermediate, NO^+, is directly observed and the formation

sequence of reactive intermediate is also revealed. The results indicate clearer and more detailed reaction mechanisms by ME-DRIFTS than normal *in situ* spectroscopies. But still, these papers all focused on ME-DRIFTS. The need to develop new MES approaches arise as for heterogeneous catalysis, the characterization method varies when studying different materials. Hence, this research will continue expanding the application of ME for different spectroscopies such as UV-Vis and X-ray adsorption.

1.4 Outline of thesis

Combing the issue of NOx and N_2O with *in situ/operando* spectroscopies together, this emphasizes the necessity and possibility of mechanistic studies for SCR of NO and N_2O utilizing cutting-edge *in situ/operando* and modulation excitation spectroscopies.

Therefore, this thesis aims at the mechanistic study of SCR for 1) NO over Cu-CHA with O_3 assistance, 2) NO over CeO_2 supported sulfur catalyst and 3) N_2O over Fe-ß catalyst with CO utilizing *in situ/operando* spectroscopies and modulation excitation spectroscopies.

Chapter 2 presents the transient reduction of NOx with NH_3 over Cu-exchanged CHA zeolite (Cu-CHA) assisted by the catalyst-free oxidation of NO by O_3 investigated by applying *in situ/operando* spectroscopies to enhance the low temperature reactivity of Cu-CHA. The room-temperature catalyst-free oxidation of NO by O_3 yielded NO_2 at low O_3/NO ratio and N_2O_5 as the main product at higher ratios. DFT calculations verified the reaction of NO_2 + O_3 to N_2O_5 proceeding with low activation energies. Transient operando IR measurements demonstrated that Cu-CHA exposure to NO + O_3 at 100 °C resulted in the storage of NOx as NO_3^- on the Cu^{2+} site. The stored NOx reacted with NH_3 to yield N_2 and NH_4NO_3. Preabsorbed NH_3 on Cu-CHA was oxidized by O_3 to yield N_2 and N_2O. The reaction of preabsorbed NH_3 with NO+O_3 caused the selective formation of N_2. The obtained results may aid in developing a new O_3-assisted unsteady-state lean De-NOx process involving reactions of captured NOx with NH_3 or reduction of NOx with stored NH_3.

Chapter 3 presents a comprehensive investigation into the active sites and reaction mechanism of the selective catalytic reduction of NO by NH_3 (NH_3−SCR)

over sulfate-loaded ceria (S1/CeO_2) utilizing *in situ/operando* spectroscopies and modulation excitation spectroscopies along with computational methods. Catalyst characterization and density functional theory (DFT) calculations reveal that SO_4^{2-} and $S_2O_7^{2-}$species are the dominant sulfate species on the S1/CeO_2 catalysts under the experimental conditions. The reduction/oxidation half-cycles (RHC/OHC) were investigated using modulation excitation in situ X-ray absorption near-edge structure (XANES) at the Ce *L*3-edge, ultraviolet-visible (UV-Vis), and infrared (IR) spectroscopies, along with online analysis of outlet products (operando spectroscopy). The $Ce^{4+}(OH^-)$ species, possibly located adjacent to sulfate species, are reduced by NO + NH_3 to produce N_2, H_2O, and Ce^{3+} species through an NO^+ intermediate (RHC). The Ce^{3+} species are subsequently reoxidized by O_2 (OHC). The results from IR spectroscopy suggest that the RHC begins with the reaction between NO and $Ce^{4+}(OH^-)$, initially generating NO^+, followed by the formation of Ce^{3+} and gaseous HONO. The HONO then reacts with NH_3 to produce N_2 and H_2O via NH_4NO_2 intermediates.

Chapter 4 presents that selective reduction of N_2O by CO under excess O_2 was effectively catalyzed by Fe(0.9 wt%)-exchanged ß zeolite (Fe0.9ß) in the temperature range of 250–500 °C. Kinetic experiments showed that the activation energy for N_2O reduction with CO was lower than that for the direct N_2O decomposition, and the rate of N_2O reduction with CO at 300 °C was 16 times higher than that for direct N_2O decomposition. Reaction order analyses showed that CO and N_2O were involved in the kinetically important step, while O_2 was not involved in the important step. At 300 °C, the rate of CO oxidation with 0.1% N_2O was two times higher than that of CO oxidation with 10% O_2. This quantitatively demonstrates the preferential oxidation of CO by N_2O under excess O_2 over Fe0.9ß. *Operando/in-situ* diffuse reflectance UV-vis spectroscopy showed a redox-based catalytic cycle; α-Fe-O species are reduced by CO to give CO_2 and reduced Fe species, which are then re-oxidized by N_2O to regenerate the α-Fe-O species. The initial rate for the regeneration of α-Fe-O species under 0.1% N_2O was four times higher than that under 10% O_2. This result shows quantitative evidence on the higher reactivity of N_2O than O_2 for the regeneration of α-Fe-O intermediates, providing a fundamental reason why the Fe0.9ß catalyst selectively promotes the CO + N_2O reaction under excess O_2 rather than the undesired side reaction of CO + O_2. The mechanistic model was verified by the results of *in-situ* Fe K-edge X-ray absorption spectroscopy.

Chapter 5 is the general summary. Throughout the thesis, I have developed and utilized rational design of deNOx catalysts based on the mechanistic study from *in situ/operando* and modulation excitation spectroscopies combined with DFT calculations. This set of mechanistic study allows me to get a molecular level insights into the SCR reaction mechanism and gives essential and important guidance for the design and development of novel catalysts.

(1) Roy, S.; Hegde, M. S.; Madras, G. *Appl. Energy* **2009**, *86* (11), 2283–2297.
(2) Skalska, K.; Miller, J. S.; Ledakowicz, S. *Sci. Total Environ.* **2010**, *408* (19), 3976–3989.
(3) Si, M.; Shen, B.; Adwek, G.; Xiong, L.; Liu, L.; Yuan, P.; Gao, H.; Liang, C.; Guo, Q. *J. Environ. Sci. (China)* **2021**, *101*, 49–71.
(4) Beale, A. M.; Gao, F.; Lezcano-Gonzalez, I.; Peden, C. H. F.; Szanyi, J. *Chem. Soc. Rev.* **2015**, *44* (20), 7371–7405.
(5) Leverett, J.; Lie, W. H.; Khan, M. H. A.; Ma, Z.; Daiyan, R.; Amal, R. *Sustain. Energy Fuels.* **2025**, *9* (14), 3780–3790.
(6) Mulholland, E.; Miller, J.; Bernard, Y.; Lee, K.; Rodríguez, F. *Transp. Eng.* **2022**, *9*, 100133.
(7) Mądziel, M.; Mądziel, M. *Energies (Basel)* **2025**, *18* (21), 5853.
(8) Zhang, Z.; Hu, J.; Yang, D.; Yin, Z.; Lu, K.; Tan, D. *Energy* **2024**, *303*, 131955.
(9) Shibata, G.; Eijima, W.; Koiwai, R.; Shimizu, K; Nakasaka, Y.; Kobashi, Y.; Kubota, Y.; Ogura, M.; Kusaka, J. *Catal. Today* **2019**, *332*, 59–63.
(10) Qian, Y.; Yasumura, S.; Mine, S.; Toyao, T.; Shimizu, K. *Appl. Catal. Gen.* **2023**, *655*, 119099.
(11) Liu, C.; Malta, G.; Kubota, H.; Toyao, T.; Maeno, Z.; Shimizu, K. *J. Phys. Chem. C* **2021**, *125* (40), 21975–21987.
(12) Yasumura, S.; Kato, T.; Qian, Y.; Toyao, T.; Shimizu, K. *J. Phys. Chem. C* **2024**, *128* (31), 12949–12959.
(13) Priya, S. V.; Ohnishi, T.; Shimada, Y.; Kubota, Y.; Masuda, T.; Nakasaka, Y.; Matsukata, M.; Itabashi, K.; Okubo, T.; Sano, T.; Tsunoji, N.; Yokoi, T.; Ogura, M. *Bull. Chem. Soc. Jpn.* **2018**, *91* (3), 355–361.
(14) Kubota, H.; Toyao, T.; Maeno, Z.; Inomata, Y.; Murayama, T.; Nakazawa, N.; Inagaki, S.; Kubota, Y.; Shimizu, K. *ACS Catal.* **2021**, *11* (17), 11180–11192.
(15) Wang, D.; Chen, Q.; Zhang, X.; Gao, C.; Wang, B.; Huang, X.; Peng, Y.; Li, J.; Lu, C.; Crittenden, J. *Environ. Sci. Technol.* **2021**, *55* (5), 2743–2766.
(16) Xie, Q.; Cai, Y.; Zhang, L.; Hu, Z.; Li, T.; Wang, X.; Zeng, Q.; Wang, X.; Sun, J.; Dong, L. *J. Phys. Chem. C* **2021**, *125* (40), 21964–21974.
(17) Koebel, M.; Madia, G.; Raimondi, F.; Wokaun, A. *J. Catal.* **2002**, *209* (1), 159–165.
(18) Kubota, H.; Qian, Y.; Mine, S.; Toyao, T.; Nuguid, R. J. G.; Buttignol, F.; Ferri, D.; Shimizu, K. *ChemCatChem* **2025**, *17* (4), e202401839.

(19) Ciardelli, C.; Nova, I.; Tronconi, E.; Chatterjee, D.; Bandl-Konrad, B.; Weibel, M.; Krutzsch, B. *Appl. Catal., B Environ.* **2007**, *70* (1–4), 80–90.
(20) Dumesic, J. A.; Topsøe, N. Y.; Topsøe, H.; Chen, Y.; Slabiak, T. *J. Catal.* **1996**, *163* (2), 409–417.
(21) Wachs, I. E. *Dalton Trans.* **2013**, *42* (33), 11762–11769.
(22) Inomata, Y.; Kubota, H.; Hata, S.; Kiyonaga, E.; Morita, K.; Yoshida, K.; Sakaguchi, N.; Toyao, T.; Shimizu, K.; Ishikawa, S.; Ueda, W.; Haruta, M.; Murayama, T. *Nat. Commun* **2021**, *12* (1).
(23) Zhang, N.; He, C.; Jing, Y.; Qian, Y.; Toyao, T.; Shimizu, K. *S&I* **2024**, *46*, 104120.
(24) Qian, Y.; Yasumura, S.; Zhang, N.; Anzai, A.; Toyao, T.; Shimizu, K. *CHINESE J CATAL.* **2025**, *69*, 185–192.
(25) Zhang, N.; He, C.; Jing, Y.; Qian, Y.; Obuchi, M.; Toyoshima, R.; Kondoh, H.; Oka, K.; Wu, B.; Li, L.; Anzai, A.; Toyao, T.; Shimizu, K. *Environ. Sci. Technol.* **2025**, *59* (3), 1598–1607.
(26) Yasumura, S.; Qian, Y.; Kato, T.; Mine, S.; Toyao, T.; Maeno, Z.; Shimizu, K. *ACS Catal.* **2022**, *12* (16), 9983–9993.
(27) Liu, C.; Kubota, H.; Amada, T.; Kon, K.; Toyao, T.; Maeno, Z.; Ueda, K.; Ohyama, J.; Satsuma, A.; Tanigawa, T.; Tsunoji, N.; Sano, T.; Shimizu, K. *ChemCatChem* **2020**, *12* (11), 3050–3059.
(28) Sun, C.; Zhao, N.; Zhuang, Z.; Wang, H.; Liu, Y.; Weng, X.; Wu, Z. *J. Hazard. Mater.* **2014**, *274*, 376–383.
(29) Liu, C.; Malta, G.; Kubota, H.; Kon, K.; Toyao, T.; Maeno, Z.; Shimizu, K. *J. Phys. Chem. C* **2021**, *125* (25), 13889–13899.
(30) Yasumura, S.; Qian, Y.; Toyao, T.; Maeno, Z.; Shimizu, K. *J. Phys. Chem. C* **2022**, *126* (27), 11082–11090.
(31) Yasumura, S.; Kato, T.; Qian, Y.; Toyao, T.; Maeno, Z.; Shimizu, K. *J. Phys. Chem. C* **2022**, *126* (45), 19147–19158.
(32) Zhang, N.; Tong, J.; Miyazaki, S.; Zhao, S.; Kubota, H.; Jing, Y.; Mine, S.; Toyao, T.; Shimizu, K. *Environ. Sci. Technol* **2023**, *57* (43), 16289–16295.
(33) Kubota, H.; Jing, Y.; Wan, L.; Tong, J.; Zhang, N.; Mine, S.; Toyao, T.; Toyoshima, R.; Kondoh, H.; Ferri, D.; Shimizu, K. *ACS Catal.* **2023**, *13* (13), 9274–9288.
(34) Marberger, A.; Petrov, A. W.; Steiger, P.; Elsener, M.; Kröcher, O.; Nachtegaal, M.; Ferri, D. *Nat. Catal.* **2018**, *1* (3), 221–227.
(35) Nuguid, R. J. G.; Ferri, D.; Marberger, A.; Nachtegaal, M.; Kröcher, O. *ACS*

Catal. **2019**, *9* (8), 6814–6820.

(36) Nuguid, R. J. G.; Elsener, M.; Ferri, D.; Kröcher, O. *Appl. Catal. B: Environ.* **2021**, *298*, 120629.

(37) Müller, P.; Hermans, I. *Ind. Eng. Chem. Res.* **2017**, *56* (5), 1123–1136.

(38) Ferri, D.; Newton, M. A.; Nachtegaal, M. *Top. Catal.* **2011**, *54* (16–18), 1070–1078.

(39) Greenaway, A. G.; Marberger, A.; Thetford, A.; Lezcano-González, I.; Agote-Arán, M.; Nachtegaal, M.; Ferri, D.; Kröcher, O.; Catlow, C. R. A.; Beale, A. M. *Chem. Sci.* **2020**, *11* (2), 447–455.

(40) Urakawa, A.; Bürgi, T.; Baiker, A. *Chem. Eng. Sci.* **2008**, *63* (20), 4902–4909.

(41) Kubota, H.; Qian, Y.; Mine, S.; Toyao, T.; Nuguid, R. J. G.; Buttignol, F.; Ferri, D.; Shimizu, K. *ChemCatChem* **2025**, *17* (4), e202401839.

Chapter 2

Low-temperature NOx capture and reduction via NO oxidation by O_3 on Cu-CHA

2.1 Introduction

The ammonia selective catalytic reduction (NH_3–SCR) of nitrogen oxides (NOx) using Cu-exchanged chabazite (Cu-CHA) catalysts is widely used for NOx removal in diesel emission control systems [1–7]. A commercial NH_3–SCR system with Cu-CHA exhibits low NO_X conversion under engine cold start conditions (<150 °C)[8,9]. The reduction of a NO_2/NO (1/1) mixture by NH_3, known as fast SCR, can provide high NOx conversion at low temperatures. Further, new NH_3–SCR technologies combined with NOx adsorbers, such as passive NOx adsorbers (PNAs) [10], adsorption+SCR (AdSCR) [11,12], and NOx storage and reduction (NSR) coupled with SCR (NSR–SCR) [13–16], have been studied for low-temperature diesel NOx reduction below 150 °C. However, the conversion efficiency of NOx is low below 100 °C, which results in high NOx emissions, particularly under cold start conditions. To improve NOx conversion under transient cold start conditions, a new NOx adsorption-assisted SCR system that can reduce (or capture) NOx below 100 °C must be developed. However, this is a challenging research objective.

Numerous studies have comprehensively investigated the reaction mechanism of NH_3–SCR over Cu-CHA[17]. In previous studies, the mechanism of NH_3–SCR was investigated in depth by *in situ*/*operando* spectroscopy. The standard SCR mechanism is composed of a reduction half-cycle (RHC) and an oxidation half-cycle (OHC). Cu^{2+} is reduced by NO+NH_3 to yield Cu^+, N_2, and H_2O in the RHC, which is followed by the re-oxidation of Cu^+ to Cu^{2+} in the OHC [18,19]. Our group employed *in situ*/*operando* IR spectroscopy and density functional theory (DFT) calculations to reveal the mechanism of standard [20,21] and fast SCR [22] reactions on Cu-CHA and reported low-temperature (<100 °C) N_2 formation via transient reactions of adsorbed NO_2 with NH_3. NO is oxidized by ozone (O_3) under catalyst-free conditions at room temperature [23–28]. Previously, in the presence of metal oxides under flowing NO+O_3, the oxidation of NO by O_3 allowed for the preparation of mixtures with variable concentrations of NO, NO_2, and N_2O_5, which were then adsorbed onto the catalyst [29].

Based on this background, we hypothesize that a new transient De-NOx system could be developed by combining gas-phase NO oxidation by O_3 and the transient reaction of adsorbed NOx on Cu-CHA below 100 °C. Herein, we report the results of an *in situ*/*operando* IR spectroscopic study conducted on the formation of adsorbed NOx species on Cu-CHA under NO+O_3. The thermal desorption and reaction of the adsorbed NOx species with NH_3 and the reaction

of adsorbed NH_3 with O_3 or $NO+O_3$ were also studied. The results of this study suggest the feasibility of O_3-assisted unsteady-state SCR using Cu-CHA catalysts.

2.2 Experimental Section

2.2.1 Catalyst preparation

H^+-form CHA (H-CHA) was prepared by calcining (600 °C, 3 h, air) NH_4^+-form CHA (Tosoh, Si/Al = 12.8). The method used to prepare Cu-exchanged CHA with a Cu/Al ratio of 0.42 (Si/Al = 12.8) is detailed in our previous report [19].

2.2.2 *In situ/operando* FTIR spectroscopic experiments

In situ/operando IR spectra were recorded in the transmission mode using a JASCO FT/IR-4100 spectrometer (TGS, accumulating 20 scans at a resolution of 4 cm^{-1}). Cu-CHA powder was pelletized into a 40 mg self-supporting thin wafer and placed inside a quartz IR cell (CaF_2 window) connected to a flow system (total flow: 100 mL min^{-1}). The standard gas composition was 0.1% NO, 0.1% NH_3, and 10% O_2 under a He flow. O_3 was fed to the system by passing the O_2 flow through an ozonizer (F0G-AC5G, EcoDesign Inc.) placed before the mainstream. A reference spectrum of the Cu-CHA wafer pretreated under 10% O_2 at 500 °C was recorded under He at the temperature of *in situ* measurements. The difference spectra of the adsorbed species were recorded as functions of the reaction time. The concentrations of NO, NO_2, NH_3, N_2O, and O_3 in the outlet gas line were monitored using an online IR spectrometer (JASCO FT/IR-4100 with a gas cell). N_2 (m/z = 28) was monitored using a mass spectrometer (JMS-Q1500GS, JEOL Ltd.). The gas cell (IR) sensitivity of O_3 was calibrated using an O_3 analyzer (EG-550, EcoDesign Inc.).

2.2.3 Computational details

Reaction route mapping was conducted using the SC-AFIR method implemented in the GRRM17 program [30]. A model collision energy parameter of 1000 kJ mol^{-1} was used to explore the reaction route. Path top (PT) points were obtained using the locally updated plane (LUP) method and subsequently re-optimized by the following intrinsic reaction coordinate (IRC) calculation to determine the transition state (TS) structures and their connectivity[31]. All atoms in the system were treated as target atoms. First, geometry optimization was performed using the GFN2-xTB method [32] with an electronic temperature of 1000 K, an integral cutoff of 0.25×10^2, an SCF convergence of 0.1×10^{-5} Ha, and a wavefunction convergence of

0.1 × 10^{-3} e to obtain a rough reaction map. Subsequently, the “RePATH” keyword in the GRRM17 program was used to refine the obtained reaction route by the Gaussian16 program [33] and improve the accuracy of the geometry optimization. The stability of the molecular orbital was checked using the “Stable = Opt” keyword in the GRRM17 program. Spin-unrestricted DFT calculations were performed using the B3LYP functional [34,35] with the 6-311G** basis set. The spin multiplicity of the system was set to be a singlet. The obtained reaction route was determined using Cytoscape software [36].

2.3 Results and Discussion

2.3.1 Gas-phase reaction

Following previous reports on the gas-phase oxidation of NO by O_3 [23–26,37], we first performed gas cell (IR) analysis on the gas-phase product for the oxidation of 0.2% NO by O_3 at different concentrations (0.1%, 0.2%, 0.3%, and 0.5%) under catalyst-free conditions at room temperature (25 °C).

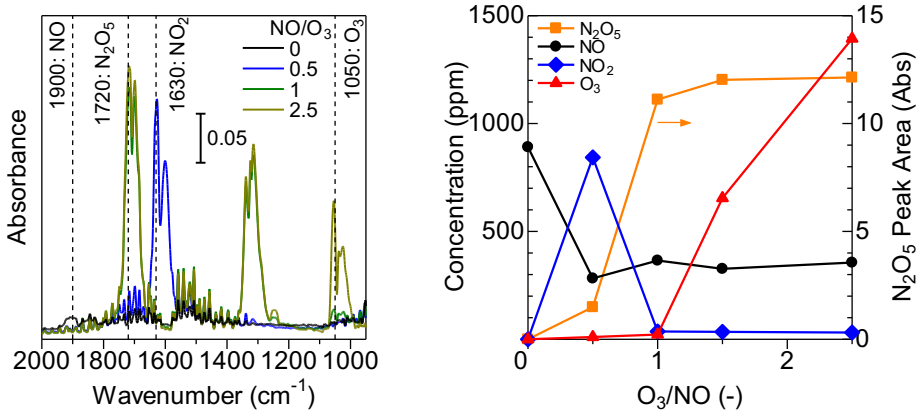

Figure 1. IR spectra (left) of gas-phase products under different NO/O_3 ratios for the gas-phase (catalyst-free) oxidation of NO (0.2%) by O_3 (0.1%, 0.2%, 0.3%, and 0.5%) (total flow: 100 mL min^{-1}). Concentrations of NO, NO_2, and O_3 and the IR peak area of N_2O_5 versus the O_3/NO ratio (right).

As shown in Figure 1, the amounts of NO_2 and N_2O_5 produced depend on the O_3/NO ratio. The O_3/NO ratio of 0.5 produced the highest NO_2 concentration. At

higher O_3/NO ratios, N_2O_5 is the main product[38]. NO_2 formation is described by reaction (1).

$$NO + O_3 \rightarrow NO_2 + O_2 \quad (1)$$

Our previous DFT study [39] showed that reaction (1) is a barrierless process, indicating that the gas-phase (catalyst-free) oxidation of NO with O_3 can occur even at room temperature. To investigate the mechanism of N_2O_5 formation in the presence of O_3, we performed DFT calculations using the SC-AFIR method. As shown in Figure 2, NO_2 can react with O_3 to produce N_2O_5 with a low barrier, in accordance with our experimental observations. The plausible reactions are as follows.

$$2NO_2 + O_3 \rightarrow NO_2 + NO_3 + O_2 \quad (2)$$

$$NO_2 + NO_3 + O_2 \rightarrow N_2O_5 + O_2 \quad (3)$$

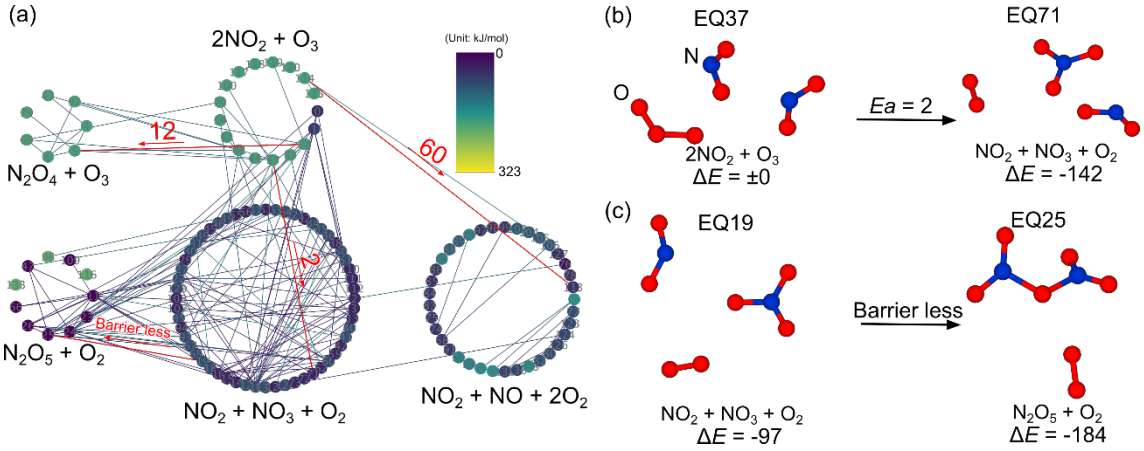

Figure 2. (a) Reaction route network for $2NO_2$+O_3 without the catalyst. Nodes and edges describe obtained structures and paths connecting them (TS and PT, determined by GRRM program). The node and edge colors describe the relative energy (the color bar is shown on the left side). The structures of plausible reaction routes for (b) $2NO_2 + O_3 \rightarrow NO_2 + NO_3 + O_2$ and (c) $NO_2 + NO_3 + O_2 \rightarrow N_2O_5 + O_2$.

As shown in Figure 2b, the activation energies of reactions (2) and (3) are below 2 kJ mol^{-1}, which is considerably lower than those of other possible reactions, such as $2NO_2 + O_3 \rightarrow NO_2 + NO + 2O_2$ (60 kJ mol^{-1}) and $2NO_2 + O_3 \rightarrow N_2O_4 + O_3$ (12 kJ mol^{-1}). Figure 2c shows a barrierless way of forming N_2O_5 from NO_2 and NO_3. The entire reaction route from NO_2 to N_2O_5 requires very low energy to overcome these barriers. The gas-phase reaction of NO_2 with excess O_3 resulted in the formation of N_2O_5 via the NO_3 intermediate.

2.3.2 Identification of adsorbed NOx species under NO+O_3

To identify the adsorbed NOx species on Cu-CHA under flowing NO+O_3, the IR spectrum of adsorbed species was obtained after exposure of the IR disk to a flow of 0.1% NO + 0.7% O_3 + 10% O_2 at 100 °C for 4000 s. The spectrum (blue line in Figure 3A) shows a strong band at 1610–1625 cm^{-1} and a peak at 1570 cm^{-1} attributed to chelating bidentate nitrate (NO_3^-) on Cu^{2+} sites [40]. A band at 1674 cm^{-1} assignable to adsorbed HNO_3 (HNO_{3ad}) and another at 1320 cm^{-1} ascribed to monodentate NO_3^- are also observed. Note that bands around 2220 cm^{-1} originating from NO^+ species were not observed (the result is not shown). These results indicate the formation of NO_3^- on Cu^{2+} sites as the main NOx species and HNO_{3ad} as a minor species. Subsequently, after purging with 10% O_2 (600 s), we conducted temperature-programmed desorption (TPD) experiments (temperature ramping rate = 20 °C min^{-1}) from 30 °C under 10% O_2. Simultaneously, we monitored the *in situ* IR spectra of adsorbed species and concentrations of NO and NO_2 in the effluent gas mixture by another IR with a gas cell at the downstream (*operando* IR measurement). Representative IR spectra are shown in Figure 3A, and the temperature dependence of the relative amounts of adsorbed species (NO_3^- and HNO_{3ad}) and TPD profiles for desorbed NO/NO_2 are illustrated in Figure 3B. The HNO_{3ad} species decomposed below 150 °C, whereas NO_3^- on the Cu^{2+} sites was stable below 250 °C. Above 350 °C, the amount of NO_3^- species decreased with temperature, accompanying the formation of NO_2. This indicates that the decomposition of NO_3^- on the Cu^{2+} sites resulted in the formation of NO_2.

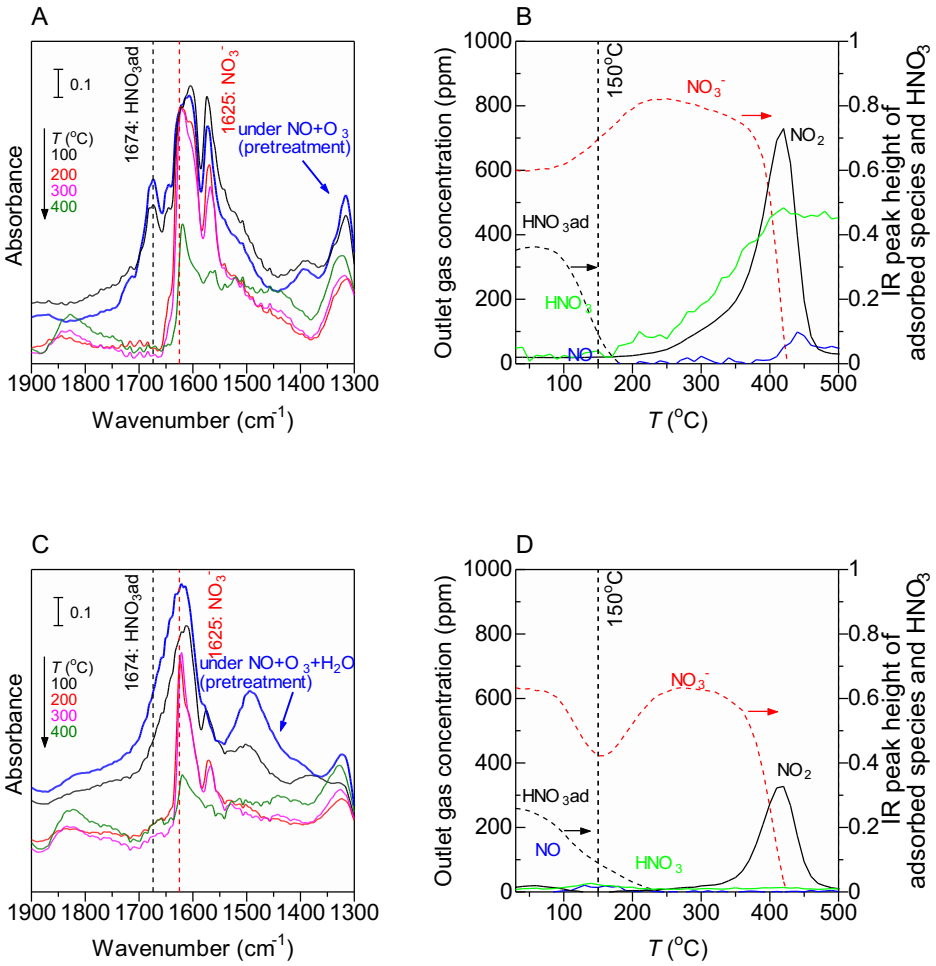

Figure 3. TPD of adsorbed NOx species on Cu-CHA under 10% O_2: (A), (C) IR spectra of adsorbed species and (B), (D) temperature dependence of the IR peak height and TPD curves for disorbed NO/NO_2. The IR disk was pre-exposed to (A), (B) 0.1% NO + 0.7% O_3 + 10% O_2 or (C), (D) 0.1% NO + 0.7% O_3 + 10% O_2 + 1% H_2O at 100 °C (4000 s), followed by purging with 10% O_2 (600 s).

The same experiment was conducted in the presence of 1% H_2O during the NOx storage period under NO+O_3, which was followed by the TPD of adsorbed NOx under dry conditions. The IR spectrum after flowing NO+O_3 for 4000 s (blue line in Figure 3C) shows bands assignable to chelating bidentate nitrate (NO_3^-) on Cu^{2+} sites (1625 and 1570 cm^{-1}) and a band assignable to HNO_{3ad} (1674 cm^{-1}). Results of the TPD experiment (Figure 3D) show that there is a decrease at the peak height of 1625 cm^{-1}, which may have originated from the desorption of H_2O rather than NO_3^- decomposition. Over 300 °C, NO_3^- on

Cu^{2+} decreases with increasing temperature, accompanying the formation of NO_2. However, the amount of NO_2 produced is considerably lower than that produced under dry conditions. This indicates that compared with the $NO+O_3+H_2O$ condition, the $NO+O_3$ condition has a higher NOx storage amount and releases more NO_2 when heated. Thus, we selected $NO+O_3$ as the standard condition for the following experiments.

The low-temperature adsorption of NOx on Cu-CHA and its desorption at high temperatures could be applied to unsteady-state lean De-NOx. NOx, which is adsorbed onto Cu-CHA at low temperatures, is desorbed at high temperatures, where the Cu-CHA catalyst can reduce the released NOx in the presence of NH_3 (NH_3–SCR).

2.3.3 Reaction of stored NOx species with NH_3

The reactions of the adsorbed NOx species, formed by the $NO+O_3$ reaction, with NH_3 were investigated via *in situ* IR combined with gas-phase analysis by mass spectrometry (MS). At 100 °C, the IR disk of Cu-CHA was first subjected to a flow of 0.16% NO + 0.08% O_3 for 15 min, which was followed by purging with He for 15 min. Thereafter, a flow of 0.1% NH_3 was introduced into the IR cell while monitoring the IR spectra of the adsorbed species and the outlet gas components (N_2 by MS and N_2O by IR with a gas cell (Figure 4)). After subjecting the catalyst to NH_3 for 200 s, the IR peak originating from NO_3^- (1625 cm^{-1}) decreased, and the IR band at 1450 cm^{-1} originating from NH_3 adsorbed on the Brønsted acid sites (BASs), NH_4^+ [41–43], appeared. The evolution of N_2 was accompanied by the consumption of adsorbed NO_3^-. Peaks of NO_3^- and NH_4^+ were observed after N_2 generation. The results show that the NO_3^- species reacts with NH_3 to yield N_2, according to reaction (4).

$$2NH_3 + 2NO_2 \rightarrow N_2 + H_2O + NH_4NO_3 \quad (4)$$

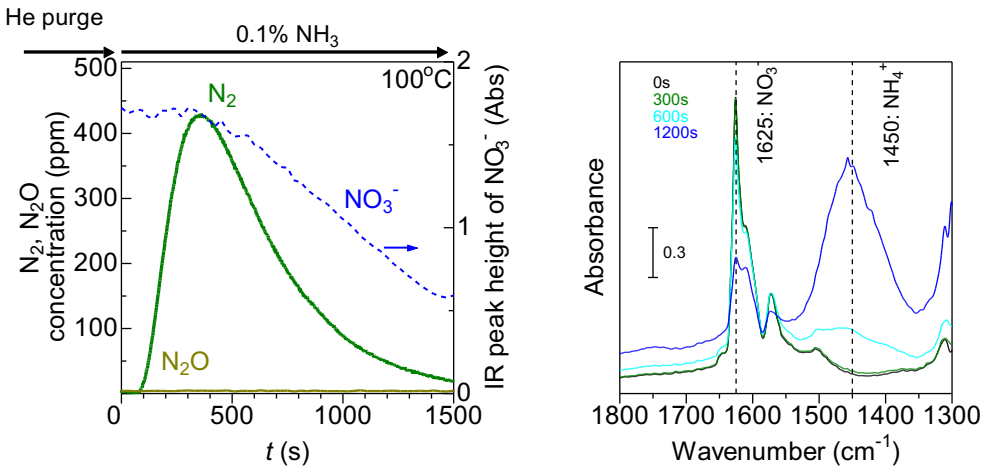

Figure 4. Concentration of outlet N_2 and N_2O on Cu-CHA at 100 °C under 0.1% NH_3; IR peak height of adsorbed NO_3^- (left) and IR spectra of adsorbed species (right). The IR disk was pre-exposed to 0.16% NO + 0.08% O_3 (900 s) at 100 °C.

NO and NO_2 desorption was not observed under NH_3 flow, indicating that the captured NOx on Cu-CHA was selectively converted to N_2 and ammonium nitrate (NH_4NO_3) without NOx desorption. N_2O was not observed, indicating that the oxidation of NH_3 to N_2O did not occur [44]. The temperature-programmed surface reaction (TPSR) of the adsorbed NO_3^- under NH_3 was also conducted after exposure of Cu-CHA to NO+O_3 (Figure 5). Two N_2 formation peaks at 160 °C (in the range of 60–210 °C) and 330 °C (in the range of 260–440 °C), accompanied by a decrease in the NO_3^- IR peak intensity, can be observed. The first N_2 generation peak at 160 °C, only minor NO_3^- truing into NO_2, can be attributed to reaction (4), where NO_3^- primarily reacts with NH_3 to yield NH_4NO_3. The second peak, accompanied by N_2O formation, might be attributable to the decomposition of NH_4NO_3 [45].

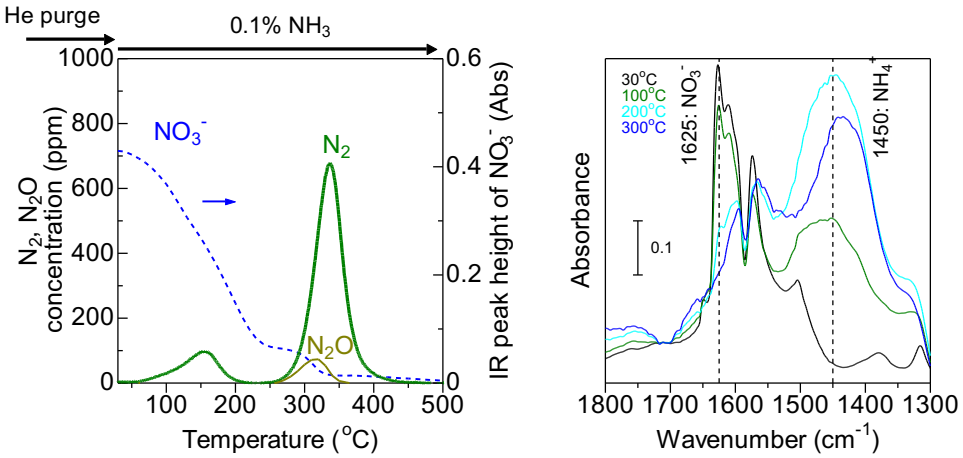

Figure 5. TPSR of adsorbed NOx (20 °C min^{-1}) (from 30 °C) under 0.1% NH_3 over Cu-CHA; TPSR profile (left) and IR spectra of adsorbed species (right). The IR disk was pre-exposed to 0.16% NO and 0.08% O_3 (900 s) at 100 °C.

2.3.4 Reaction of NH_4NO_3 with NO over Cu-CHA

The IR disk of Cu-CHA was exposed to 0.16% NO + 0.08% O_3 (900 s) and then to He and 0.1% NH_3 (900 s) and He (600 s) at 50 °C. IR peaks corresponding to adsorbed NO_3^- and NH_4^+ were observed. The relatively strong intensity of the band due to NH_4^+ suggests that NH_4NO_3 and NH_4^+ were present in the Cu-CHA. These IR peaks were stable during purging with He, suggesting that the NH_4NO_3 and NH_4^+ species were stable. Based on our previous observations of NH_4NO_3 in Cu-CHA reacting with NO to produce N_2 (reaction (5)) [22] and NH_4^+ in Cu-CHA reacting with NO to yield N_2 (reaction (6)) [19], we conducted the TPSR of adsorbed species under NO.

$$NH_4NO_3 + NO \rightarrow N_2 + NO_2 + 2H_2O \quad (5)$$

$$NH_{3ad} + NO + Cu^{II} - OH \rightarrow N_2 + 2H_2O + Cu^{I} \quad (6)$$

The TPSR profile of the NH_4NO_3+NO reaction is shown in Figure 6 (top) with representative IR spectra at different temperatures. The accumulated NH_4NO_3, NH_4^+, and gas-phase NO were consumed in the range of 100–400 °C accompanied by N_2 generation. A similar TPSR experiment of accumulated NH_4NO_3 and NH_4^+ was conducted under He. A comparison between the TPSR results under NO (Figure 6, top) and He (Figure 6, bottom) shows larger N_2 formation under NO and larger N_2O formation under He.

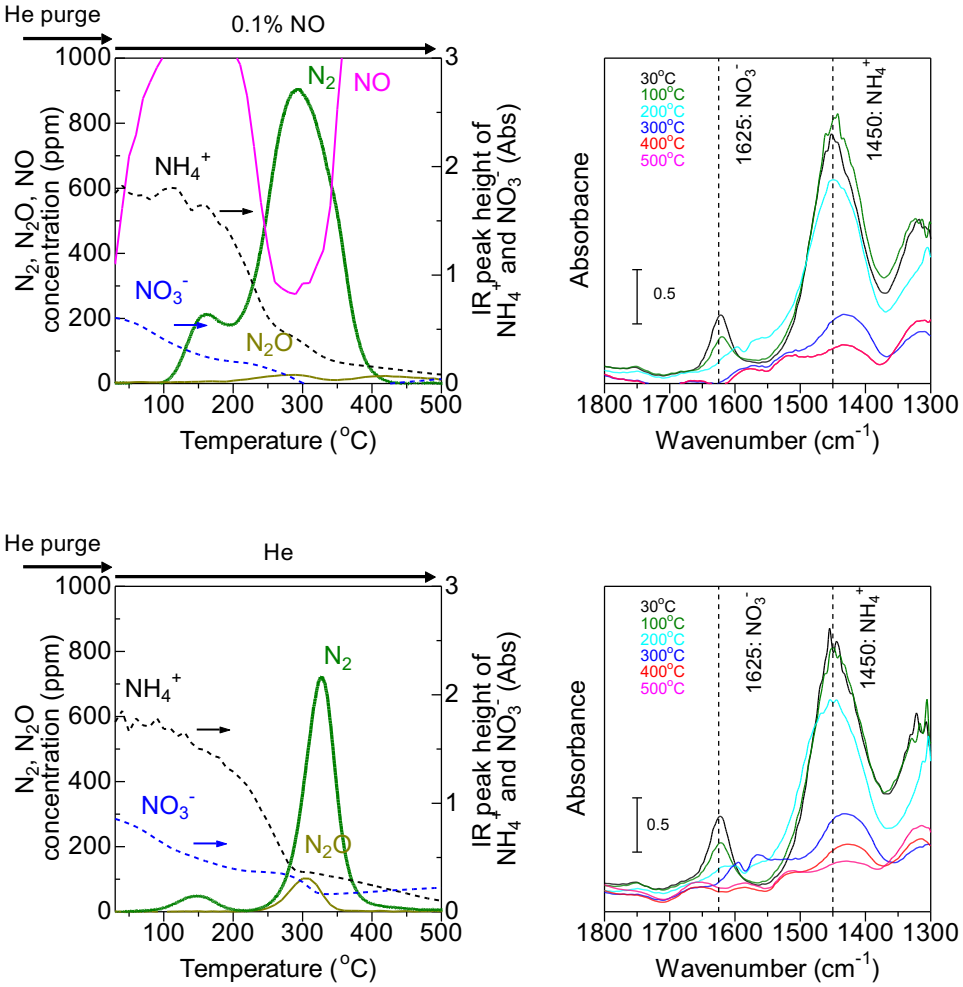

Figure 6. TPSR (20 °C min^{-1}) of adsorbed species on Cu-CHA under 1000 ppm NO (top) or He (bottom) (20 °C min^{-1}) (from 30 °C) and IR spectra of adsorbed species. The IR disk was pre-exposed to 0.16% ppm NO + 0.08% O_3 (900 s), which was followed by purging with He (900 s) and by flowing 0.1% NH_3 (900 s) at 50 °C.

The larger N_2 formation under NO indicates that NH_4NO_3 and NH_4^+ in Cu-CHA react with NO to yield N_2, according to reactions (5) and (6). The larger N_2O formation under He indicates N_2O formation via thermal decomposition of NH_4NO_3 (reaction (7)) [22].

$$NH_4NO_3 \rightarrow N_2O + 2H_2O \quad (7)$$

N_2 formation under He could be ascribed to the thermal decomposition of NO_3^- to NO and its subsequent reaction with NH_4^+ (reaction (6)).

2.3.5 Reaction of adsorbed NH_3 under O_3 and $NO+O_3$

Next, we examined the reaction of NH_3 adsorbed on Cu-CHA under 0.7% O_3 flow at 100 (Figure 7A) and 150 °C (Figure 7B). The IR disk of Cu-CHA was pre-exposed to 0.1% NH_3 for 900 s, which was followed by purging with He and 12% O_2 (900 s). Thereafter, 0.7% O_3 was added to the sample. After introducing O_3, N_2 was observed by MS, N_2O was observed by IR with the gas cell at the outlet, and NH_4^+ consumption was observed by IR. The amount of N_2 generated and the rate of NH_4^+ consumption (slope of the kinetic curve) were higher at higher temperatures; however, the initial rate of N_2O formation (peak height of N_2O formation) was higher at lower temperatures [44]. To investigate the roles of H^+ and Cu^{2+} sites in the transient reaction, the same transient reaction at 150 °C was conducted with Cu-free H-CHA (Figure 7C).

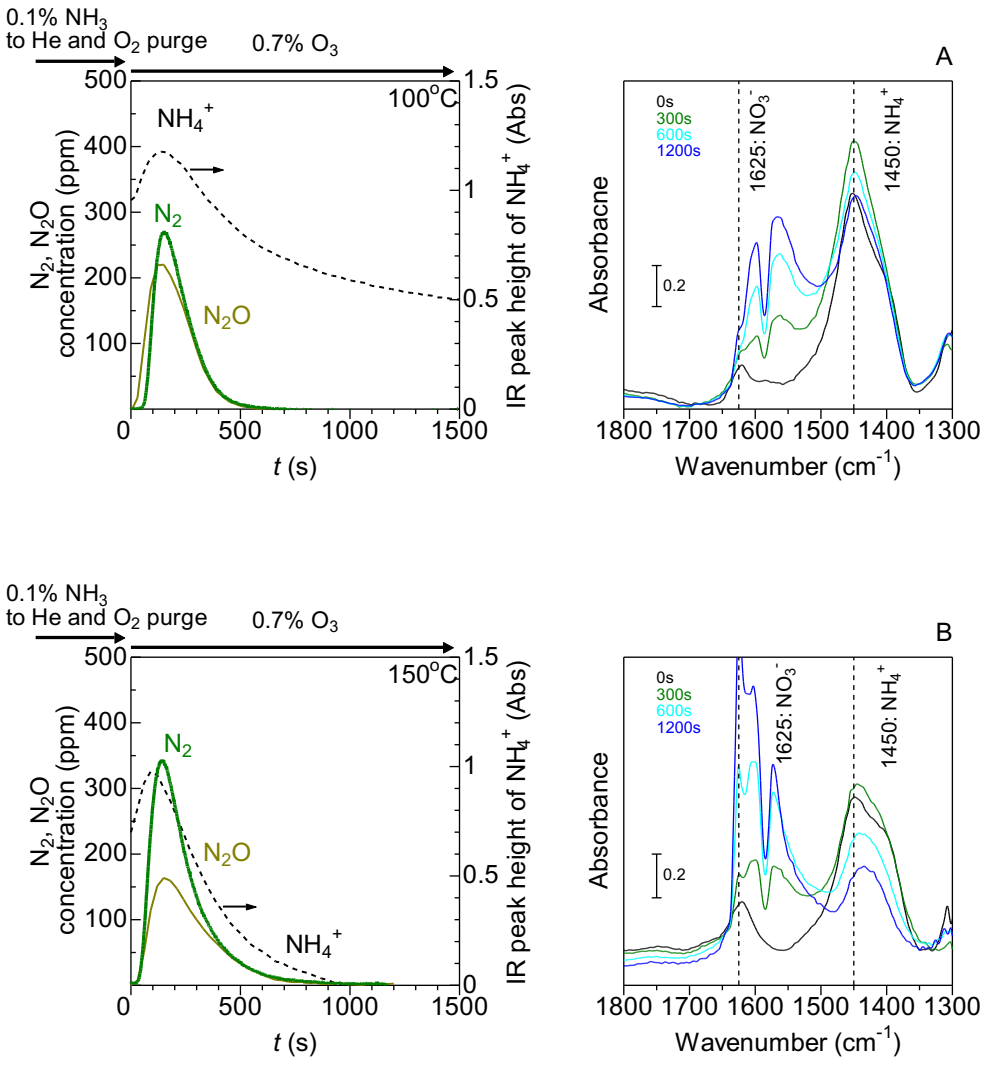

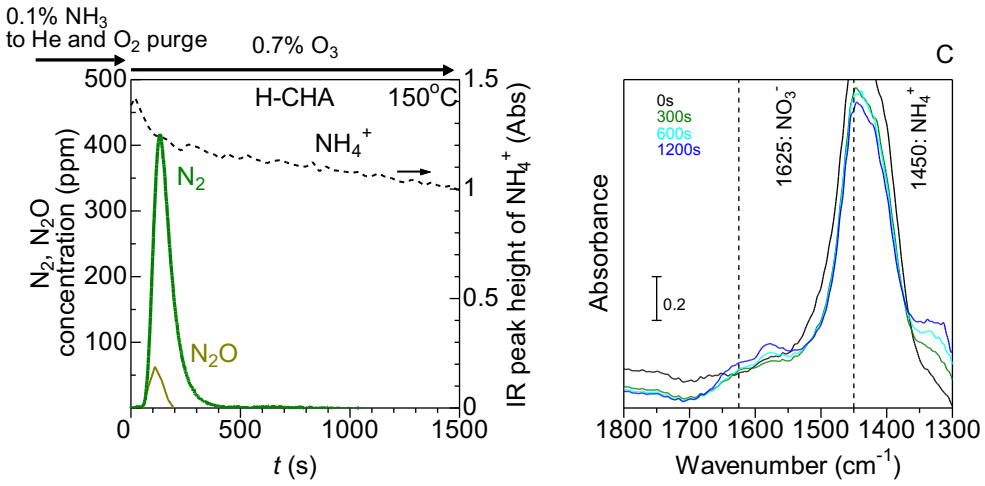

Figure 7. Concentration of outlet N_2 and N_2O (left) and IR spectra of adsorbed species (right) on (A) Cu-CHA at 100 °C under flowing 0.7% O_3. (B) Cu-CHA and (C) H-CHA at 150 °C. The samples were pre-exposed to 0.1% NH_3 at 100 °C (900 s), followed by purging with He and 12% O_2 (900 s).

NH_4^+ consumption and N_2 generation were also observed over H-CHA; however, the amount of N_2 generated and the rate of NH_4^+ consumption over H-CHA were lower than those over Cu-CHA, indicating that in the Cu^{2+} site, the oxidation of adsorbed NH_3 with O_3 to yield N_2 (reaction (8)) was promoted by both H^+ and Cu^{2+} sites, and the Cu^{2+} site enhanced the reaction.

$$2NH_{3ad} + 3O_3 \rightarrow N_2 + 3H_2O + 3O_2 \quad (8)$$

N_2O formation over H-CHA was significantly lower than that over Cu-CHA, indicating that the Cu^{2+} site was the main active site for the oxidation of NH_3 with O_3 to yield N_2O (reaction (9)).

$$2NH_{3ad} + 2O_3 \rightarrow N_2O + 3H_2O + O_2 \quad (9)$$

The same experiment for Cu-CHA at 150 °C was carried out under low-concentration O_3 (0.08%). The results (Figure 8) show that the initial rates of N_2 formation (height of the N_2 kinetic curve), N_2O formation, and NH_4^+ consumption (slope of the NH_4^+ kinetic curve) under 0.08% O_3 are lower than those under 0.7% O_3. The results demonstrate that the reaction rates of adsorbed NH_3 with O_3 to yield N_2 (reaction (8)) and N_2O (reaction (9)) are lower under lower concentrations of O_3.

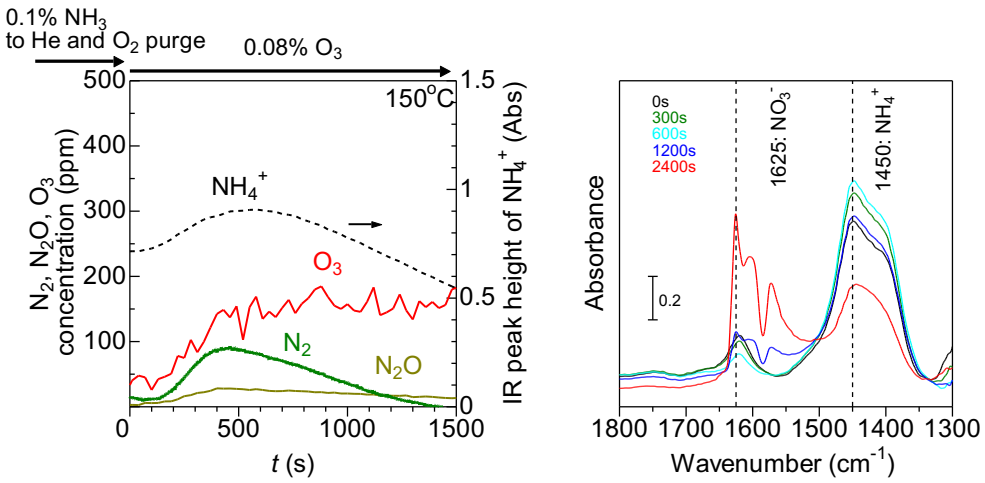

Figure 8. Concentration of outlet N_2, N_2O and O_3 (left) and IR spectra of adsorbed species (right) on Cu-CHA at 150℃ under 0.08% O_3. The IR disk was pre-exposed to 0.1% NH_3 (900 s) at 150 °C.

The TPSR of adsorbed NH_3 under 0.7% O_3 over Cu-CHA and H-CHA was performed to obtain further information on the reactivity of NH_4^+ with O_3 (Figure 9). The heights of N_2 and N_2O formation peaks below 200 °C are higher for Cu-CHA, indicating that the Cu^{2+} site is more active than the H^+ site for the O_3 oxidation of adsorbed NH_3 by reactions (8) and (9). However, H-CHA showed a larger N_2O formation peak in the range of 200–350 °C. Considering that the thermal decomposition of adsorbed NH_4NO_3 on H-CHA results in N_2O formation in the range of 200–350 °C [20], the large N_2O peak over H-CHA can be explained by the O_3 oxidation of adsorbed NH_3 to yield NO_2 (reaction (10)) followed by its reaction with adsorbed NH_3 to form NH_4NO_3 and by the decomposition of NH_4NO_3 to yield N_2O.

$$2NH_{3ad} + 3O_3 \rightarrow 2NO_2 + 3H_2O + O_2 \qquad (10)$$

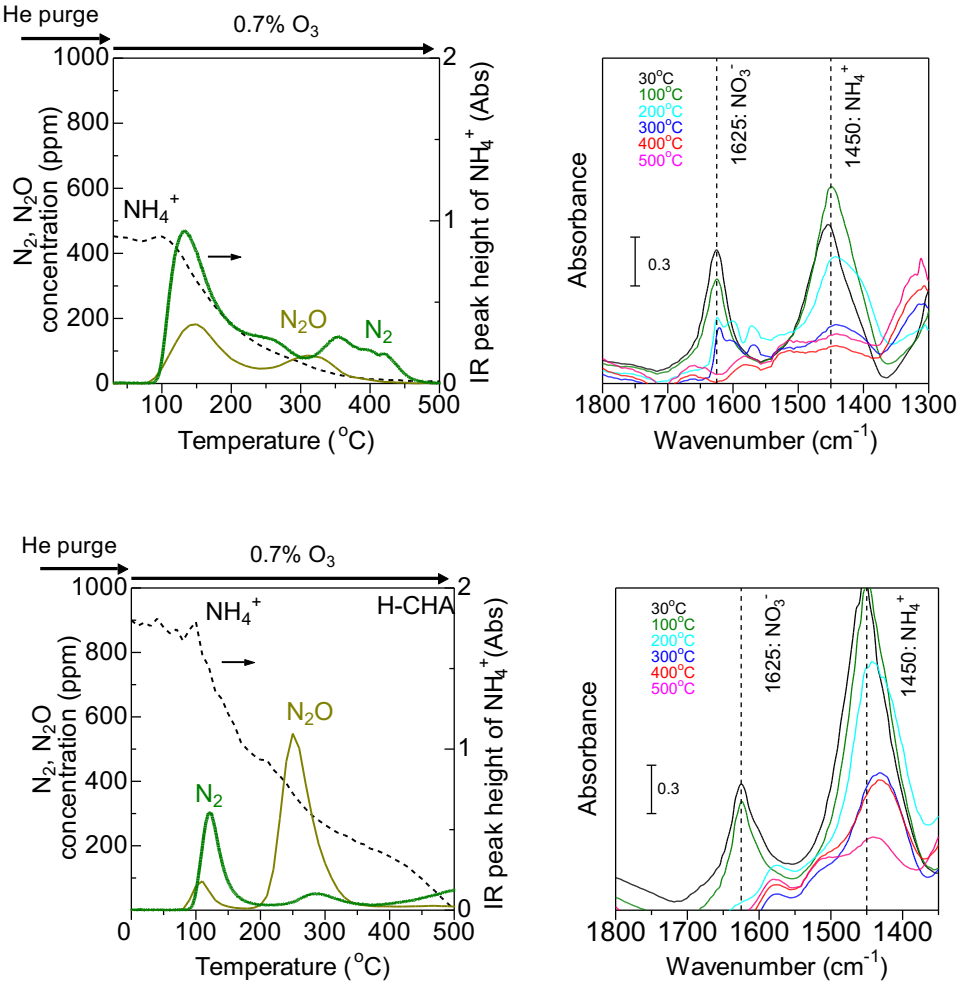

Figure 9. TPSR of adsorbed NH_3 (20 °C min^{-1}) (from 30 °C) under 0.7% O_3 over (top) Cu-CHA and (bottom) H-CHA; TPSR profiles (left) and IR spectra of adsorbed species (right). The IR disk was pre-exposed to 0.1% NH_3 (900 s) at 50 °C.

To study the effect of NO co-fed with O_3 over NH_3-preadsorbed Cu-CHA, we conducted the reaction of adsorbed NH_3 under 0.16% NO + 0.08% O_3 flow over Cu-CHA at three different temperatures (50, 100, and 150 °C), as shown in Figure 10.

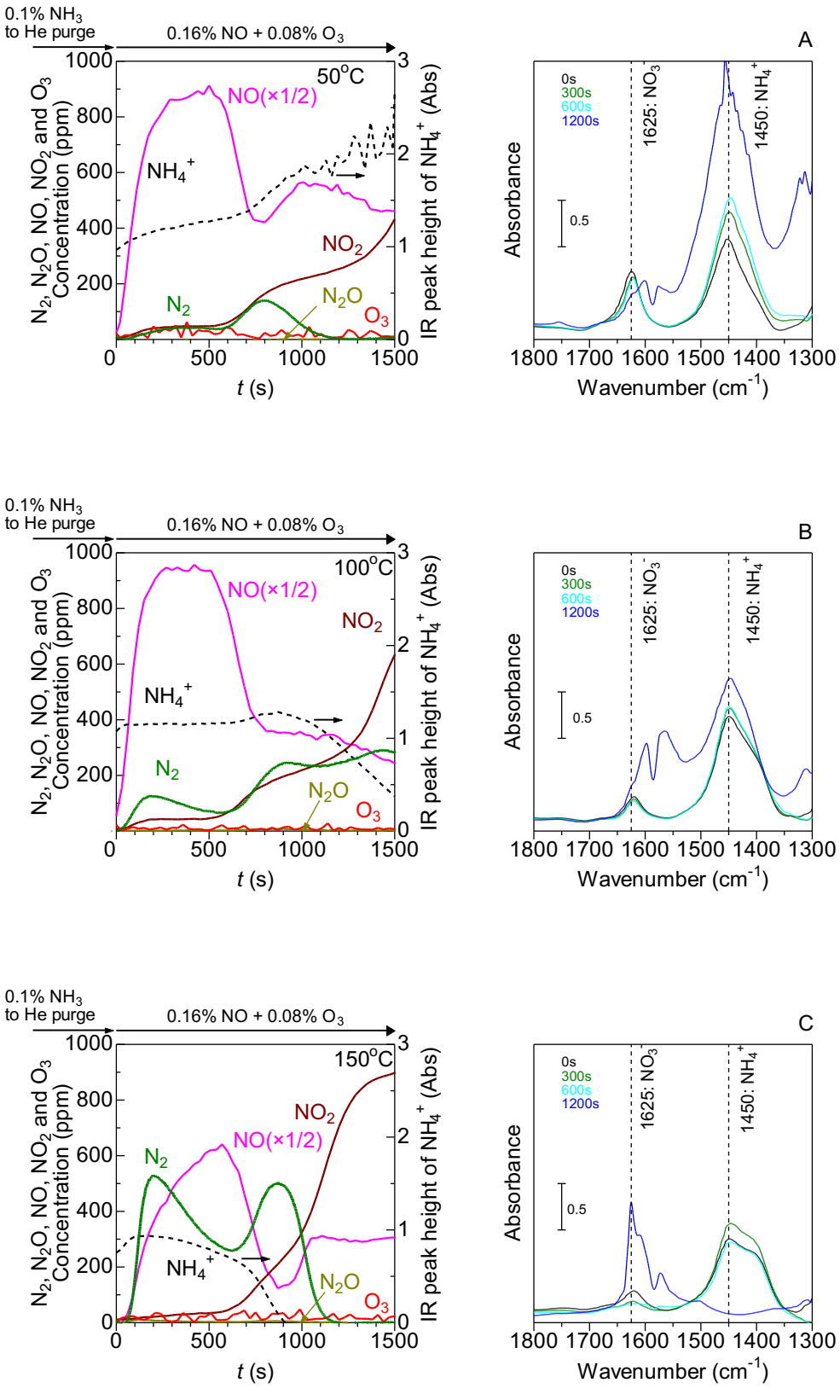
0.1% NH3
to He purge
0.16% NO + 0.08% O3
50°C
NO(×1/2)
NH4+
NO2
N2
N2O
O3
N2, N2O, NO, NO2 and O3
Concentration (ppm)
IR peak height of NH4+ (Abs)
t (s)
A
0s
300s
600s
1200s
1625: NO3-
1450: NH4+
0.5
Absorbance
Wavenumber (cm-1)
100°C
B
150°C
C

Figure 10. Concentration of outlet N_2, N_2O, NO, NO_2, and O_3(left) and IR spectra of adsorbed species (right) on Cu-CHA at (A) 50 °C, (B) 100 °C, and (C) 150 °C under 0.16% NO + 0.08% O_3. The IR disk was pre-exposed to 0.1% NH_3 (900 s) at each temperature.

The reaction at 50 °C increased the IR peak heights at 1575 and 1320 cm^{-1}. Considering that NO_3^- and NH_4^+ can show IR absorption in this region [20], this result indicates that NO_3^- accumulated on the surface, possibly as NH_4NO_3. N_2 formation can be caused by the reaction of NO_2 with adsorbed NH_3 by reaction (4). At higher temperatures (100 and 150 °C), the IR peak height for NH_4^+ decreased with the time of NO+O_3 flow accompanying the N_2 formation, indicating that the adsorbed NH_3 (NH_4^+) reacted with NO_2 to yield N_2 via reaction (4). In contrast to the reaction of the adsorbed NH_3 under O_3 (Figure 9), in the reaction under NO+O_3, N_2O formation was not observed. Considering that O_3 is fully converted by the gas-phase reaction of NO+O_3 under low-O_3-concentration conditions (O_3/NO = 0.5), as shown in Figure 1, the absence of N_2O can be explained by the absence of O_3 in the feed due to complete consumption by the gas-phase NO+O_3 reaction before arriving at the Cu-CHA surface.

2.4 Conclusions

The catalyst-free oxidation of NO by O_3 at room temperature yielded NO_2 at an O_3/NO ratio of 0.5, while N_2O_5 was the main product at higher O_3/NO ratios (>0.5). DFT calculations verified the reaction route of NO_2 to N_2O_5 with low activation energies (2 kJ mol^{-1}), which is consistent with the experimental results. The exposure of Cu-CHA to a flow of 0.16% NO + 0.08% O_3 at 100 °C resulted in the storage of NO_X as NO_3^- on Cu^{2+} sites. The captured NO_X was desorbed as NO_2 upon heating at >300 °C. At 100 °C, the captured NO_X reacted with NH_3 to yield N_2 and NH_4NO_3. At >200 °C, NH_4NO_3 reacted with NO to yield N_2. NH_3 adsorbed on Cu-CHA was oxidized by excess O_3 (0.7%) to produce N_2 and N_2O at low temperatures (<150 °C) in a N_2O/N_2 ratio of 0.75. The rates of NH_3 oxidation by O_3 to N_2 and N_2O were lower (below 100 ppm) at lower O_3 concentrations (0.08%). Oxidation of the NH_3 adsorbed on Cu-CHA by NO+O_3 resulted in the selective formation of N_2 at low temperatures (<150 °C). The aforementioned results may aid in designing unsteady-state lean De-NOx via the desorption/reaction of captured NOx with NH_3 or reduction of NOx with captured NH_3.

2.5 References

(1) Borfecchia, E.; Beato, P.; Svelle, S.; Olsbye, U.; Lamberti, C.; Bordiga, S. *Chem. Soc. Rev.* **2018**, *47* (22), 8097–8133.

(2) Zhang, R.; Liu, N.; Lei, Z.; Chen, B. *Chem. Rev.* **2016**, *116* (6), 3658–3721.

(3) Beale, A. M.; Gao, F.; Lezcano-Gonzalez, I.; Peden, C. H. F.; Szanyi, J. *Chemical Society Reviews*. October 21, 2015, pp 7371–7405.

(4) Zhang, S.; Pang, L.; Chen, Z.; Ming, S.; Dong, Y.; Liu, Q.; Liu, P.; Cai, W.; Li, T. *Appl. Catal. Gen.* **2020**, *607*.

(5) Liu, F.; Yu, Y.; He, H. *Chem Commun* **2014**, *50* (62), 8445–8463.

(6) Brandenberger, S.; Kröcher, O.; Tissler, A.; Althoff, R. *Catal. Rev. - Sci. Eng.* **2008**, *50* (4), 492–531.

(7) Liu, Q.; Bian, C.; Ming, S.; Guo, L.; Zhang, S.; Pang, L.; Liu, P.; Chen, Z.; Li, T. *Applied Catalysis A: General*. October 25, 2020.

(8) Chen, H. Y.; Mulla, S.; Weigert, E.; Camm, K.; Ballinger, T.; Cox, J.; Blakeman, P. *SAE Int. J. Fuels Lubr.* **2013**, *6* (2), 372–381.

(9) Lee, J.; Theis, J. R.; Kyriakidou, E. A. *Appl. Catal. B: Environ.* **2019**, *243*, 397–414.

(10) Khivantsev, K.; Jaegers, N. R.; Kovarik, L.; Prodinger, S.; Derewinski, M. A.; Wang, Y.; Gao, F.; Szanyi, J. *Appl. Catal. Gen.* **2019**, *569*, 141–148.

(11) Selleri, T.; Gramigni, F.; Nova, I.; Tronconi, E.; Dieterich, S.; Weibel, M.; Schmeisser, V. *Catal. Sci. Technol.* **2018**, *8* (9), 2467–2476.

(12) Gramigni, F.; Selleri, T.; Nova, I.; Tronconi, E.; Dieterich, S.; Weibel, M.; Schmeisser, V. *Top. Catal.* **2019**, *62* (1–4), 3–9.

(13) De La Torre, U.; Urrutxua, M.; Pereda-Ayo, B.; González-Velasco, J. R. *Catal. Today* **2016**, *273*, 72–82.

(14) Kim, C. H.; Perry, K.; Viola, M.; Li, W.; Narayanaswamy, K. **2011**.

(15) Li, M.; Malamis, S. A.; Epling, W.; Harold, M. P. *Appl. Catal. B: Environ.* **2019**, *242*, 469–484.

(16) Theis, J. R.; Kim, J.; Cavataio, G. *SAE Int. J. Fuels Lubr.* **2015**, *8* (2), 460–473.

(17) Marberger, A.; Petrov, A. W.; Steiger, P.; Elsener, M.; Kröcher, O.; Nachtegaal, M.; Ferri, D. *Nat. Catal.* **2018**, *1* (3), 221–227.

(18) Liu, C.; Kubota, H.; Amada, T.; Kon, K.; Toyao, T.; Maeno, Z.; Ueda, K.; Ohyama, J.; Satsuma, A.; Tanigawa, T.; Tsunoji, N.; Sano, T.; Shimizu, K. *ChemCatChem* **2020**, *12* (11), 3050–3059.

(19) Kubota, H.; Toyao, T.; Maeno, Z.; Inomata, Y.; Murayama, T.; Nakazawa, N.; Inagaki, S.; Kubota, Y.; Shimizu, K. *ACS Catal.* **2021**, *11* (17), 11180–11192.

(20) Liu, C.; Malta, G.; Kubota, H.; Kon, K.; Toyao, T.; Maeno, Z.; Shimizu, K. *J. Phys. Chem. C* **2021**, *125* (25), 13889–13899.

(21) Yasumura, S.; Liu, C.; Toyao, T.; Maeno, Z.; Shimizu, K. *J. Phys. Chem. C* **2021**, *125* (3), 1913–1922.

(22) Liu, C.; Malta, G.; Kubota, H.; Toyao, T.; Maeno, Z.; Shimizu, K. *J. Phys. Chem. C* **2021**, *125* (40), 21975–21987.

(23) Sun, C.; Zhao, N.; Zhuang, Z.; Wang, H.; Liu, Y.; Weng, X.; Wu, Z. *J. Hazard. Mater.* **2014**, *274*, 376–383.

(24) Lin, F.; Wang, Z.; Zhang, Z.; He, Y.; Zhu, Y.; Shao, J.; Yuan, D.; Chen, G.; Cen, K. *Chemical Engineering Journal*. February 15, 2020.

(25) Mok, Y. S.; Lee, H. J. *Fuel Process. Technol.* **2006**, *87* (7), 591–597.

(26) Lin, F.; Wang, Z.; Shao, J.; Yuan, D.; He, Y.; Zhu, Y.; Cen, K. *CHINESE J CATAL.* **2017**, *38* (7), 1270–1280.

(27) Ji, R.; Wang, J.; Xu, W.; Liu, X.; Zhu, T.; Yan, C.; Song, J. *Ind Eng Chem Res* **2018**, *57* (43), 14440–14447.

(28) Skalska, K.; Miller, J. S.; Ledakowicz, S. *Chem. Eng. Sci.* **2011**, *66* (14), 3386–3391.

(29) Erme, K.; Jõgi, I. *Environ Sci Technol* **2019**, *53* (9), 5266–5271.

(30) Maeda, S.; Harabuchi, Y.; Takagi, M.; Saita, K.; Suzuki, K.; Ichino, T.; Sumiya, Y.; Sugiyama, K.; Ono, Y. *J Comput Chem* **2018**, *39* (4), 233–250.

(31) Fukui, K. *Acc Chem Res* **1981**, *14* (12), 363.

(32) Bannwarth, C.; Ehlert, S.; Grimme, S. *J Chem Theory Comput* **2019**, *15* (3), 1652–1671.

(33) Frisch, M. J. G.; Trucks, W.; Schlegel, H. B.; Scuseria, G. E.; Robb, M. A.; Cheeseman, J. R.; Scalmani, G.; Barone, V.; Mennucci, B.; Petersson, G. A.; Nakatsuji, H.; Caricato, M.; Li, X.; Hratchian, H. P.; Izmaylov, A. F.; Bloino, J.; Zheng, G.; Sonnenberg, J. L. *Gaussian Inc.: Wallingford, CT*. 2016.

(34) Becke, A. D. *Phys Rev A (Coll Park)* **1988**, *38*, 3098–3100.

(35) Lee, C.; Ynag, W.; Parr, R. G. *Phys Rev B Condens Matter Mater Phys* **1988**, *37*, 785–789.

(36) Otasek, D.; Morris, J. H.; Bouças, J.; Pico, A. R.; Demchak, B. *Genome Biol* **2019**, *20* (1), 185.

(37) Lin, F.; Wang, Z.; Zhang, Z.; He, Y.; Zhu, Y.; Shao, J.; Yuan, D.; Chen, G.; Cen, K. *Chem. Eng. J.* **2020**, *382*.

(38) Lin, F.; Wang, Z.; Ma, Q.; He, Y.; Whiddon, R.; Zhu, Y.; Liu, J. *Energy and Fuels* **2016**, *30* (6), 5101–5107.

(39) Yasumura, S.; Saita, K.; Miyakage, T.; Kon, K.; Toyao, T.; Maeno, Z.; Taketsugu, T.;

Shimizu, K. *Nat. Commun.* **2023**, *14*, 3926.

(40) Negri, C.; Hammershøi, P. S.; Janssens, T. V. W.; Beato, P.; Berlier, G.; Bordiga, S. *Chem. Eur. J.* **2018**, *24* (46), 12044–12053.

(41) Lezcano-Gonzalez, I.; Deka, U.; Arstad, B.; Van Yperen-De Deyne, A.; Hemelsoet, K.; Waroquier, M.; Van Speybroeck, V.; Weckhuysen, B. M.; Beale, A. M. *Phys. Chem. Chem. Phys* **2014**, *16* (4), 1639–1650.

(42) Shan, Y.; Shi, X.; Du, J.; Yu, Y.; He, H. *Catal. Sci. Technol.* **2019**, *9* (1), 106–115.

(43) Zhu, H.; Kwak, J. H.; Peden, C. H. F.; Szanyi, J. *Catal. Today* **2013**, *205*, 16–23.

(44) Yates, M.; Martín, J. A.; Martín-Luengo, M. Á.; Suárez, S.; Blanco, J. *Catal. Today* **2005**, *107–108*, 120–125.

(45) Kubota, H.; Liu, C.; Toyao, T.; Maeno, Z.; Ogura, M.; Nakazawa, N.; Inagaki, S.; Kubota, Y.; Shimizu, K. *ACS Catal* **2020**, *10* (3), 2334–2344.

Chapter3

Redox-Half-Cycle Dynamics of NH_3–SCR on Sulfate-Modified CeO_2 Revealed by Modulation-Excitation Spectroscopy

3.1 Introduction

The selective catalytic reduction of NO_x using NH_3 (NH_3–SCR) by Cu-exchanged zeolites has been employed for NO_x removal from diesel exhausts.[1,2] V_2O_5–WO_3/TiO_2 has long been commercially utilized to control NO_x emissions from stationary sources.[3] After numerous studies aimed at developing alternative NH_3–SCR catalysts, tungstate-modified CeO_2 (W/CeO_2) catalysts have been developed.[4–6] Fundamental studies revealed that the high performance of W/CeO_2 is caused by cooperation between redox property of CeO_2 and surface acidity caused by the acidic additive (tungstate). Later, CeO_2-based catalysts modified by typical metal acidic salts, sulfate-, phosphate, and arsenate-loaded CeO_2 (S/CeO_2,[7–10] P/CeO_2,[4,11–13] As/CeO_2[14–16]) have been reported to show higher NOx conversions than pristine CeO_2. Among them, S/CeO_2 catalysts are promising alternative NH_3–SCR catalysts because of their high NO_x conversions, high tolerance to sulfur poisoning, and high hydrothermal stability.[17] Despite the high impact of S/CeO_2 as a promising catalyst for NH_3–SCR, the catalytic mechanism of this system and mechanistic role of the sulfate species are still under debate. [7–10]

A large number of papers have studied the NH_3–SCR mechanisms over Cu-CHA and V-oxide catalysts. It is well established that NH_3–SCR over Cu-CHA catalysts is based on the Cu^{2+}/Cu^{+} redox and so called the reduction half-cycle (RHC) and oxidation half-cycle (OHC). In the RHC, $Cu^{2+}(OH^{-})$ is reduced by NO + NH_3 to produce N_2, H_2O, and Cu^{+}. In the subsequent OHC, Cu^{+} is oxidized by O_2 followed by hydration to regenerate the $Cu^{2+}(OH^{-})$ species. Based on *operando* spectroscopic results, we have recently demonstrated the common mechanistic features of Cu-zeolites and V-oxides catalysts in NH_3–SCR. [2,12,18–24] We proposed that NH_3–SCR mechanism for V_2O_5/TiO_2 and WO_3-V_2O_5 catalysts is also based on the V^{5+}/V^{4+} redox including RHC and OHC. Recently, our *operando* spectroscopic strategy has been extended to tungstate- and phosphate-loaded ceria catalysts (W/CeO_2, P/CeO_2). [6,13] We proposed that NH_3–SCR over W/CeO_2 and P/CeO_2 is based on the Ce^{4+}/Ce^{3+} redox mechanism including RHC and OHC; $Ce^{4+}(OH^{-})$ is reduced by NO + NH_3 to produce N_2, H_2O, and Ce^{3+}, which is oxidized by O_2 followed regenerate the $Ce^{4+}(OH^{-})$ species. We have also studied the detailed mechanism of RHC over W/CeO_2 and P/CeO_2. The RHC is divided into three elementary steps; first, $Ce^{4+}(OH^{-})$ is reduced by NO to produce Ce^{3+} and nitrous acid (HONO), which reacts with NH_3 to yield ammonium nitrite (NH_4NO_2), and thermal decomposition of NH_4NO_2 gives N_2 and H_2O. The reaction of HONO with acidic OH groups on the catalyst surface can give NO^{+} adsorbed on the anionic oxygen site and water. The mechanism via the HONO or NO^{+} intermediates has been recently reported by for NH_3–SCR over Cu-zeolites, [20,23,25] Fe-zeolites,[26] and V_2O_5/CeO_2. [22]

Modulation Excitation (ME) Spectroscopy is utilized to reveal the dynamic changes of intermediates involved in catalytic reactions.[27–32] The reactive species

on the catalyst surface can be observed by combining diffuse reflectance infrared Fourier transform spectroscopy (DRIFTS) with ME spectroscopy. This technique, known as ME-DRIFTS, enables the removal of IR bands corresponding to spectator species that are not directly involved in the catalytic cycle. Phase-sensitive detection (PSD) analysis transforms the time-domain spectra into phase-domain spectra isolating signals that respond specifically to periodic perturbations. Several studies have utilized ME-DRIFTS to monitor the dynamics of intermediates during NH_3-SCR over tungsten-based,[32] V-based[31,33] and Cu-zeolite[34] catalysts. These reports have provided direct spectroscopic evidences on key intermediates with short lifetime.

Herein, we report a comprehensive investigation into the NH_3−SCR mechanism over S/CeO_2 catalysts. First, $Ce^{4+} \leftrightarrow Ce^{3+}$ redox cycles (RHC/OHC) under unsteady-state NH_3−SCR conditions are studied using *in situ/operando* infrared (IR), ultraviolet-visible (UV−vis), and X-ray absorption near-edge structure (XANES) in combination with gas-phase analyses combining with modulation excitation (ME) method. Then, the density functional theory (DFT) calculations are presented to propose the molecular structure of the sulfate species on CeO_2 together with EPR spectra. Then considering the proposed mechanism in the literature, a detailed mechanisms of NH_3–SCR over S1/CeO_2 are discussed.

3.2 Experimental Section

3.2.1 Catalyst preparation

CeO_2 (Type B) was supplied by Daiichi Kigenso Kagaku Kogyo Co., Ltd. S loaded CeO_2/B loaded CeO_2 catalysts were prepared by impregnating CeO_2 with an aqueous solution of $(NH_4)_2SO_4$ or H_3BO_3, followed by evaporation to dryness, drying at 100 °C for 12 h, and calcination at 600 °C for 3 h. For comparison, the CeO_2 without loading any elements was also calcinated at 600 °C for 3h.

3.2.2 Catalytic tests

Catalytic tests were performed with the catalysts (typically 40 mg) in a fixed-bed flow reactor under several flowing gas mixtures (total flow rate of 100 mL/min): 0.1% NO/0.1% NH_3/10%O_2/He. The concentrations of NO and NH_3 were analyzed using an IR spectrometer (JASCO FT/IR-4100 with a gas cell) based on calibration standards. The N_2 formation was monitored by a mass spectrometry (JMS-Q1500GS, JEOL Ltd.).

3.2.3 *In situ*/*operando* UV-Vis

Operando/in situ diffuse reflectance UV-vis spectra were recorded in an *in situ* flow diffuse reflectance cell using a JASCO V750 spectrometer. The catalyst powder (40 mg) was placed in a diffuse reflectance cell (JASCO HISV-728) with a quartz window connected to a gas-flow system (total flow rate of 100 mL min^{-1}). The center of the smooth sample and spectrometer were connected by an optical fiber. The baseline was obtained with $BaSO_4$ at room temperature. The spectra were measured in a range 300–800 nm. The reflectance was converted to Kubelka–Munk (KM) intensity. For *operando* UV-vis measurement, 0.1% NO

(0.1% NH_3) or 10% O_2 (balanced with He) was introduced to the cell at 350 °C. The formation of N_2 (m/z = 28) under 0.1%NH_3 + 0.1%NO was analyzed using online mass spectrometry (JMS-Q1500GS, JEOL Ltd.), the formation of NO_2 was monitored by FTIR with home-made gas cell connected with the outlet of UV-Vis cell.

3.2.4 Modulation excitation spectroscopy with a Phase-Sensitive Detection Analysis

Diffuse reflectance infrared Fourier transform (DRIFT) spectra were collected from 4000 to 900 cm^{-1} at a resolution of 4 cm^{-1} using a FT/IR-4600 spectrometer (JASCO) equipped with an MCT detector and DRIFTS cell (DR-600Ai, JASCO). The sample and background spectra were taken by coadding 5 and 15 scans, respectively. Approximately 40 mg of each sample was loaded into the DR-600Ai spectroscopic cell, which was equipped with a 2-mm-thick zinc selenide window (Pie Optics Co., Ltd. Japan). Prior to each experiment, the sample was dehydrated under 10 vol% O_2/He at 500 °C for 330 min. For the operando experiments, various mixtures of 0.1% NO, 0.1% NH_3, and 10% O_2 in He balance were admitted to the cell. The total flow rate for all experiments was fixed at 100 mL min^{-1}. A JMS-Q1500GS mass spectrometer (JEOL Ltd.) was connected at the outlet of the cell to monitor m/z = 17 (NH_3), 18 (H_2O), 28 (N_2), 30 (NO), and 32 (O_2).

Concentration modulation experiments were carried out by alternately pulsing NO in O_2, and NH_3 + NO in 10 vol% O_2 for 300 s (half-cycle) with 15 cycles. Pulses were achieved using two solenoid valves (GL Science) attached to the main line to the spectroscopy cell. The time-resolved DRIFT spectra from at least five modulation cycles were converted into phase-resolved spectra using the following equation:

$$A\left(\varphi^{PSD}\right)= \frac{2}{T} \int_0^T A\,(t) \sin\left(\omega t+ \varphi^{PSD}\right) dt \qquad \text{(Eq.1)}$$

where $A\left(\varphi^{PSD}\right)$ is the absorbance in the phase-resolved spectra, T is the modulation period, A (t) is the absorbance in the time-resolved spectra, ω is the demodulation index, and φ^{PSD} is the phase angle. Only the fundamental frequency, k=1 was used for the analysis.

Ce L_3-edge X-ray absorption near-edge structure (XANES) spectra were collected in the transmission mode using the BL07 beamline at SAGA-LS (Saga, Japan). The storage ring was operated at 8 GeV. A Si(111) double-crystal monochromator was used to obtain monochromatic X-ray beams. A sample pellet prepared using 1.13 mg of the S1/CeO_2 catalyst diluted in boron nitride 21 mg (φ: 7 mm) was introduced into a quartz *in situ* cell equipped with Kapton film windows. The temperature of the sample was controlled by an electric heating jacket surrounding the quartz tube. The inlet gas feed to the cell was controlled by a VICI 4-port switching valve to introduce periodic concentration modulations

between 5% O_2/He and 1% NO/He, each at a total flow rate of 200 mL/min. In an ME-XAS experiment, 5 cycles were performed with a period T of 600s. During each cycle, 10 XANES spectra were collected from 5.55 to 6.01keV with a 0.4 eV step. XANES analysis was conducted using Athena software ver. 0.9.26, which is included in the Demeter package.[35]

The output results of each spectroscopic measurement were fed to a homemade MES-PSD analysis code utilizing the FFTW library.

3.2.5 Computational methods

Periodic DFT calculations were performed using the Vienna ab initio simulation package (VASP, version 5.4.4).[36,37] For VASP, the Perdew–Burke–Ernzerhof functional revised for solids (PBEsol)[38] was employed in combination with the projector-augmented wave (PAW) method[39]. A kinetic energy cutoff of 400 eV was used for the plane-wave basis sets. Gaussian smearing with a width of 0.05 eV was applied to occupy the electronic levels. The k-point mesh includes only the gamma point of the Brillouin zone (1 × 1 × 1). Van der Waals interactions were described using a dispersion-corrected DFT-D3 (BJ) function.[40] The convergence of the force on each atom was set to 0.03 eV $Å^{-1}$. The effect of adding Hubbard U was considered based on Dudarev's formulation. The effective *U* value (denoted as U_{eff}) of *U-J* was set to 5 eV for Ce.

The CeO_2 material used in this study is polycrystalline, and therefore, one of the most likely surface terminations is (111). The CeO_2(111) surface was simulated using supercell slab models (Figure 1). The repeated slabs along the surface-normal direction were separated by a minimum vacuum region thickness of 14 Å. The bottom layer was fixed at their original bulk positions.

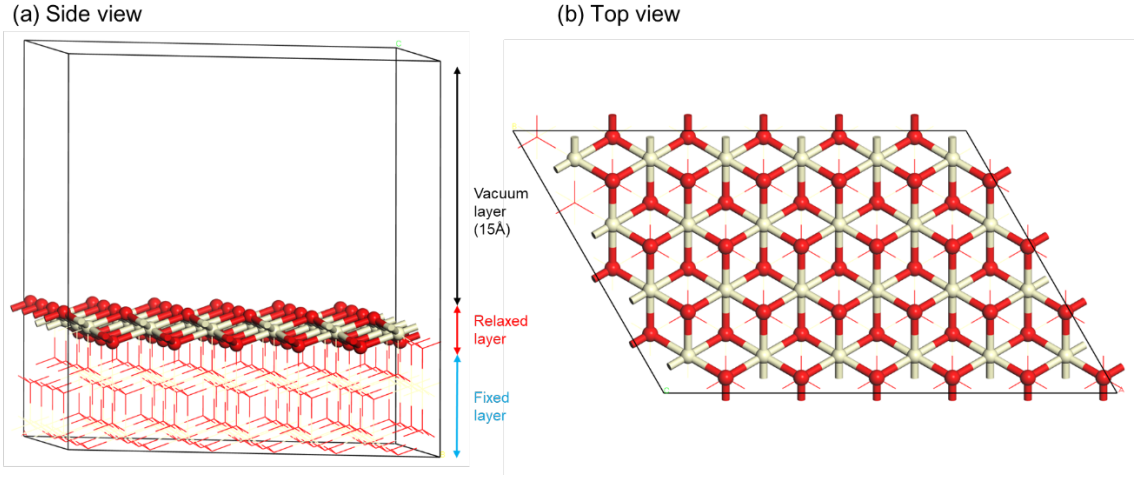

Figure 1. Side and top view of slab models for computational study of the CeO_2 (111) surface; Light yellow: Ce; red: O

The O vacancy formation energy (E_{Ovac}) is defined as:

$$E_{Ovac} = E_{removed} - E_{perfect} + \frac{1}{2}E_{O_2}, \qquad \text{(Eq.2)}$$

Where $E_{removed}$ and $E_{perfect}$ are the slab energies after and before removal of one O atom, respectively. E_{O2} is the total energy of an isolated O_2 molecule.
The differential charge density ($\Delta\rho$) of the supported sulfur oxide species is defined as

$$\Delta\rho = \rho_{SO_x/CeO_2} - \rho_{SO_x} - \rho_{CeO_2},$$

(Eq.3)

where ρ_{SO_x/CeO_2}, ρ_{SO_x}, and ρ_{CeO_2} are the charge densities of the CeO_2-supported sulfur oxide, free-state sulfur oxide, and bare CeO_2(111) surfaces, respectively. Bader charge analysis was also performed to evaluate the valence state of sulfur on the surfaces of metal oxides.

3.2.6 *Ab initio* thermodynamic analysis

Ab initio thermodynamic analysis was performed to investigate the effects of reaction gases (O_2 and H_2O) and temperature on the sulfur oxide species on the CeO_2(111) surface. The enthalpy and entropy at each temperature and standard state pressure (1 atm) were obtained from the NIST-JANAF Thermochemical Tables. Sulfate acid (H_2SO_4) was used to determine the energy of the sulfur oxide species. The energies of the gas molecules were obtained using a large empty unit cell (12 Å × 30 Å × 22 Å) to mimic the isolated species. The equilibrium reaction, energy change (ΔE), Gibbs free energy change (ΔG), and chemical potential change ($\Delta\mu$) under SO_2, O_2 and H_2O atmospheres are given by Eq. (4)–(7).

$$xSO_2 + (CeO_{2(\text{with O defect})} + \frac{1}{2}O_2) + \left(\frac{1}{2}z\right)H_2O + \left(-x + \frac{1}{2}y - \frac{1}{4}z\right)O_2 \rightarrow (S_xO_yH_z)/CeO_2$$

(4)

$$\Delta E = E\left[(S_xO_yH_z)/CeO_2\right] - xE[SO_2] - \left(\frac{1}{2}z\right)E[H_2O] - \left(-x + \frac{1}{2}y - \frac{1}{4}z\right)E[O_2]$$

(5)

$$\Delta G(T, p) = \Delta E - \left(\frac{1}{2}z\right)\Delta\mu_{H_2O} - \left(-x + \frac{1}{2}y - \frac{1}{4}z\right)\Delta\mu_{O_2} - x\Delta\mu_{SO_2}$$

(6)

$$\Delta\mu_{gas} = \Delta\mu_{gas}(T, p^0) + RT\ln\left(\frac{p_{gas}}{p^0}\right) \text{ (gas = } O_2, SO_2 \text{ and } H_2O)$$

(7)

Here, $S_xO_yH_z/CeO_2$ is the CeO_2-supported tungsten oxide species, $E[S_xO_yH_z/CeO_2]$ is the total energy of the species, $E(CeO_2)$ is the total energy of the CeO_2(111) slab model, $E(O_2)$ and $E(H_2O)$ represent the total energies of the gas molecules, $\Delta\mu_{gas}$ is the change in the chemical potential of the gases involved in the reaction (Eq. (7)), T is the temperature (K), p^0 is the atmospheric pressure, and p_{gas} is the partial pressure of the reaction gas.

3.3 Results and Discussion

3.3.1 NH_3–SCR performance

The temperature dependence of NOx conversion for sulfate or borate loaded CeO_2 and pure CeO_2 is shown in Figure 2. The conversions above 200 °C depend strongly on the additives and increase in the order of $S1/CeO_2$ > $B1/CeO_2$ > CeO_2. The $S1/CeO_2$ catalyst shows the highest activity for NH_3–SCR among the three catalysts. The results imply that the addition of non-metallic elements enhances NH_3–SCR performance of CeO_2.

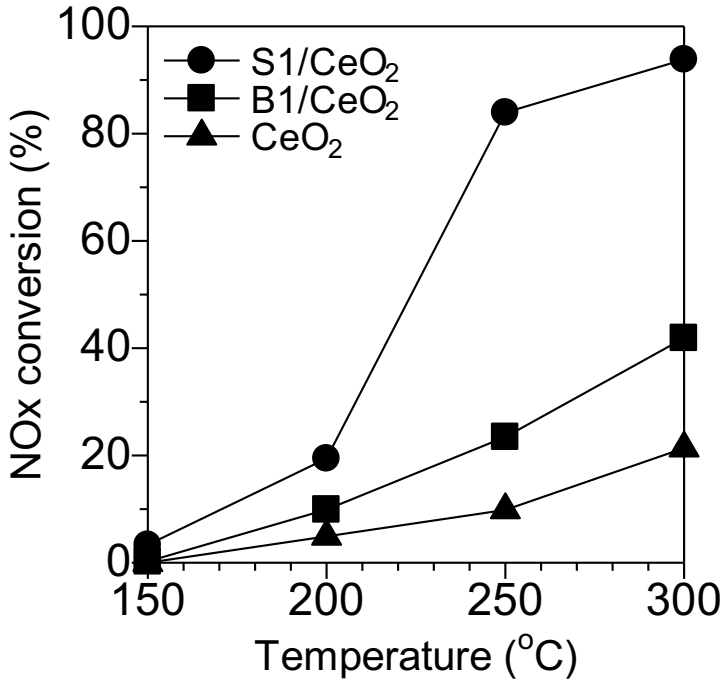

Figure 2. Temperature dependence of NOx conversion over various catalysts (30 mg) under 0.1% NO + 0.1% NH_3 + 10% O_2 balanced with He (total flow 100mL/min).

3.3.2 Structure of Sulfate Species

DFT calculations combined with *ab initio* thermodynamic analysis were conducted to further clarify the plausible structures of the supported sulfate species. This method enables the assessment of the most stable structure under reaction conditions by calculating the relative Gibbs free energies (ΔG). The valence state of S was set to 6+ for all structures. As shown in Figure 3 (top), H_2SO_4 on CeO_2 (111) surface, named H_2SO_4/CeO_2, SO_4^{2-} on CeO_2 (111) with one oxygen vacancy (SO_4^{2-}/CeO_2 with O vacancy), $H_2S_2O_7$ on CeO_2 (111) ($H_2S_2O_7/CeO_2$), and $S_2O_7^{2-}$ on CeO_2 (111) with one oxygen vacancy ($S_2O_7^{2-}$ with O vacancy) were considered as possible structures. Note that only the most stable structures for each chemical formulation obtained are shown for clarity. A 3D phase diagram of the S oxide species is shown in Figure 3A (bottom), which

shows the dependence of the lowest relative Δ*G* on the temperature and partial pressure of O_2. The result shows that the thermodynamic stability of the model structures around the reaction conditions (*T* = 300-350 °C, P_{O2} = 0.1) increases in the order of H_2SO_4/CeO_2 < $H_2S_2O_7/CeO_2$ < $S_2O_7^{2-}/CeO_2$ with O vacancy < SO_4^{2-}/CeO_2 with O vacancy. The monomeric species are more stable than the dimeric species. As shown in Figure 3B (bottom), a 2D phase shows that the most stable species is the SO_4^{2-} on CeO_2 (111) with one oxygen vacancy. When defects were introduced, the Bader charge of Ce around defects turns to decrease, and the sulfate, SO_4^{2-}, was stabilized over the relatively reduced Ce, which helps to provide the electrons that Ce needs, helping the stabilization of defects.

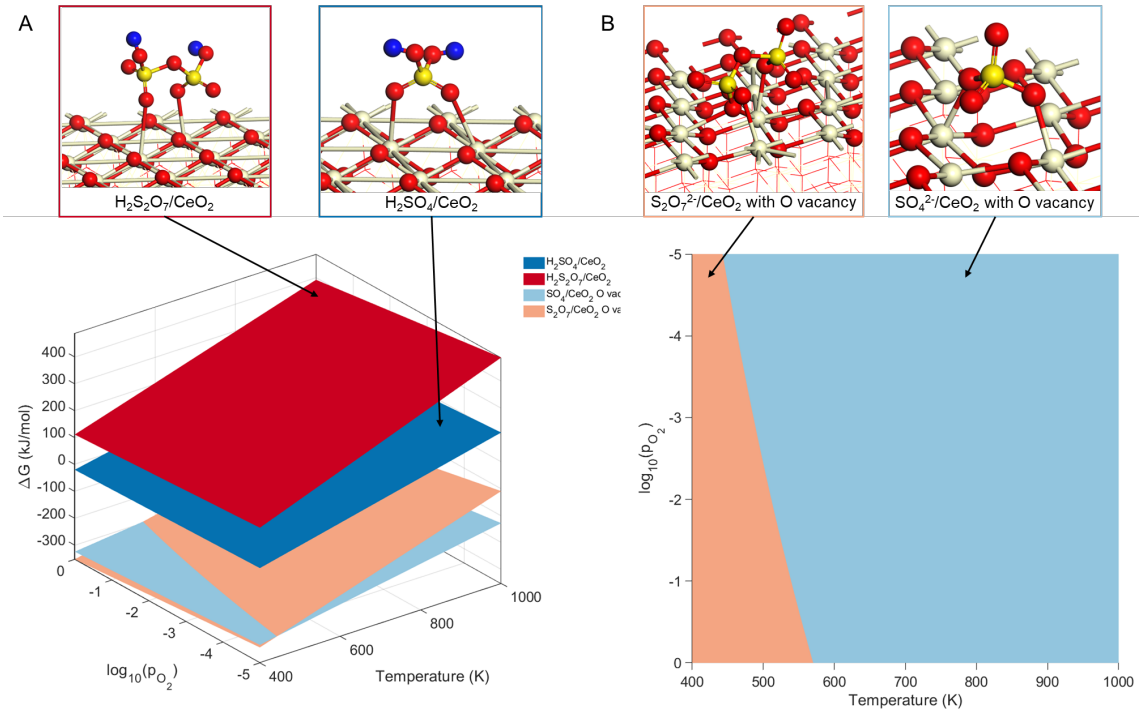

Figure 3. (A) 3D and (B) 2D Phase diagrams show the species with the lowest relative Gibbs free energy (ΔG) in terms of temperature and O_2 partial pressure (log scale) and the two possible structures: dimeric species $S_2O_7^{2-}/CeO_2$(111) and monomeric species SO_4^{2-}/CeO_2(111). All calculations were performed by VASP; yellow: S; red: O; white: Ce, Blue: H.

3.3.3 *Operando* UV-Vis study for transient reactions

We carried out *operando* UV-Vis experiments at 350 °C to figure out the mechanistic reasons on the sulfate-promoted NH_3–SCR activity of CeO_2. First, UV-Vis measurement was carried out for $S1/CeO_2$ under 0.1% NO + 0.1% NH_3. As shown in Figure 4A, introduction of NO + NH_3 to the sample gave a broad band in the visible reign as well as blue shift of a large adsorption band centered around 350-450 nm. Difference spectra with respect to the spectrum before the introduction of NO + NH_3 are shown in Figure 4C. With the increase in the time

of NO + NH_3 flow, a broad peak centered around 570 nm was intensified, while a sharp negative peak around 427 nm was also intensified. According to the literature, the adsorption at 570 nm is assigned to Ce^{3+} species with oxygen defect,[41,42] while the adsorption at 427 nm is assigned to charge transfer between O and Ce^{4+} of CeO_2.[41–43]

For quantitative analysis of the absorption at 570 nm due to the reduced Ce^{3+} species, *in situ* UV-vis experiments for S1/CeO_2 were carried out during H_2 pulse titration at 350 °C. The sample was first pretreated under 2% H_2 (15 min) and then 10% O_2 (15 min) for 2 cycles at 500 °C. Then, time-resolved UV-Vis spectra (Figure S2) were recorded while the 10% H_2 (1 mL) was repeatedly pulsed to the sample. The difference spectra with respect to the oxidized sample shows a broad band centered around 570 nm whose spectral feature is similar to that observed under NO + NH_3 (Figure 4C). Assuming the Ce^{4+}-OH^- species as the main surface Ce species on the oxidized CeO_2, the band at 570 nm can be assigned to the Ce^{3+} species with oxygen defect[41,42,44] produced by the following reaction.

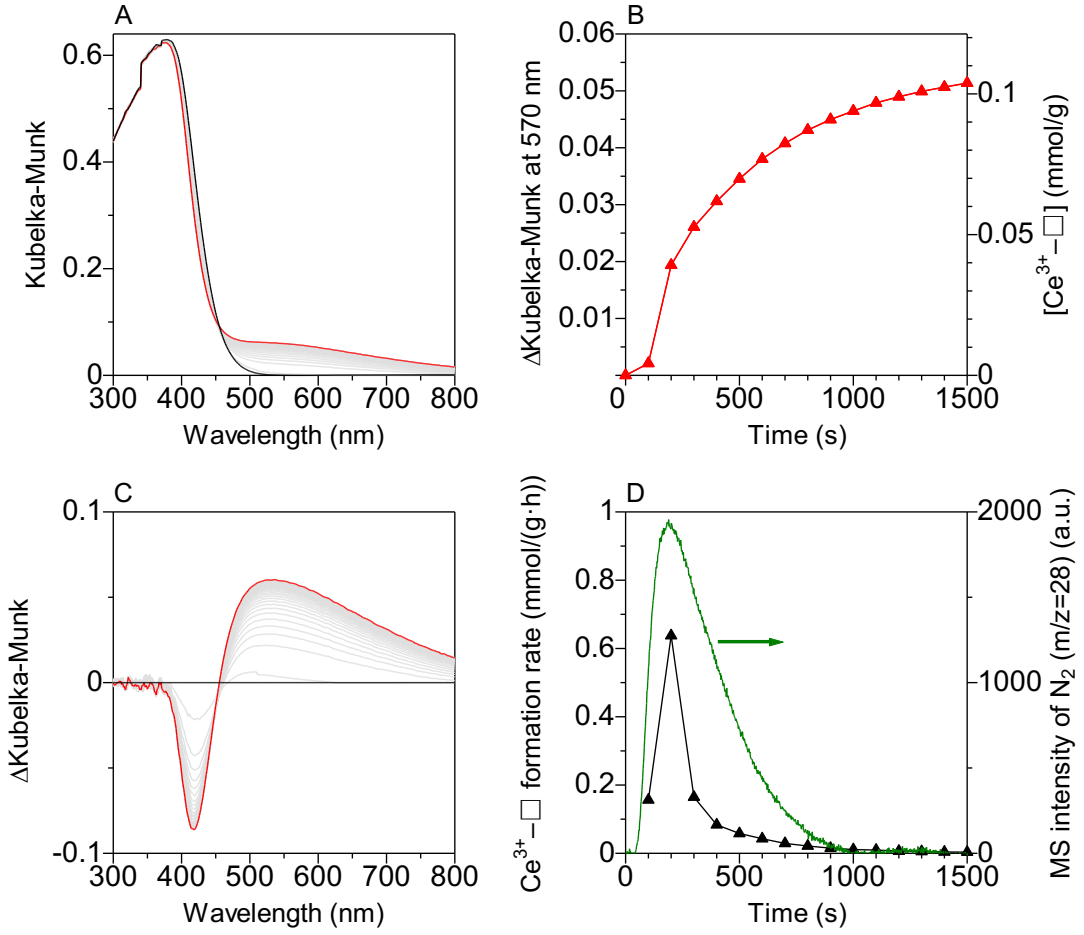

Figure 4. *Operando* UV-Vis results for S1/CeO_2 under 0.1% NO + 0.1% NH_3 at 350 °C. (A) Original UV-Vis spectra, (B) time dependence of the signal intensity

at 570 nm due to Ce^{3+}-□, (C) difference spectra, and (D) time dependence of the formation rates of Ce^{3+}-□ and relative rates of N_2 formation (MS intensity for m/z = 28).

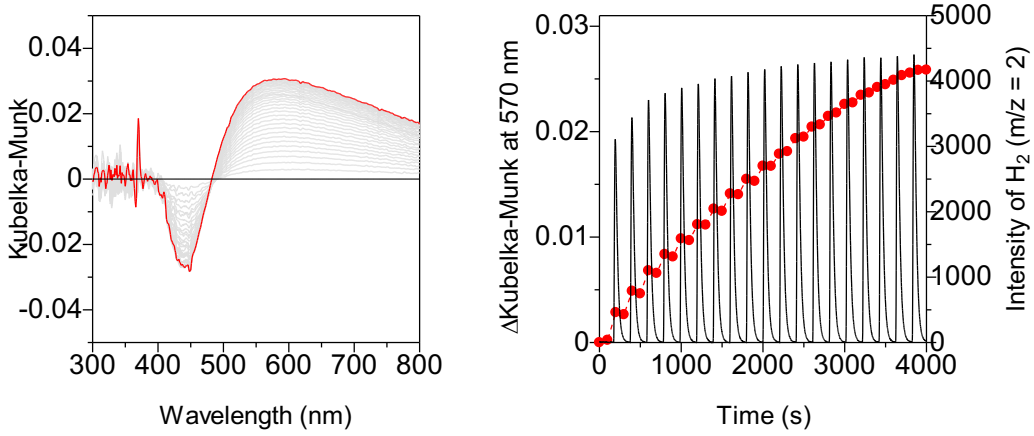

Figure S2. In situ UV-Vis spectra of S1/CeO_2 during repeated H_2 pulse (1 mL of 10% H_2/He) at 500 °C (left). Time-dependence of the Kubelka-Munk function at 570 nm (●) and MS intensity of m/z = 2 (black line) during the in situ UV-vis experiment (right).

The quantitative analysis was carried out by applying the result from Figure S2. The H_2 consumption amount was calculated by operando H_2 pulse. The change in the KM function at 570 nm from the UV-Vis spectrum was plotted to record the change in the valence state of Ce.
The oxygen vacancy on Ce surface can be formed by following reaction:

$CeO_2 + H_2 \rightarrow CeO\text{-}□ + H_2O$
Since one vacancy was formed by consuming one H_2 molecule, the correlation between change at 570 nm and consumption amount of H_2 was formed. 2 mmol/g of oxygen vacancies were formed when KM function changing 1 unit in UV-Vis.
During the above experiment, the relative concentration of H_2 in the outlet gas mixture was monitored by MS (Figure S2). The Kubelka-Munk function at 570 nm is also plotted in Figure S2. Based on the results, the extinction coefficient for the band due to the Ce^{3+}-□ species is calculated assuming the above stoichiometry. Using this extinction coefficient, the peak intensity at 570 nm under NO + NH_3 (Figure 4B) can be converted to the number of the Ce^{3+}-□ species. Numerical differentiation of this plot ($\Delta[Ce^{3+}\text{-}□]/\Delta t$ vs t) gives the time dependence of the formation rates of the Ce^{3+}-□ species (Figure 4D). The MS intensity for m/z = 28, that is the relative rates of N_2 formation, is also plotted in Figure 4D. Clearly, the kinetic curve for the formation of the Ce^{3+}-□ sites showed similar time

dependence to that the N_2 formation; both of the curves showed volcano-type shape with the maximum rate around 200 s. The formation of N_2 and the Ce^{3+}-□ species both finished in 1000 s. Considering the well-established stoichiometry of the reduction half cycle of NH_3–SCR. [6,13,20,23,25,26,45], the results suggest that the reduction half cycle for S1/CeO_2 is described by the following reaction:

Ce^{4+}-OH^- + NO + NH_3 → Ce^{3+}-□ + N_2 + $2H_2O$

After the experiment for the reduction half cycle, followed by purging the cell with He, 10% O_2 was introduced to the reduced S1/CeO_2. Figure 5A shows UV-Vis spectra recorded during the oxidation half cycle. Figure 5B shows the difference spectra with respect to the spectrum before the experiment in Figure 4. The peak intensity at 570 nm due to the Ce^{3+}-□ sites decrease with the time of O_2 flow, while the negative signal at 427 nm due to CeO_2 charge transfer between O and Ce^{4+} decreased with time. The results suggest that the oxidation half cycle for S1/CeO_2 is described by the following reaction:

$$Ce^{3+}\text{-}\square + \frac{1}{4}O_2 + \frac{1}{2}H_2O \rightarrow Ce^{4+}\text{-}OH^-$$

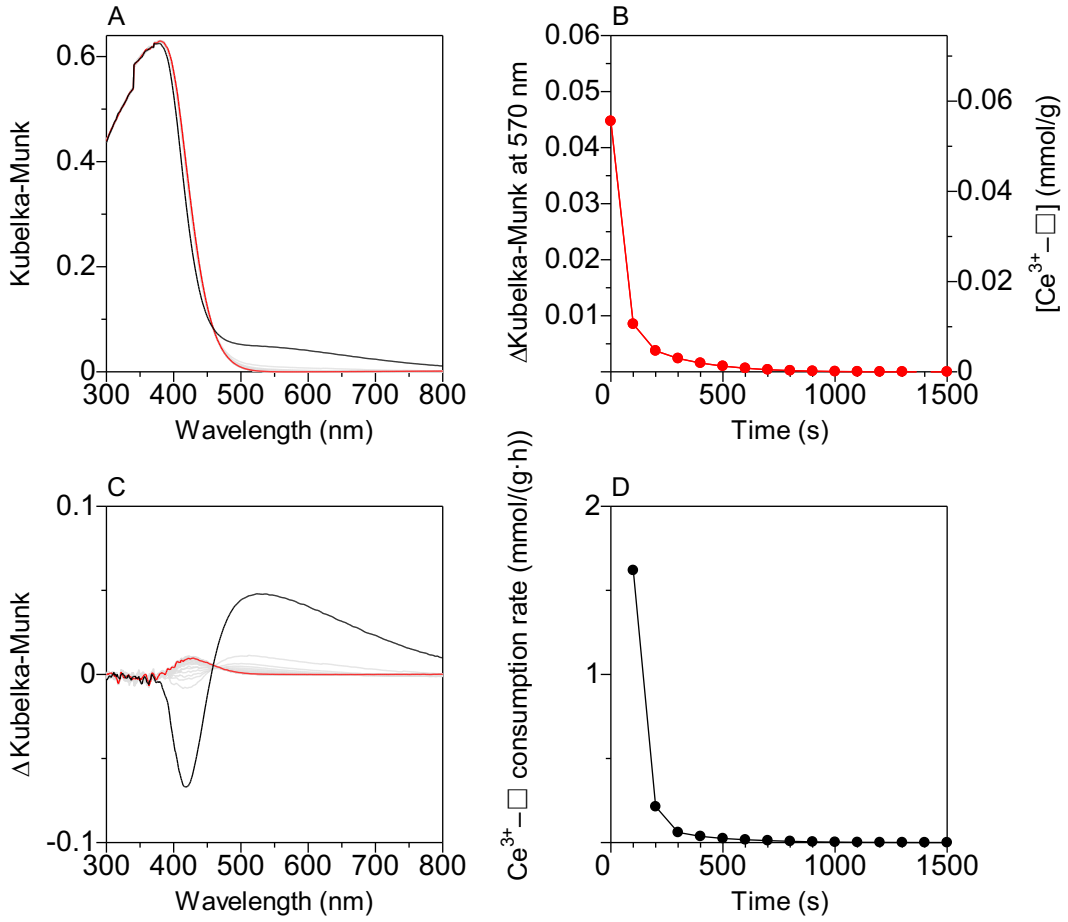

Figure 5. *Operando* UV-Vis results of S1/CeO_2 under 10% O_2 at 350 °C. (A) Original UV-Vis spectra, (B) kinetic plot for consumption of Ce^{3+}-□, (C) difference spectra, and (D) kinetic plot for the rates of Ce^{3+}-□ consumption. The experiment was carried out after the reduction of the sample under NO + NH_3 (Figure 4), followed by He purge for 10 min.

The intensity of the band due to the Ce^{3+}-□ sites is plotted in Figure 5B as a function of the re-oxidation time. The initial slope of the kinetic curve in Figure 5B is steeper than that in Figure 4B, indicating that the oxidation half cycle is faster than the reduction half cycle. The initial rate of the oxidation half cycle (mmol/g·h) in Figure 5D is also larger than the initial rate of reduction half cycle (Figure 4D). Hence, we conclude that the oxidation half cycle is faster than the reduction half cycle.

To investigate mechanistic reasons on the sulfate-promoted NH_3–SCR activity of CeO_2, the same *operando* UV-Vis experiments were carried out for CeO_2 (Figure 6). The difference spectra of CeO_2 under NO + NH_3 (Figure 6A) gave no peak at 570 nm due to the Ce^{3+}-□ sites. There is no change in the spectra at 570 nm under the subsequent flow of O_2 (Figure 6C). Consequently, the kinetic plots for

the reduction (Figure 6B) and oxidation (Figure 6D) half cycles show that the relative rate of the reduction and oxidation half cycles are nearly zero. These results indicate that pure CeO_2 does not show activity for the reduction and oxidation half cycles under the present conditions.

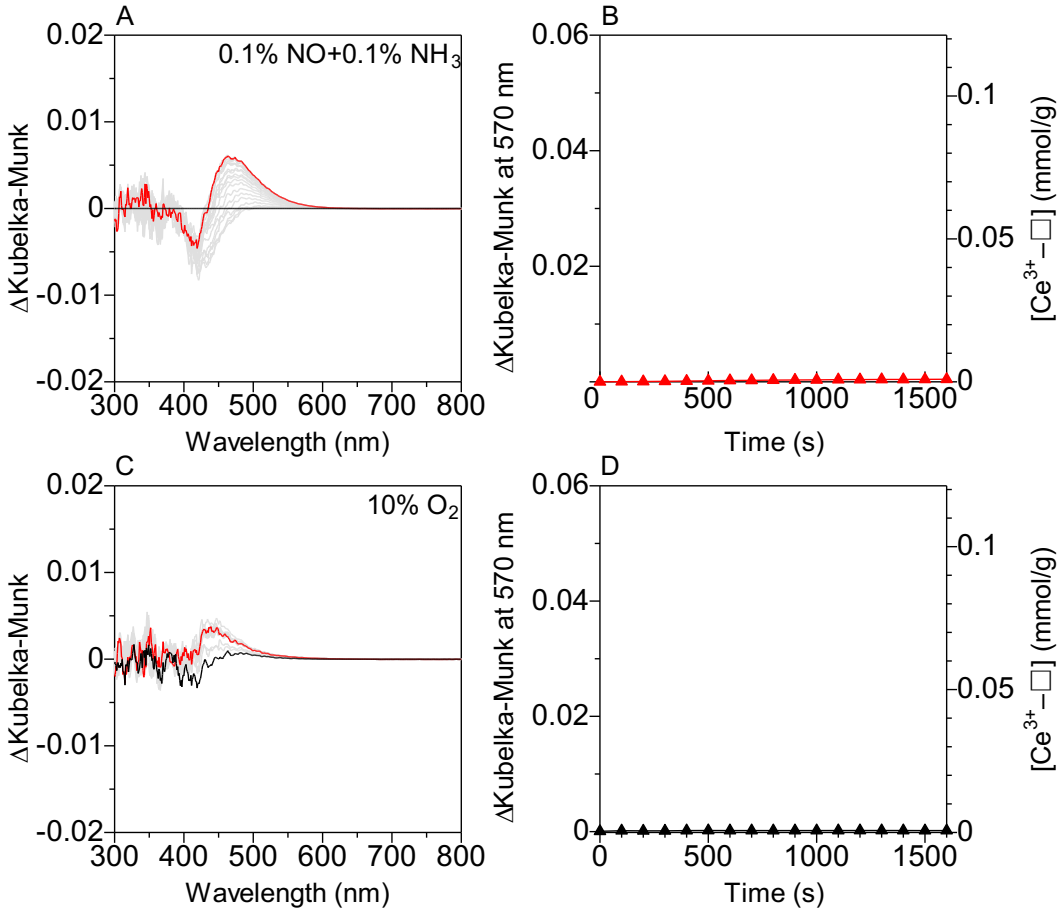

Figure 6. UV-Vis results for CeO_2 at 350 °C under 0.1% NO + 0.1% NH_3 (A, B) and then under 10% O_2 (C, D): difference spectra (A, C) and kinetic plots for the defects amount under NO + NH_3 (B) and O_2 (D). Before the introduction of O_2, the sample was purged by He for 10 min.

Based on the operando UV-Vis results shown above, the mechanism of the NH_3–SCR over sulfate-loaded CeO_2 and mechanistic origin of the sulfate-promoted catalytic activity can be discussed as follows. The NH_3–SCR over the S1/CeO_2 catalyst is driven by the cyclic reduction and oxidation half cycles. In the reduction half cycle, the $Ce^{4+}(OH^-)$ species are reduced by NO + NH_3 to yield N_2, H_2O, and Ce^{3+}-□ species. This step is strongly promoted by the sulfate species possibly adjacent to the $Ce^{4+}(OH^-)$ sites. In the oxidation half cycle, the Ce^{3+}-□ species are reoxidized by O_2 to regenerate $Ce^{4+}(OH^-)$ species. A similar redox-type mechanism and a similar promotional role of acidic additives (phosphates) have

been proposed in our previous study [6,13] on the NH_3–SCR mechanism over phosphates-promoted CeO_2 catalysts. We have also proposed that the reduction half cycle on the phosphates-promoted CeO_2 consists of three elementary steps.[13] The $Ce^{4+}(OH^-)$ species are first reduced by NO to yield Ce^{3+}-□ species and gaseous HONO, which then reacts with NH_3 to produce N_2 and H_2O via NH_4NO_2 intermediates.

To discuss the role of sulfate species in the initial reduction of $Ce^{4+}(OH^-)$ species by NO, we carried out operando UV-Vis experiment of S1/CeO_2 under 0.1% NO at 350 °C (Figure 7). Upon exposure to NO, the band centered around 570 nm due to the Ce^{3+}-□ species appeared in difference spectra accompanied by negative peak at 427 nm due to charge transfer between O and Ce^{4+} of CeO_2[43] (Figure 7A). The band intensity for the Ce^{3+}-□ species increased with time of NO flow, and simultaneously the MS signal of NO_2 (m/z = 46) was observed by the MS analysis of the outlet gas (Figure 7B). These results indicate that the $Ce^{4+}(OH^-)$ species on the surface of S1/CeO_2 is reduced by NO to yield the Ce^{3+}-□ species and NO_2 as follows.

$$Ce^{4+}(OH^-) + \frac{1}{2}NO \rightarrow Ce^{3+}\text{-}\square + \frac{1}{2}NO_2$$

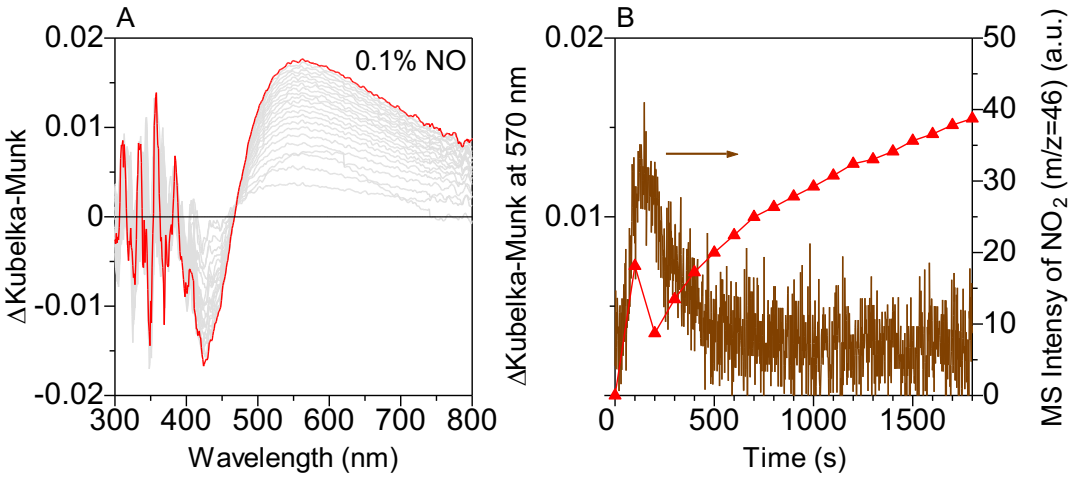

Figure 7. (A) Difference UV-Vis spectra of S1/CeO_2 at 350 °C (A). (B) KM function at 570 nm and MS intensity for NO_2 (m/z = 46) as a function of the time under 0.1% NO.

The reaction rates of NH_3–SCR at 350 °C over S1/CeO_2, B1/CeO_2 and CeO_2 catalysts were estimated under the kinetic conditions (Figure 8A). Figure 8B plots the steady-state NH_3–SCR rates and the transient rates of the reduction half cycle at 350 °C (Figure 4D) as a function of the transient formation rates of the Ce^{3+}-□ species under NO at 350 °C estimated by the *operando* UV-Vis experiment (Figure 8B). For the reduction of the surface $Ce^{4+}(OH^-)$ by NO as the initial step of NH_3–SCR, the rates increase in the order of CeO_2 < B1/CeO_2 < S1/CeO_2. The

rates of the reduction half cycle increase linearly with increase in the formation rates of the Ce^{3+}-□ species under NO. This trend is consistent with the above-mentioned hypothesis that the reduction of $Ce^{4+}(OH^-)$ by NO is the initial step of the reduction half cycle. The steady-state NH_3–SCR rates also cycle increase linearly with increase in the formation rates of the Ce^{3+}-□ species under NO. This trend is also consistent with the hypothesis that the reduction of $Ce^{4+}(OH^-)$ by NO is the initial step of the NH_3–SCR.

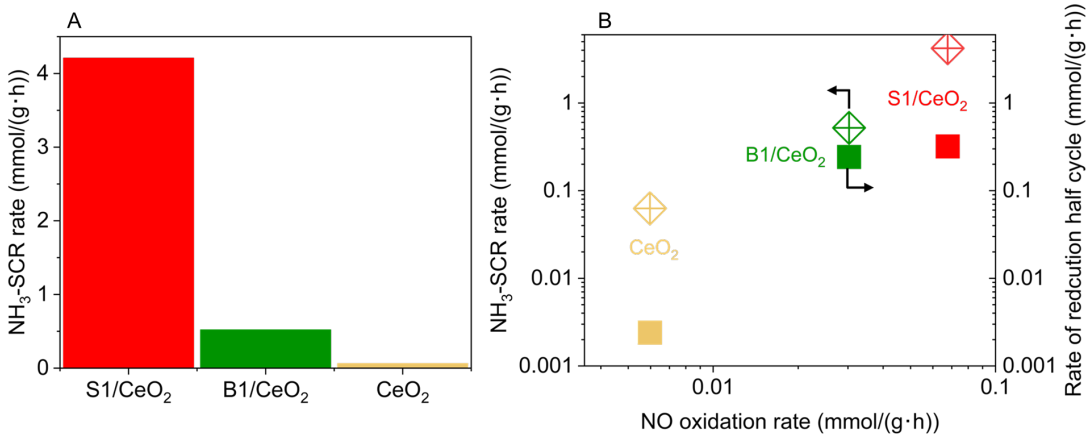

Figure 8. Comparison of catalytic activity (A) and NO reduction rate vs NH_3-SCR rate for reduction half cycles (B) over $S1/CeO_2$, $B1/CeO_2$ and CeO_2 at 350 °C. (A) steady-state rates of NH_3–SCR, (B) initial rate of $Ce^{4+}(OH^-)$ reduction by NH_3 + NO (Figure 4, 6, S1), initial rate of $Ce^{4+}(OH^-)$ reduction by NO (Figure 7, S2, S3).

3.3.4 ME-UV-Vis under NO + O_2 conditions

To better understand the Ce redox cycle during the initial stage of the reduction half cycle, we performed a ME-UV-Vis experiment. Under NO + O_2 reaction conditions over $S1/CeO_2$ at 350 °C, the NO concentration was modulated (0.1% or 0%) every 300 s in a continuous O_2 flow. Although no distinct changes were observed in the time-resolved spectra (Figure 9, top), two broad bands around 425 nm and 530 nm were clearly detected in the phase-resolved spectra (Figure 9, bottom). The band at 425 nm is attributed to charge transfer between Ce^{4+} and O species, while the band at 530 nm corresponds to the Ce^{3+}-□ species.[41–43] These signals appear in inverse phase to each other. The ME-UV-vis result indicates that Ce^{4+} is reduced by NO to form Ce^{3+} and an oxygen defect, and subsequently, the Ce^{3+}-□ site is re-oxidized by O_2 to regenerate Ce^{4+}. The complete inverse phase angles of the Ce^{4+} (φ^{PSD} = 280°) and the Ce^{3+}-□ (φ^{PSD} = 100°) bands confirm that NO oxidation over the $S1/CeO_2$ surface is driven by the redox cycle between Ce^{4+} and Ce^{3+}-□ sites.

It is noteworthy that the intense Ce^{4+} band in the time-resolved spectra shows no significant change, indicating that majority of Ce species remain in their original

state (Ce^{4+}). After PSD analysis, which eliminates signals from unchanged species of Ce, the reduced Ce species were clearly observed. Based on the difference in the Ce^{4+} band intensity in the time-resolved and phase-resolved spectra, the fraction of redox active Ce sites was estimated to be 0.7% of the total Ce atoms. Considering the surface area of S1/CeO_2 and assuming the (111) facet as the representative surface of CeO_2, approximately 4% of the Ce atoms are located on the surface of S1/CeO_2. The quantitative analysis suggests that about 18% of the surface Ce sites act as the redox-active centers under NO oxidation conditions.

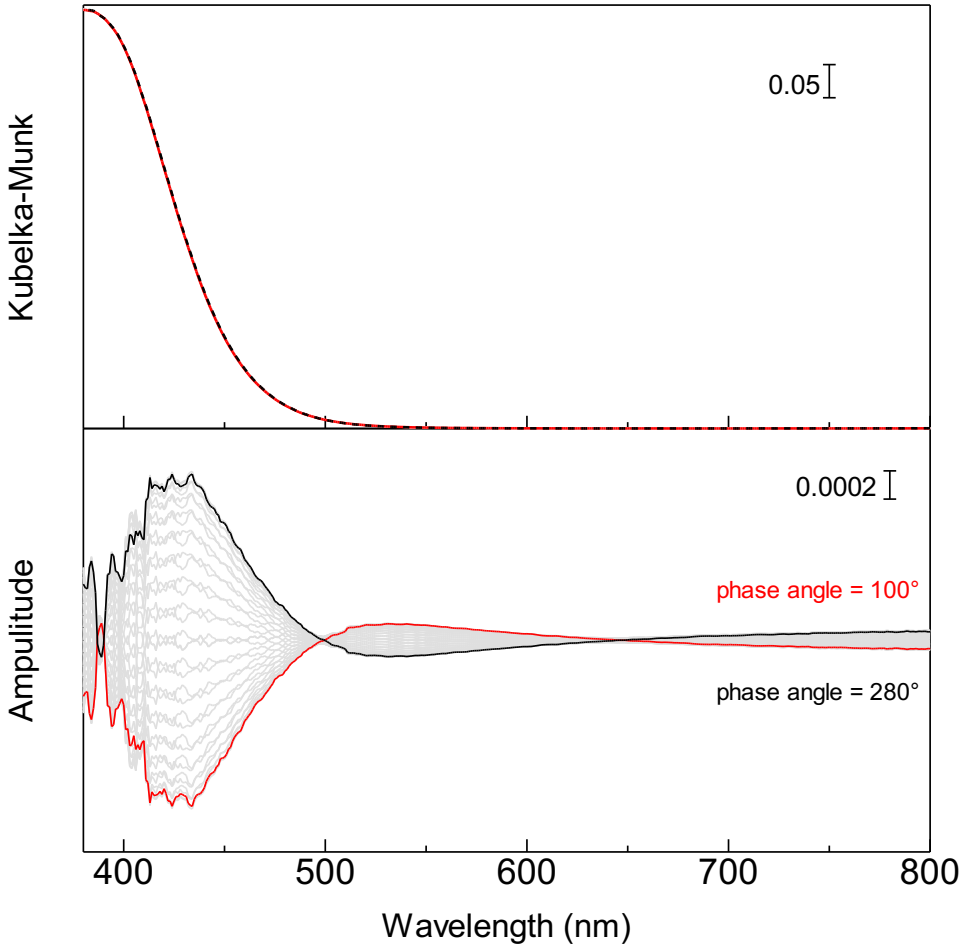

Figure 8. Modulation excitation UV-Vis spectra of S1CeO_2 at 350 °C under alternating gas flows of 0.1% NO + 10% O_2 and 10% O_2, with switching every 300 s. Top: time-resolved UV-Vis spectra with average (red line: end of NO period, black dotted line: end of O_2 period); bottom: phase-resolved spectra without average (red line: phase angle = 100°, black line: phase angle = 280°).

3.3.5 ME-XANES under NO + O_2 conditions

ME-XAS was carried out to investigate the dynamic redox cycle during the NO + O_2 reaction over S1/CeO_2. Under reaction condition at 350 °C, the NO concentration (0.5% or 0%) was modulated every 300 s in a continuous O_2 flow. No clear changes were observed in the time-resolved spectra (Figure 9 top), and the spectral features were consistent with those of CeO_2, indicating that the majority of Ce species are not involved in the redox cycle. In contrast, the phase-resolved spectra revealed changes in the oxidation state of a trace amount of Ce changed (Figure 9 bottom). A peak at 5725 eV, attributed to Ce^{3+} species, and two peaks at 5735 and 5740 eV, corresponding to Ce^{4+} species, were clearly observed. The signals for Ce^{4+} (φ^{PSD} = 290°) and Ce^{3+} (φ^{PSD} = 110°) emerged in opposite phase angles. These results demonstrate that only a small fraction of Ce species participate in the $Ce^{4+} \leftrightarrow Ce^{3+}$ redox cycle during NO oxidation reaction over S1/CeO_2. Based on the difference in the intensity of the Ce^{4+} signal at 5738 eV between deconvoluted time-resolved spectra[46–48] (Figure 10) and phase-resolved spectra, the fraction of the redox-active Ce sites was calculated to be 0.4% of the total Ce atoms, corresponding to 10% of the surface Ce sites. Thus, the ME-XANES result indicates that 10% of the surface Ce sites function as redox-active centers under NO oxidation conditions. This finding is in a good agreement with the quantitative analysis obtained from ME-UV-Vis experiment

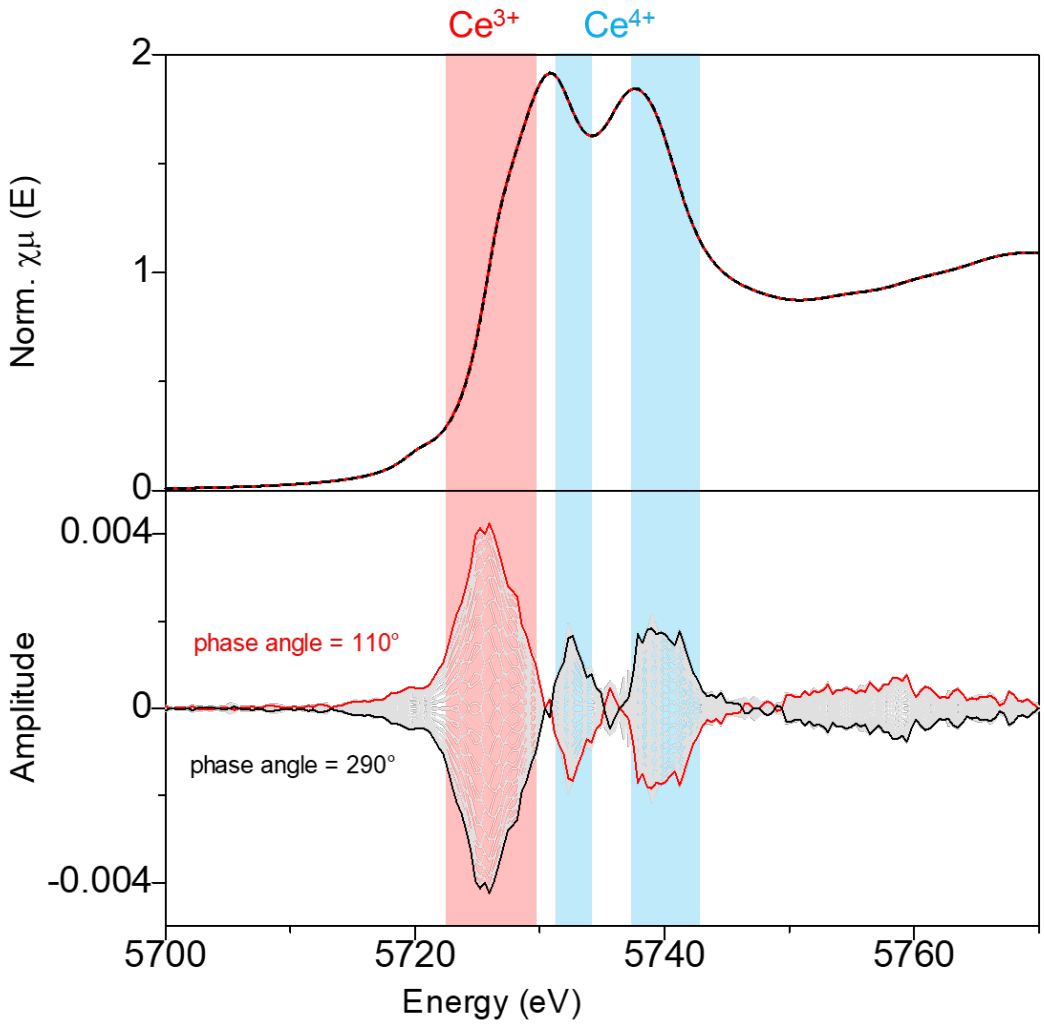

Figure 9. Modulation excitation XANES spectra at 350 °C of S1/CeO_2 under alternating gas flows of 0.5% NO and 10% O_2, with switching every 300 s (total flow: 200mL/min): Top: Time-resolved XANES spectra with average (red line = end of NO period, black dotted line = end of O_2 period); Bottom: Phase-resolved spectra without average (red line: phase angle = 110°, black line: phase angle = 290°).

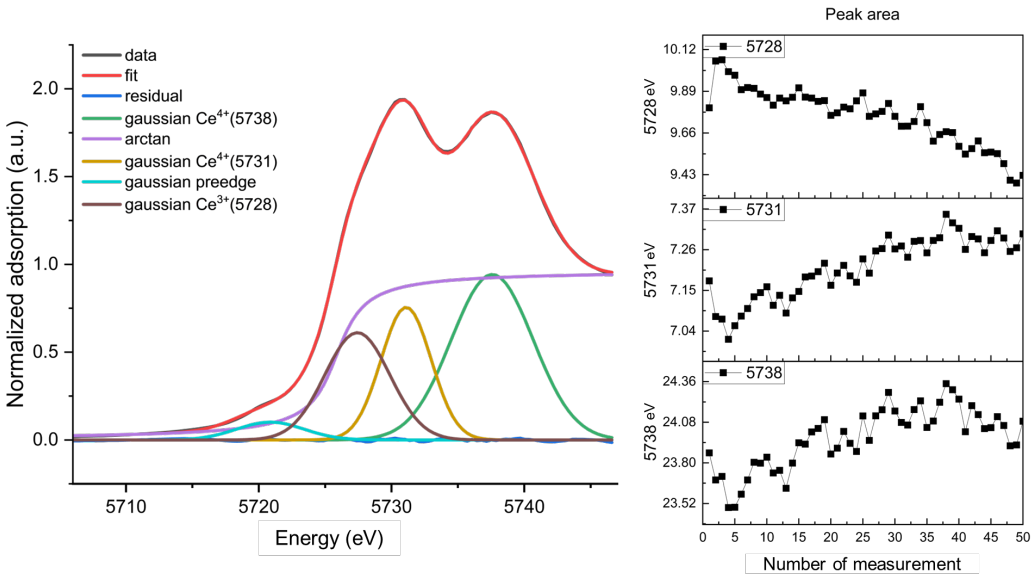

Figure 10. Gaussian peak decomposition of XANES for S1/CeO_2 (Left). Peak area changes during measurement (Right).

3.3.6 EPR for oxygen defect formation

Therefore, ex situ EPR was carried out to probe the formation of oxygen vacancies in CeO_2 and S1/CeO_2, respectively. The enlarged ex-situ EPR spectrum is shown in Figure 11. Most prominently is the signal of a Ce^{4+}-V_o-Ce^{3+} construct, featuring an axial g tensor of g⊥ = 1.966 and gII =1.942. [49] The axial tensor originates most probably from the fact that the Ce^{4+}/Ce^{3+} redox pair is believed to be at or close to the surface and hence features an anisotropic environment.[50] Note that sometimes the signal is attributed to Ce^{3+} species; however, due to the expected short relaxation times of $4f^1$ states as a result of the strong spin–orbit coupling as well as the small g-anisotropy, this signal has been reassigned to the Ce^{4+}-V_o-Ce^{3+} construct [51]. The slight shift between the g-values observed for the CeO_2 and S1/CeO_2 materials might be caused by small changes in the local environment induced by the presence of sulfur. The signal around g = 2.0058 can be attributed to adsorbed O_2^- species at V_o vacancies and to V_o themselves. However, while isolated V_o vacancies usually exhibit an isotropic signal around g = 2.0058, the anisotropic signal with a gII = 2.06 and g⊥ = 2.019 observed here seems to stem from traces of adsorbed O_2^- adsorbed on V_o. [50–55]Similarly to the signal associated with the Ce^4+-V_o-Ce^{3+} construct, a slight shift in the g tenor can be observed for the adsorbed O_2^- species, indicative of a small change in the electronic surrounding.

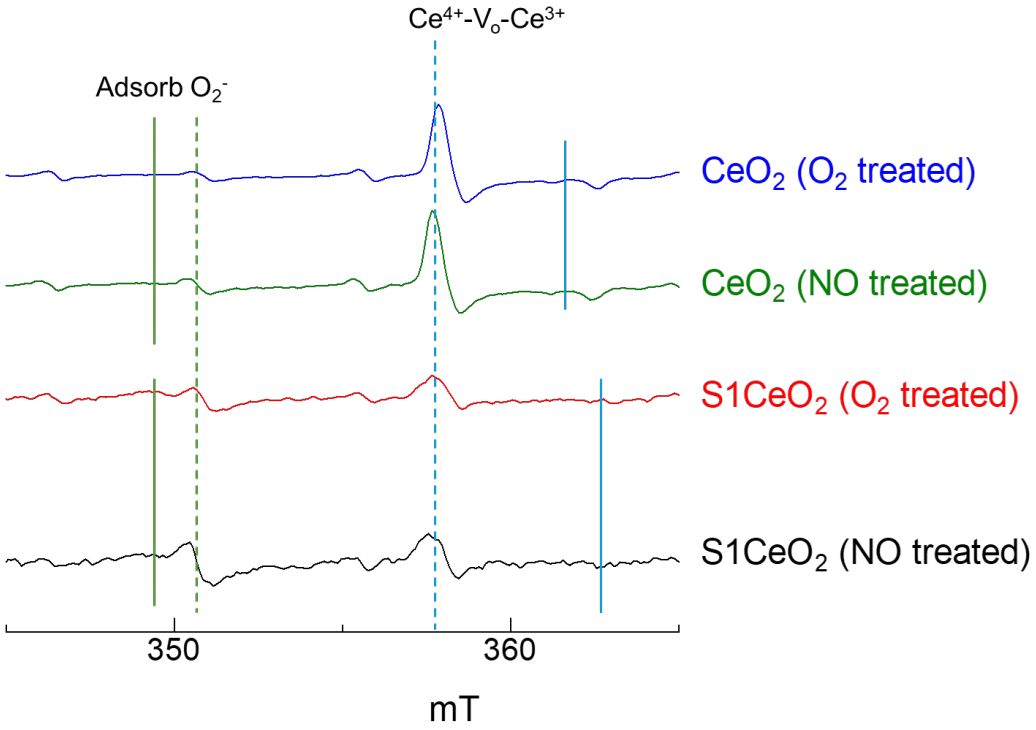

Figure 11. *Ex situ* EPR spectra at 25°C of $S1CeO_2$ and CeO_2 after 350 °C O_2 and NO for 0.5h. Signals are normalized by weight of each sample.

3.3.7 ME-DRIFTS under NO + O_2 conditions

In our previous research on NH_3–SCR mechanism over phosphate- and tungstate-loaded CeO_2, we proposed that adsorbed NO^+ species, possibly formed by the adsorption of nitrous acid (HONO), acts as reactive intermediates;[6,13] NO^+ formed by exposing NO to the catalysts reacted with NH_3 to produce N_2 at low temperatures (below 350°C). To observe intermediate species adsorbed on the catalyst surface, we carried out *in situ* ME-DRIFTS measurement for the NO + O_2 reaction over $S1/CeO_2$ and CeO_2. Under reaction conditions over $S1/CeO_2$ at 350 °C, the NO concentration was modulated between 0.1% and 0 % every 300 s. The time-resolved spectra (top) and the phase-resolved spectra (bottom) for $S1/CeO_2$ and CeO_2 are shown in Figure 12A and 12B, respectively. In the phase-resolved spectra for $S1/CeO_2$, a band at 2245 cm^{-1} with a shoulder at 2198 cm^{-1} is assigned to NO^+ species adsorbed on the anionic oxygen sites of CeO_2.[56–58] A sharp band at 1403 cm^{-1} can be assigned to free nitrate (NO_3^-) species,[59–62] while a broad band at 1616 cm^{-1} with a shoulder at 1565 cm^{-1}corresponds to adsorbed NO_2 and bidentate nitrate (NO_3^-)[61,62]. The absence of NO^+ and NO_3^- signals for CeO_2 indicates that sulfate species are indispensable for the formation of these species on the CeO_2. A band at 3606 cm^{-1} in the hydroxyl region is assigned to acidic CeOH groups.[6,58] Table1 summarizes the observed features in the phase-resolved spectra in Figure 12. The most notable observation from the phase angles is the inverse relationship between

NO^+ (φ^{PSD} = 40°) and free NO_3^- (φ^{PSD} = 220°). This suggests that upon NO introduction, free NO_3^- is consumed, followed by the formation of $NO_{2\ (ad)}$ at a phase angle of 80°. Based on the phenomena observed by ME-DRIFTS, the following reaction is considered to occur within the phase angle of 0° to 180°:

$1/2\ NO_3^- + 1/2\ NO^+ \rightarrow NO_2$

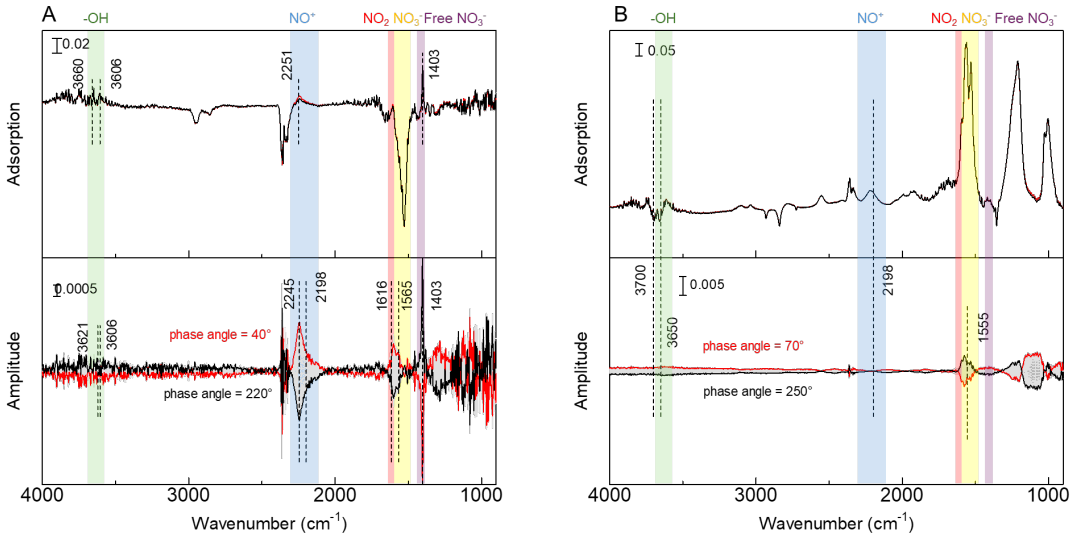

Figure 11. Modulation excitation DRIFT spectra of (A) S1/CeO_2 and (B) CeO_2 under NO modulation between 0.1% and 0% with constant 10% O_2 at 350 °C. (total flow: 100mL/min). Top: Averaged time-resolved spectra (red line: end of NO + O_2 period, black line: end of O_2 period. Bottom: Phase-resolved spectra without average (red line: phase angle = 40° and black line: phase angle = 220°). Table 1 summarizes the observed features in the phase-resolved spectra.

Table 1. Features observed in ME-DRIFTS during NO concentration (0.1% or 0%) modulation experiment.

Wavenumber (cm^{-1})	In-phase angle (°)	Species
1403	220	free NO_3^-
1565	70	NO_3^-
1616	80	$NO_{2\ (ad)}$
2198	40	NO^+
3606	190	OH^-

3.3.8 NH_3–SCR mechanism over sulfate-loaded CeO_2

Summarizing the above results, a possible mechanism of NH_3–SCR over sulfate-loaded CeO_2 is proposed in Figure 12. As a simplified model shown in Figure 12A, NH_3–SCR is based on the reduction of the surface $Ce^{4+}(OH^-)$ species by NO and NH_3 to yield the Ce^{3+}-□ species, N_2, and H_2O (reduction half cycle), followed by the reaction of the Ce^{3+}-□ species with O_2 and water to regenerate the $Ce^{4+}(OH^-)$ species (oxidation half cycle). The sulfate species strongly promote the reduction half cycle.

In a more detailed mechanism (Figure 12B), the reduction half cycle is divided into five individual steps as follows. First, the surface $Ce^{4+}(OH^-)$ species is reduced by NO to yield the Ce^{3+}-□ species and NO_2, which undergoes disproportionation reaction to give adsorbed NO^+ and NO_3^- species. The NO^+ possibly adsorbed on an anionic oxygen (CeO^-) site can react with NH_3 to yield H^+ on the CeO^- site and a free nitrosamide (NH_2NO). NO_3^- species possibly adsorbed on a cationic site can react with NH_3 and H^+ on the CeO^- site to give a free NH_4NO_3 molecule. It is well established that NH_2NO thermally decomposes to give N_2 and H_2O. [63] Our previous works [64] have shown that acidic sites promote the reduction of NH_4NO_3 by NO to yield ammonium nitrite (NH_4NO_2) and NO_2 and the decomposition of NH_4NO_2 to yield N_2 and H_2O.

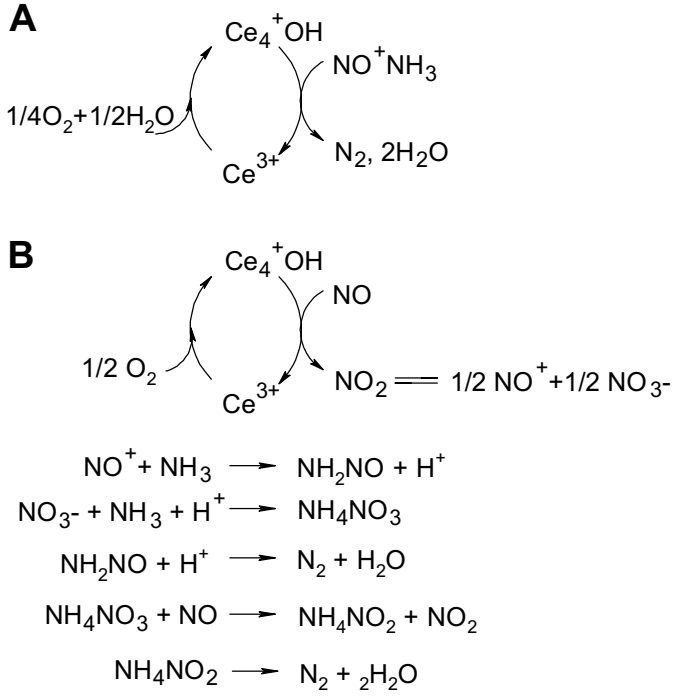

Figure 12. A proposed NH_3-SCR mechanism over sulfate-loaded CeO_2. (A) Overall reaction mechanism. (B) Elementary reaction mechanism for reaction determining step (NO oxidation).

3.4 Conclusion

This study showed comprehensive investigation of the active sites and reaction mechanism for NH_3−SCR over sulfate-loaded ceria, and the following conclusions were drawn. SO_4^{2-} and $S_2O_7^{2-}$species are the dominant sulfate species on the catalysts under the experimental conditions. The $Ce^{4+}(OH^-)$ species, possibly located adjacent to the sulfate species, are reduced by NO + NH_3 to produce N_2, H_2O, and Ce^{3+} species through an NO^+ intermediate (reduction half-cycle). The Ce^{3+} species are subsequently reoxidized by O_2 (oxidation half-cycle). The reduction half-cycle begins with the reaction between NO and $Ce^{4+}(OH^-)$, initially generating NO^+, followed by the formation of Ce^{3+} and gaseous HONO. The HONO then reacts with NH_3 to produce N_2 and H_2O via NH_4NO_2 intermediates. These fundamental insights can lead to rational design of deNOx catalysis.

3.5 References

(1) Beale, A. M.; Gao, F.; Lezcano-Gonzalez, I.; Peden, C. H. F.; Szanyi, J. *Chem. Soc. Rev.* **2015**, *44* (20), 7371–7405.

(2) Shan, Y.; Du, J.; Zhang, Y.; Shan, W.; Shi, X.; Yu, Y.; Zhang, R.; Meng, X.; Xiao, F. S.; He, H. *Nat. Sci. Rev* **2021**, *8* (10), nwab010.

(3) Lai, J. K.; Wachs, I. *ACS Catal* **2018**, *8* (7), 6537–6551.

(4) Zhou, J.; Guo, R. T.; Zhang, X. F.; Liu, Y. Z.; Duan, C. P.; Wu, G. L.; Pan, W. *Energy Fuels* **2021**, *35* (4), 2981–2998.

(5) Inomata, Y.; Kubota, H.; Hata, S.; Kiyonaga, E.; Morita, K.; Yoshida, K.; Sakaguchi, N.; Toyao, T.; Shimizu, K.; Ishikawa, S.; Ueda, W.; Haruta, M.; Murayama, T. *Nat. Commun* **2021**, *12* (1).

(6) Kubota, H.; Qian, Y.; Mine, S.; Toyao, T.; Nuguid, R. J. G.; Buttignol, F.; Ferri, D.; Shimizu, K. *ChemCatChem* **2025**, *17* (4), e202401839.

(7) Gu, T.; Liu, Y.; Weng, X.; Wang, H.; Wu, Z. *Catal. Commun* **2010**, *12* (4), 310–313.

(8) Zhang, L.; Zou, W.; Ma, K.; Cao, Y.; Xiong, Y.; Wu, S.; Tang, C.; Gao, F.; Dong, L. *J. Phys. Chem. C* **2015**, *119* (2), 1155–1163.

(9) Ma, L.; Xie, R.; Li, Z.; Qu, Z.; Yan, N.; Li, J. *ACS Catal* **2021**, *11* (21), 13119–13139.

(10) Xie, Q.; Cai, Y.; Zhang, L.; Hu, Z.; Li, T.; Wang, X.; Zeng, Q.; Wang, X.; Sun, J.; Dong, L. *J. Phys. Chem. C* **2021**, *125* (40), 21964–21974.

(11) Zeng, Y.; Wang, Y.; Hongmanorom, P.; Wang, Z.; Zhang, S.; Chen, J.; Zhong, Q.; Kawi, S. *Chem. Eng. J* **2021**, *409*, 128242.

(12) Chen, L.; Janssens, T. V. W.; Vennestrøm, P. N. R.; Jansson, J.; Skoglundh, M.; Grönbeck, H. *ACS Catal* **2020**, *10* (10), 5646–5656.

(13) Zhang, N.; Tong, J.; Miyazaki, S.; Zhao, S.; Kubota, H.; Jing, Y.; Mine, S.; Toyao, T.; Shimizu, K. *Environ. Sci. Technol* **2023**, *57* (43), 16289–16295.

(14) Li, X.; Li, X.; Zhu, T.; Peng, Y.; Li, J.; Hao, J. *Environ. Sci. Technol* **2018**, *52* (15), 8578–8587.
(15) Jiang, S.; Shi, Y.; Sun, Y.; Zhu, T.; Li, X. *Environ. Sci. Technol* **2024**, *58* (50), 22312–22321.
(16) Li, X.; Li, J.; Peng, Y.; Li, X.; Li, K.; Hao, J. *J. Phys. Chem. C* **2016**, *120* (32), 18005–18014.
(17) Lu, S.; Song, L.; Zhou, C.; Su, Z.; Shu, G.; Ma, K.; Yue, H. *Fuel* **2023**, *338*, 127263.
(18) Qian, Y.; Yasumura, S.; Mine, S.; Toyao, T.; Shimizu, K. *Appl. Catal. A Gen.* **2023**, *655*, 119099.
(19) Hu, W.; Selleri, T.; Gramigni, F.; Fenes, E.; Rout, K. R.; Liu, S.; Nova, I.; Chen, D.; Gao, X.; Tronconi, E. *Angew. Chem. Int. Edit* **2021**, *60* (13), 7197–7204.
(20) Liu, C.; Malta, G.; Kubota, H.; Toyao, T.; Maeno, Z.; Shimizu, K. *J. Phys. Chem. C* **2021**, *125* (40), 21975–21987.
(21) He, G.; Lian, Z.; Yu, Y.; Yang, Y.; Liu, K.; Shi, X.; Yan, Z.; Shan, W.; He, H. *Sci. Adv.* **2018**, *4*, eaau4637.
(22) Hu, W.; Zou, R.; Dong, Y.; Zhang, S.; Song, H.; Liu, S.; Zheng, C.; Nova, I.; Tronconi, E.; Gao, X. *J. Catal* **2020**, *391*, 145–154.
(23) Kubota, H.; Toyao, T.; Maeno, Z.; Inomata, Y.; Murayama, T.; Nakazawa, N.; Inagaki, S.; Kubota, Y.; Shimizu, K. *ACS Catal.* **2021**, *11* (17), 11180–11192.
(24) Kubota, H.; Toyao, T.; Maeno, Z.; Inomata, Y.; Murayama, T.; Nakazawa, N.; Inagaki, S.; Kubota, Y.; Shimizu, K. *ACS Catal* **2021**, *11* (17), 11180–11192.
(25) Liu, C.; Kubota, H.; Amada, T.; Kon, K.; Toyao, T.; Maeno, Z.; Ueda, K.; Ohyama, J.; Satsuma, A.; Tanigawa, T.; Tsunoji, N.; Sano, T.; Shimizu, K. *ChemCatChem* **2020**, *12* (11), 3050–3059.
(26) Yasumura, S.; Qian, Y.; Kato, T.; Mine, S.; Toyao, T.; Maeno, Z.; Shimizu, K. *ACS Catal* **2022**, *12* (16), 9983–9993.
(27) Urakawa, A.; Bürgi, T.; Baiker, A. *Chem. Eng. Sci.* **2008**, *63* (20), 4902–4909.
(28) Greenaway, A. G.; Marberger, A.; Thetford, A.; Lezcano-González, I.; Agote-Arán, M.; Nachtegaal, M.; Ferri, D.; Kröcher, O.; Catlow, C. R. A.; Beale, A. M. *Chem. Sci.* **2020**, *11* (2), 447–455.
(29) Ferri, D.; Newton, M. A.; Nachtegaal, M. *Top. Catal.* **2011**, *54* (16–18), 1070–1078.
(30) Müller, P.; Hermans, I. *Ind. Eng. Chem. Res.* **2017**, *56* (5), 1123–1136.
(31) Nuguid, R. J. G.; Ferri, D.; Marberger, A.; Nachtegaal, M.; Kröcher, O. *ACS Catal.* **2019**, *9* (8), 6814–6820.
(32) Kubota, H.; Qian, Y.; Mine, S.; Toyao, T.; Nuguid, R. J. G.; Buttignol, F.; Ferri, D.; Shimizu, K. *ChemCatChem* **2025**, *17* (4), e202401839.

(33) Nuguid, R. J. G.; Elsener, M.; Ferri, D.; Kröcher, O. *Appl. Catal. B: Environ.* **2021**, *298*, 120629.
(34) Marberger, A.; Petrov, A. W.; Steiger, P.; Elsener, M.; Kröcher, O.; Nachtegaal, M.; Ferri, D. *Nat. Catal.* **2018**, *1* (3), 221–227.
(35) Ravel, B.; Newville, M. *J. Synchrotron Radiat.* **2005**, *12* (4), 537–541.
(36) Kresse, G.; Furthmüller, J. *Comput. Mater. Sci.* **1996**, *6* (1), 15–50.
(37) Kresse, G.; Furthmüller, J. *Phys. Rev. B* **1996**, *54* (16), 11169.
(38) Perdew, J. P.; Ruzsinszky, A.; Csonka, G. I.; Vydrov, O. A.; Scuseria, G. E.; Constantin, L. A.; Zhou, X.; Burke, K. *Phys. Rev. Lett.* **2008**, *100* (13), 136406.
(39) Blöchl, P. E. *Phys. Rev. B* **1994**, *50* (24), 17953.
(40) Grimme, S.; Ehrlich, S.; Goerigk, L. *J. Comput. Chem.* **2011**, *32* (7), 1456–1465.
(41) Seminko, V.; Maksimchuk, P.; Bespalova, I.; Masalov, A.; Viagin, O.; Okrushko, E.; Kononets, N.; Malyukin, Y. *Phys. Status Solidi B* **2017**, *254* (4), 1600488.
(42) Hoyer, H.; Hess, C. *J. Phys. Chem. C* **2024**, *128* (50), 21377–21386.
(43) Portillo, M. C.; Moreno, O. P.; Mora-Ramírez, M. A.; Santiesteban, H. J.; Avendaño, C. B.; Bernal, Y. P. *Optik (Stuttg)* **2021**, *248*, 168178.
(44) Ju, T. J.; Wang, C. H.; Lin, S. D. *Catal. Sci. Technol.* **2019**, *9* (9), 2118–2124.
(45) Yasumura, S.; Qian, Y.; Toyao, T.; Maeno, Z.; Shimizu, K. *J. Phys. Chem. C* **2022**, *126* (27), 11082–11090.
(46) Lee, K. M.; Kim, B.; Lee, J.; Kwon, G.; Yoon, K.; Song, H.; Min, K. H.; Shim, S. E.; Hwang, S.; Kim, T. *Catal. Sci. Technol.* **2024**, *14* (2), 279–292.
(47) Fernandes, V.; Graff, I. L.; Varalda, J.; Amaral, L.; Fichtner, P.; Demaille, D.; Zheng, Y.; Schreiner, W. H.; Mosca, D. H. *J. Electrochem. Soc.* **2011**, *159* (1), K27–K33.
(48) Aragón, F. F. H.; Villegas-Lelovsky, L.; Cabral, L.; Lima, M. P.; Mesquita, A.; Coaquira, J. A. H. *NANOSCALE ADV.* **2021**, *3* (5), 1484–1495.
(49) Macchi, C.; Procópio, A. M. S.; Rocha, L. S. R.; Ortega, P. P.; Aldao, C. M.; Granone, L. I.; Nascimento, H. M. S.; Longo, E.; Castro, M. S.; Ivorra, F. D.; Somoza, A.; Moura, F.; Ponce, M. A. *ACS Omega* **2024**, *9* (41), 42172–42182.
(50) Pan, D.; Xu, G.; Lv, L.; Yong, Y.; Wang, X.; Wan, J.; Wang, G.; Sui, Y. *Appl. Phys. Lett.* **2006**, *89* (8).
(51) Rakhmatullin, R. M.; Semashko, V. V.; Korableva, S. L.; Kiiamov, A. G.; Rodionov, A. A.; Tschaggelar, R.; van Bokhoven, J. A.; Paun, C. *Mater. Chem. Phys.* **2018**, *219*, 251–257.
(52) Chiesa, M.; Giamello, E. *Catal. Lett.* **2021**, *151* (12), 3417–3436.

(53) Soria, J.; Martínez-Arias, A.; Conesa, J. C. *J. Chem. Soc., Faraday Trans.* **1995**, *91* (11), 1669–1678.
(54) Martínez-Arias, A.; Fernández-García, M.; Ballesteros, V.; Salamanca, L. N.; Conesa, J. C.; Otero, C.; Soria, J. *L.* **1999**, *15* (14), 4796–4802.
(55) Aboukais, A.; Zhilinskaya, E. A.; Lamonier, J. F.; Filimonov, I. N. *Colloids Surf. A: Physicochem. Eng. Asp.* **2005**, *260* (1–3), 199–207.
(56) Martín-Martín, J. A.; Aranzabal, A.; Finocchio, E.; González-Marcos, M. P.; González-Velasco, J. R. *Catal. Today.* **2025**, *455*, 115309.
(57) Hadjiivanov, K.; Saussey, J.; Freysz, J. L.; Lavalley, J. C. *Catal. Lett.* **1998**, *52* (1), 103–108.
(58) Mihaylov, M. Y.; Ivanova, E. Z.; Vayssilov, G. N.; Hadjiivanov, K. I. *Catal. Today.* **2020**, *357*, 613–620.
(59) Trovarelli, A. *Catal. Rev. - Sci. Eng.* **1996**, *38* (4), 439–520.
(60) Machida, M.; Uto, M.; Kurogi, D.; Kijima, T. *Chem. Mater.* **2000**, *12* (10), 3158–3164.
(61) Qi, G.; Yang, R. T. *J. Phys. Chem. B.* **2004**, *108* (40), 15738–15747.
(62) Davydov, A. **2003**.
(63) Sun, D.; Schneider, W. F.; Adams, J. B.; Sengupta, D. *J. Phys. Chem. A.* **2004**, *108* (43), 9365–9374.
(64) Liu, C.; Malta, G.; Kubota, H.; Toyao, T.; Maeno, Z.; Shimizu, K. *J. Phys. Chem. C.* **2021**, *125* (40), 21975–21987.

Supporting Information

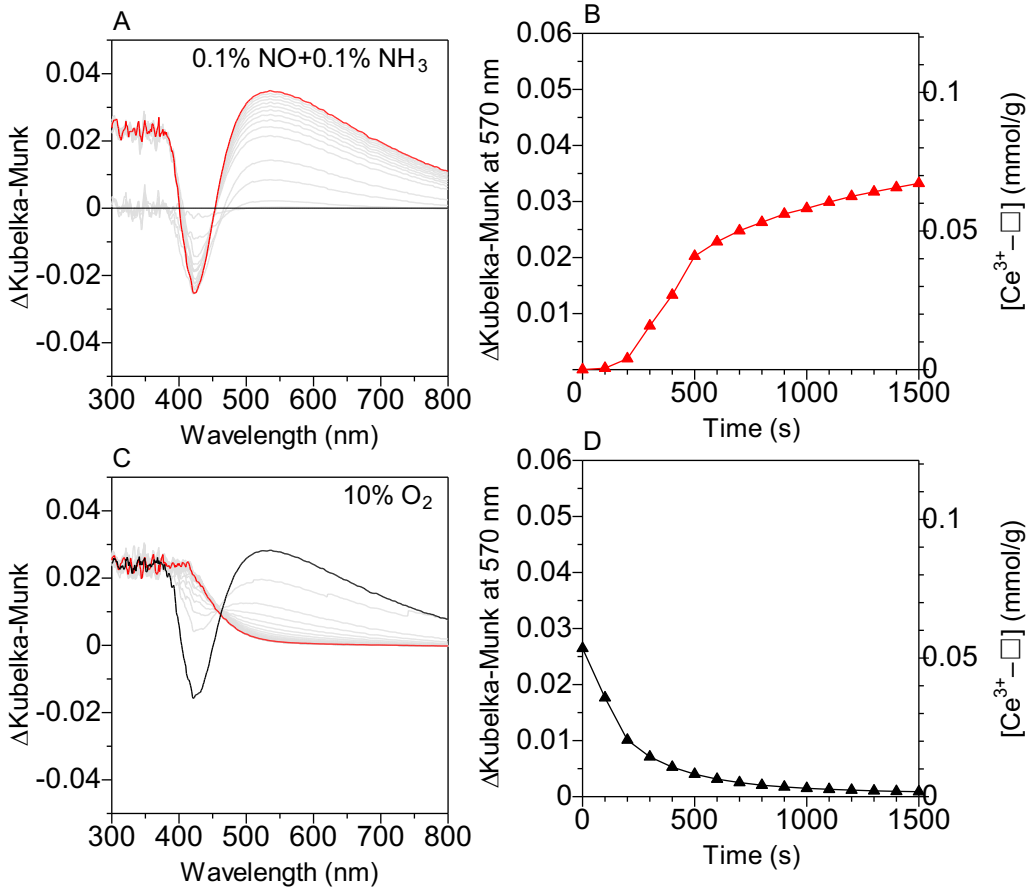

Figure S1. Difference UV-Vis spectra of $B1CeO_2$ (A), (C) at 350 °C and K-M function change at 570 nm (B), (D) of $B1CeO_2$ under 0.1% NO + 0.1% NH_3 (A), (B) / 10% O_2 (C), (D).

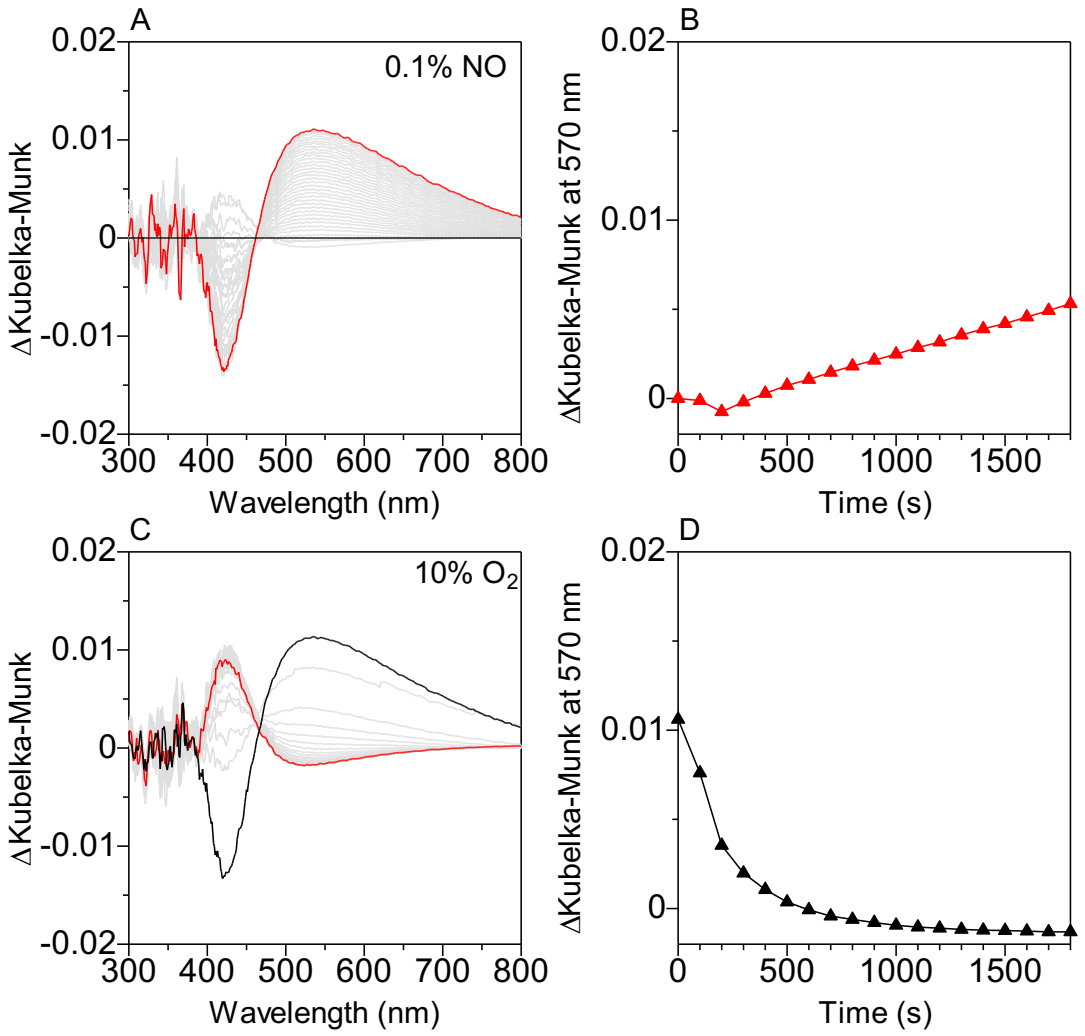

Figure S2. Difference UV-Vis spectra of B1CeO$_2$ (A), (C) at 350 °C and K-M function change at 570 nm (B), (D) of B1CeO$_2$ under 0.1% NO (A), (B) / 10% O$_2$ (C), (D).

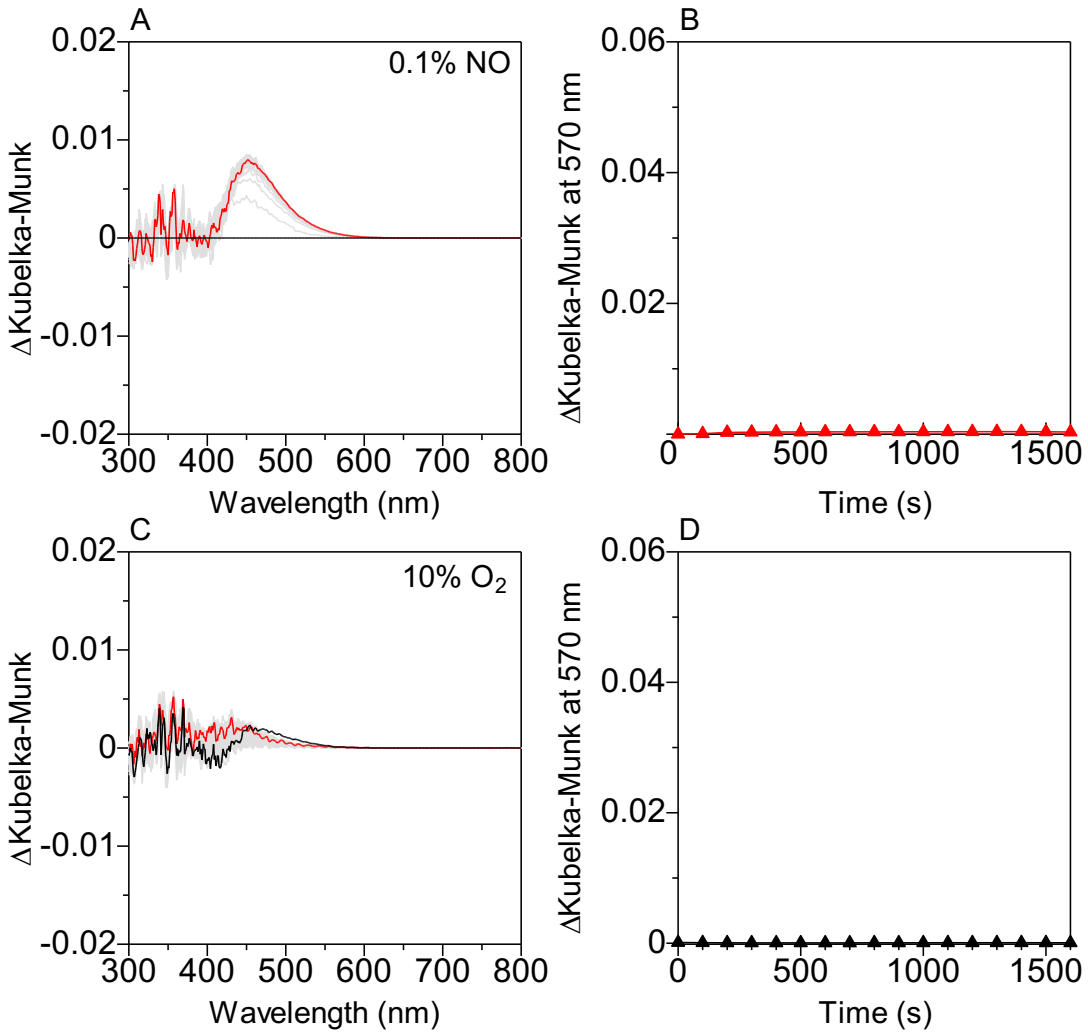

Figure S3. Difference UV-Vis spectra of CeO_2 (A), (C) at 350 °C and K-M function change at 570 nm (B), (D) of CeO_2 under 0.1% NO (A), (B) / 10% O_2 (C), (D).

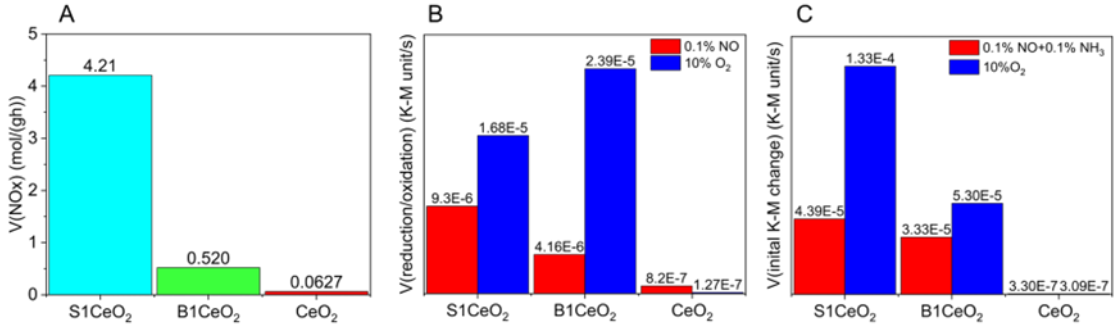

Figure S4. (A) Reaction rate of $S1CeO_2$/$B1CeO_2$/CeO_2 (B)Changing rate of initial slope K-M function at 570 nm under 0.1% NH_3 + 0.1% NO/ 10% O_2. (C) Changing rate of initial slope K-M function at 570 nm under 0.1% NO/ 10% O_2.

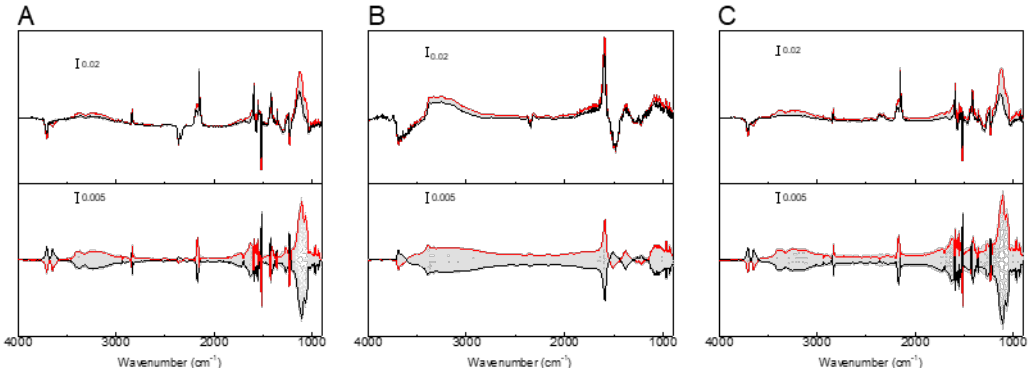

Figure S5. NO modulation excitation over (A) S1/CeO_2, (B) B1/CeO_2 and (C) CeO_2.

Table S1. Fitting parameters of Gaussian peak decomposition in Figure S8.

Species	Ce^{4+} (5738 eV)	Ce^{4+} (5731 eV)	Ce^{3+} (5728 eV)	pre-edge (5720 eV)
Height	7.278 (0.011)	3.574 (0.010)	3.756 (0.011)	0.643 (0.010)
Center	5737.59 (0.00)	5731.10 (0.00)	5727.43 (0.00)	5720.87 (0.00)
Sigma	3.081 (0.000)	1.886 (0.000)	2.451 (0.000)	2.529 (0.000)
	Arctan			
Step	0.965 (0.000)			
E_0	5725.86 (0.00)			
Width	1.581 (0.000)			

Chapter 4

Mechanism of Selective Reduction of N_2O by CO over Fe–ß Catalysts Studied by *In situ/Operando* Spectroscopy

3.1 Introduction

Nitrous oxide (N_2O) can significantly accelerate the greenhouse effect owing to its high global warming potential and long lifetime. Various industrial sectors, including agriculture, transportation, and chemical industries, face challenges in controlling N_2O emissions. To control N_2O emissions from diesel exhaust gas, researchers have studied various catalytic technologies, including direct N_2O decomposition[1–10] and selective catalytic reduction (SCR) of N_2O.[10–19] The direct catalytic decomposition of N_2O is an ideal and economical technology because no reducing agents are required. According to extensive studies, Rh is generally considered the most active catalytic component for the decomposition of N_2O.[2–4,7–9] However, the catalytic N_2O decomposition suffers from serious drawbacks of high reaction temperatures and the strong negative impact of excess O_2 on catalytic activity.[5–9,11,12,19,20] In our previous studies,[3,4] we screened various catalysts for decomposition of 0.1% N_2O under 10% O_2 and found that $RhOx/ZrO_2$ and $RhOx/Ag/Al_2O_3$ show high N_2O conversion above 350 °C even in the presence of excess O_2. In a commercial catalytic system, less expensive catalysts without platinum-group-metals (PMG) should be utilized; however, non-PGM catalysts generally show lower activity for the decomposition of N_2O than Rh-based catalysts. In contrast, non-PGM catalysts, especially Fe-containing zeolites, are known to be effective for the SCR of N_2O using various reductants such as CO[15,16], CH_4[10,13,14,21–28], hydrocarbons[11,26,27,29–31], and NH_3[12,31–36]. Fe-zeolites have also been studied as model catalysts for N_2O reduction by CO[10,17,37–40] or CH_4[10,13,14,27,41] in the absence of O_2. A few studies have reported the use of CO as a reductant for the SCR of N_2O (CO-SCR).[15–17] Among the rare examples of CO-SCR by Fe-zeolites, Zeng et al. [15] demonstrated that an Fe-exchanged ß zeolite shows N_2O conversion at relatively low temperatures (250-400 °C). They showed that the temperature range for CO-SCR is significantly lower than that for N_2O decomposition. The main drawback of CO-SCR is its inhibitory effect on O_2. Li et al.[16] reported that an Fe-exchanged MFI zeolite (Fe-MFI) with cationic Fe as the active species shows higher O_2-tolerance in CO-SCR than comparable catalysts with oligonuclear Fe_xO_y and Fe_2O_3 particles as the

dominant Fe species. The authors proposed that high O_2-tolerance of the Fe-MFI catalyst was due to preferential reactivity of the α-Fe sites with N_2O rather than with O_2, resulting in a higher rate of the N_2O + CO reaction than the O_2 + CO reaction. To design an O_2-tolerant Fe-zeolite catalyst for the CO-SCR, it is necessary to clarify the mechanism underlying the preferential oxidation of CO by N_2O under excess O_2 over specific Fe species.

Following pioneering reports on the selective hydroxylation of CH_4 or phenol by N_2O over Fe zeolites,[42] considerable attention has been paid to the nature of the active oxygen species on Fe zeolites.[14,24,29,30,43,44] On the basis of spectroscopic and theoretical evidence, it is suggested that Fe-exchanged zeolites stabilize a Fe(II) site (called α-Fe site) that dissociates N_2O, forming a highly reactive Fe(III)-O^- or Fe(IV)=O intermediate (called α-Fe-O) that is active for hydroxylation of CH_4[23,38,43–45] or benzene.[29,30] Previous studies on the SCR of N_2O have concluded that the redox mechanism between α-Fe(II) and Fe(III)-O^- (or Fe(IV)=O) is also applicable for the mechanism of N_2O decomposition [20,31] and the SCR of N_2O by CH_4[13,14,18,27,28,41,43,46] over Fe zeolites. Despite many studies on the nature of the α-Fe-O species, no studies have reported *in situ/operando* spectroscopic evidence on the redox mechanism between α-Fe(II) and Fe(III)-O^- for SCR of N_2O by CO over Fe zeolites.

We report herein *in situ* spectroscopic studies (combined with online gas-phase analysis by mass spectrometry) on the reduction and oxidation half cycles of SCR of N_2O by CO over Fe-exchanged beta zeolites (Feß). *In situ* diffuse reflectance UV-vis spectroscopy was utilized to monitor the formation of α-Fe-O during the oxidation of α-Fe(II) species by N_2O and the reaction of α-Fe-O with CO. Under similar transient conditions, X-ray absorption spectroscopy (XAS) was used to monitor the reduction of Fe(III)-αO species by CO to give α-Fe(II) and CO_2, followed by the oxidation of α-Fe(II) by N_2O to regenerate Fe(III)-αO.

4.2 Experimental Section

4.2.1 Catalyst preparation

Fe-exchanged ß catalysts were prepared by aqueous ion exchange of NH_4^+-form ß (Si/Al = 5, supplied by Mitsui Kinzoku Co., 5 g) in $Fe(SO_4)\cdot 7H_2O$ solution (0.05 M or 0.01 M, 75 mL) for 3 h at 25 °C under a N_2 atmosphere. After centrifugation and washing three times with distilled water, the catalysts were dried at room temperature in a fume hood for 72 h. The Fe loading was determined using X-ray

fluorescence analysis (XRF; EDX-700HS, Shimadzu Corp.). The resulting catalysts with Fe loadings of 0.9 wt% and 2.7 wt% were designated as Fe0.9ß and Fe2.7ß, respectively. X-ray diffraction (XRD) patterns were recorded on Rigaku Miniflex software using Cu–Kα radiation from 10 to 80° at 30 kV and 10 mA with a scanning speed of 5°/min. As shown in Figure S1, the XRD pattern of Fe0.9ß (as made) is basically identical to that of Hß (600°C, 1h, air calcination), indicating no change in crystal structure after Fe-exchange.

4.2.2 Catalytic tests

Catalytic tests were performed with the catalysts (typically 30 mg) in a fixed-bed flow reactor under several flowing gas mixtures (total flow rate of 100 mL/min): 0.1% N_2O/0.1% CO/He, 0.1% N_2O/0.1% CO/10% O_2/He, 0.1% N_2O/10% O_2/He, or 0.1% CO/10% O_2/He. The concentrations of N_2O, CO, and CO_2 were analyzed using an IR spectrometer (JASCO FT/IR-4100 with a gas cell) based on calibration standards. The % conversion of N_2O (X_{N2O}) and CO (X_{N2O}) was calculated using the following equations:

$$X_{N2O}\ (\%) = (1 - \frac{C^{out}}{C^{in}}) \times 100$$

$$X_{CO}\ (\%) = (1 - \frac{C^{out}}{C^{in}}) \times 100$$

The reaction rate of N_2O reduction, r_{N2O}, was calculated by the rate expression:
$V_{N2O} = F^0_{N2O}\ \Delta X_{N2O}/W$,
where F^0_{N2O}, ΔX_{N2O}, *and W a*re the molar flow of N_2O at the inlet, the conversion of N_2O, and the catalyst weight, respectively. As shown in Figure S2, nearly linear dependence of the N_2O conversion on the contact time was observed below 60% conversion. Thus, by adjusting the catalyst weight, the reaction rates measurement for Figure 3 and Figure 4 was carried out under the conditions where the conversions of N_2O and CO were below 35%.

4.2.3 *In situ/operando* UV-vis

Operando/in situ diffuse reflectance UV-vis spectra were recorded in an *in situ* flow diffuse reflectance cell using a JASCO V750 spectrometer. The catalyst powder (40 mg) was placed in a diffuse reflectance cell (JASCO HISV-728) with a quartz window connected to a gas-flow system (total flow rate of 100 mL min^{-1}). The center of the smooth sample and spectrometer were connected by an optical fiber. The baseline was obtained with $BaSO_4$ at room temperature. The spectra were measured in a range 250–800 nm. The reflectance was converted to

Kubelka–Munk (KM) intensity. Deconvolution analysis of the spectra was performed with Gaussian functions using PeakFit V4.11. For *operando* UV-vis measurement, 1% N_2O or 1% CO (in He) was introduced to the cell at 350 °C.[47,48] The formation of N_2 (m/z = 28) under N_2O and the formation of CO_2 (m/z = 44) under CO were analyzed using online mass spectrometry (JMS-Q1500GS, JEOL Ltd.).

4.2.4 *In situ* XAS

In situ XAS Fe K-edge spectra were obtained in the transmission mode at the BL01B1 beamline using a Si(111) double-crystal monochromator (proposal 2023A1931). A pellet of Fe0.9ß (Φ7, 54 mg) was placed in a quartz cell connected to a conventional gas flow system (total flow rate of 300 mL/min). The pellet was heated from room temperature to 350 °C at a heating rate of 20 °C/min. After reaching 350 °C, 1% N_2O/He was introduced for 900 s, followed by He purging for 300 s. Next, 1% CO/He was introduced for 900 s, followed by He purging for 300 s, and by feeding 1% N_2O/He for 900 s. During the redox treatments, XAS spectra were measured, and N_2 (m/z = 28) formation under a N_2O flow and CO_2 (m/z = 44) formation under a CO flow were analyzed by online mass spectrometry (MS). The operando XAS was repeated using the same redox treatments. Finally, after the CO reduction of the sample, XAS measurements under 10% O_2 were conducted for 900 s. The XAS results were analyzed using Athena (ver. 0.9.25) and REX2000 (ver.2.5).[49]

4.3 Results and discussion

4.3.1 Selective catalytic reduction of N_2O

We studied the catalytic activity of Fe0.9ß for the catalytic reduction of 0.1% N_2O by 0.1% CO in the presence and absence of excess (10%) O_2. Figure 1 shows the conversion of N_2O and CO under steady-state conditions at various temperatures. The results show that the selective reduction of N_2O by CO under excess O_2 is catalyzed by Fe0.9ß in the temperature range 250–500 °C. The presence of 10% O_2 resulted in a slight decrease in N_2O conversion and a slight increase in CO conversion. The mechanistic reasons for the O_2-induced slight drop in N_2O conversion and increase in CO conversion are discussed later.

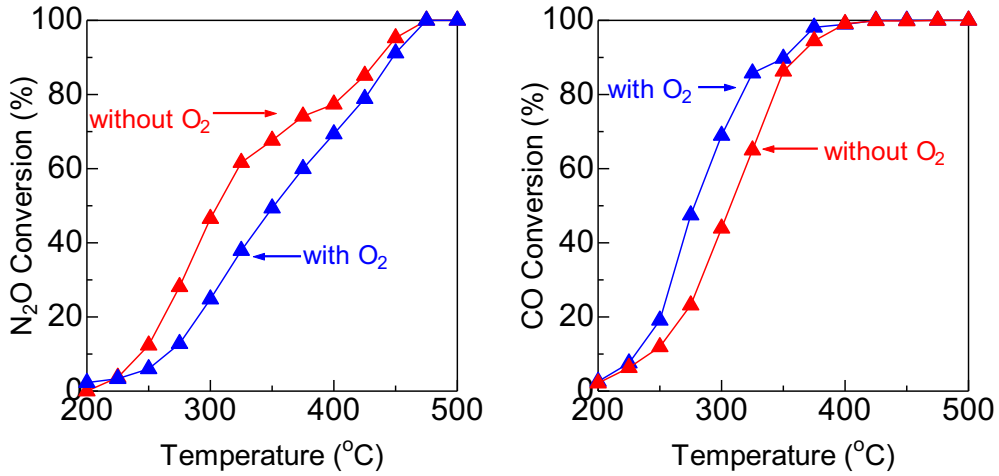

Figure 1. N_2O and CO conversion over 30 mg Fe0.9ß under 0.1% N_2O/0.1% CO/(10% O_2) versus temperature.

Figure S3 compares the catalytic activity of Fe0.9ß and Fe2.7ß for N_2O selective reduction by CO under 10% O_2. The N_2O conversion of the high Fe loading catalyst (Fe2.7ß) was slightly lower than that of the low Fe loading catalyst (Fe0.9ß), indicating that the N_2O reduction activity per Fe site is higher for the low loading catalyst.

Figure 2 compares the steady-state conversions of N_2O and CO for Fe0.9ß-catalyzed N_2O selective reduction (N_2O + CO + O_2), CO oxidation (CO + O_2), and N_2O decomposition under O_2 (N_2O + O_2) as a function of the reaction temperature. The N_2O + CO + O_2 and CO + O_2 reactions were conducted with 30 mg Fe0.9ß and the N_2O decomposition under O_2 was conducted with 150 mg Fe0.9ß. Below 450 °C, the N_2O conversions for N_2O + CO + O_2 (by 30 mg Fe0.9ß) are higher than those for N_2O + O_2 (by 150 mg Fe0.9ß), which suggests that the presence of CO as a selective reductant significantly improves the catalytic efficiency for N_2O removal. The CO conversions for CO + O_2 were similar to those for N_2O + CO + O_2. These results suggest that CO is mainly oxidized by N_2O (not by O_2) under 0.1% N_2O + 0.1% CO+ 10% O_2. CO oxidation with O_2 as a side reaction explains the lower N_2O conversion for N_2O + CO + O_2 than for N_2O + CO (Figure 1).

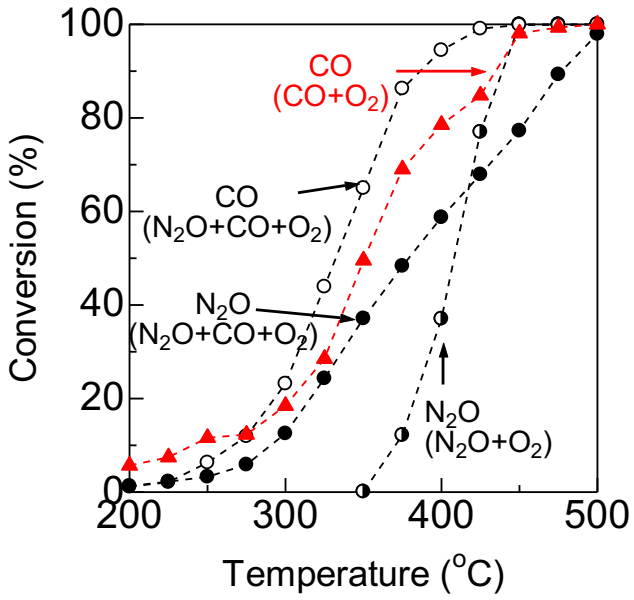

Figure 2. N_2O conversion for 0.1% N_2O + 0.1% CO + 10% O_2 over Fe0.9ß (30 mg) and 0.1% N_2O + 10% O_2 over Fe0.9ß (150 mg), and CO conversion of 0.1% CO + 10%O_2 over Fe0.9ß (30 mg) versus temperature.

To discuss the quantitative effect of CO on N_2O reduction and the reactivity of CO with N_2O or O_2, kinetic experiments were performed under the conditions in which the conversions were below 35%. Figure 3 shows the Arrhenius plots for the CO + N_2O and CO + O_2 reactions and N_2O decomposition. Note that the reaction rates were calculated based on the N_2O consumption rate for these reactions. The Arrhenius plots for the CO + N_2O and CO + O_2 reactions and N_2O decomposition gave fairly good straight lines, indicating that the apparent activation energy (Ea) can be calculated from the slope of the plot using the Arrhenius equation. The activation energy for N_2O reduction with CO (CO + N_2O; 38.2±0.6 kJ/mol) is lower than that for N_2O decomposition (98.8±4.2 kJ/mol), and the rate of N_2O reduction with CO at 300 °C is 16 times higher than that for N_2O decomposition at 300 °C. These results give quantitative evidence of the promotional effect of CO on N_2O removal over Fe0.9ß. At 300 °C, the rate of CO oxidation with 0.1% N_2O (CO + N_2O) is two times higher than the rate of CO oxidation with 10% O_2 (CO + O_2). Taking into account that the O_2 concentration is 100 times higher than that of N_2O, the result gives quantitative evidence of the significantly higher reactivity of N_2O with CO than O_2 over Fe0.9ß.

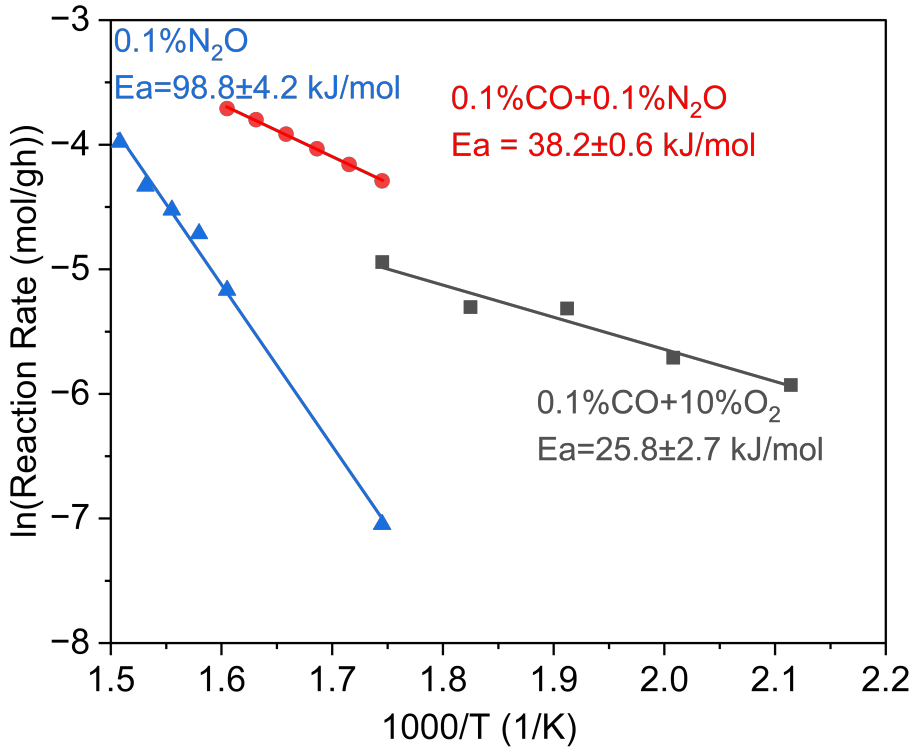

Figure 3. Arrhenius plots for CO + N_2O (150–300 °C; 5–30 mg Fe0.9ß), CO + O_2 (200–300 °C; 10–30 mg Fe0.9ß) and N_2O decomposition (300–450 °C; 75–150 mg Fe0.9ß). Activation energies (Ea) based on Arrhenius equation are shown.

For further kinetic insight, we studied the reaction order of the Fe0.9ß-catalyzed CO + N_2O + O_2 reaction at 350 °C. Figure 4 plots the rates of N_2O reduction versus the concentrations of CO, N_2O, or O_2. The reaction orders for CO, N_2O, and O_2 were estimated based on the slopes of the log–log plots. The reaction orders for CO (0.46) and N_2O (0.36) are similar and higher than that for O_2 (-0.02). The result suggests that CO and N_2O are involved in the kinetically important step of the CO + N_2O + O_2 reaction, while O_2 is not involved in the important steps.

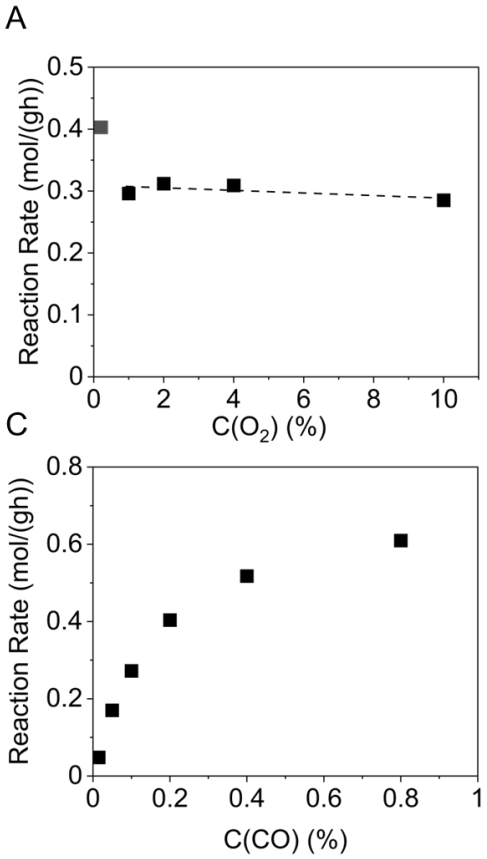

Reactant	Reaction order
CO	0.46
N_2O	0.35
O_2	-0.02

Figure 4. Reaction rates versus concentration of (A) O_2, (B) N_2O, (C) CO for CO-SCR of N_2O over Fe0.9ß at 350 °C. The reaction orders are shown in the table.

4.3.2 *In situ/operando* UV-vis

Several reported studies have provided molecular insight into the mechanism of N_2O reduction with CH_4 over Fe zeolites.[24,25,44,50] Based on spectroscopic and density functional theory evidence, Snyder et al. proposed a redox mechanism: α-Fe-O species is reduced by CH_4 to give a reduced α-Fe species, which is then re-oxidized by N_2O to regenerate the α-Fe-O species.[24,25,50] The same group reported detailed *in situ* UV-vis studies on oxidation of the α-Fe species by N_2O and assigned the broad UV-vis signal centered around 360 nm to α-Fe-O species[50].

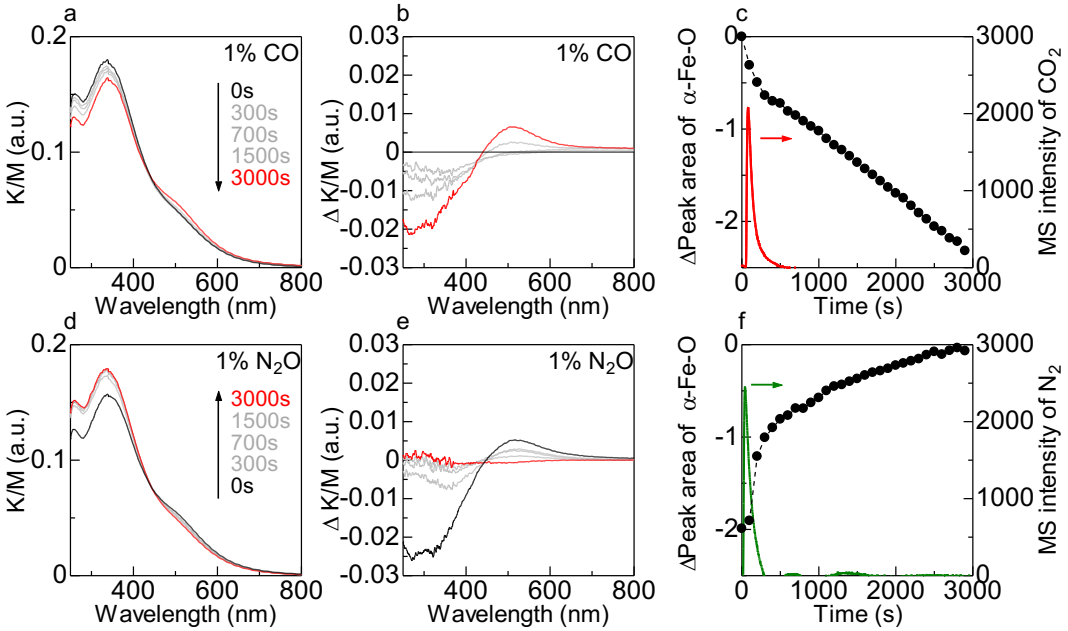

Figure 5. Selected UV-vis original spectrum of Fe0.9ß (a, d), difference spectra (b, e), and mass spectrum (MS) intensity of CO_2 or N_2 and the α-Fe-O peak area (360 nm) versus time (c, f) under 1% CO (a, b, c), followed by a He purge (for 900 s), and a flow of 1% N_2O (d, e , f) at 350 °C.

Assuming that N_2O reduction with CO over Fe0.9ß is based on this redox mechanism, we carried out *in situ* UV-vis experiments during the CO reduction of Fe0.9ß, followed by its re-oxidation by N_2O at 350 °C (Figure 5). The outlet of the *in situ* UV-vis cell was connected to an MS apparatus for online analysis of the gas-phase products. The difference spectra (Figure 5b, e) were obtained by subtracting the original spectra (left) from the initial spectrum of Fe0.9ß after pre-oxidation by 1% N_2O for 1800 s, followed by a He purge for 900 s. When the pre-oxidized Fe0.9ß was exposed to 1% CO, an unresolved negative peak centered around 360 nm assignable to the α-Fe-O species[50] appeared in the difference spectra. Deconvolution analysis of the UV-vs spectra was carried out to estimate the area of the band due to the α-Fe-O species (centered around 360 nm) using Gaussian functions. An example of the fitting results is shown in Figure S4. Figure 5c, f plots the change in peak area of α-Fe-O and the MS intensity of outlet CO_2 or N_2 as a function of time under 1% CO or 1% N_2O. The UV peak area for α-Fe-O (centered around 360 nm) increases with time. Online MS analysis indicates CO_2 formation during CO reduction of the pre-oxidized Fe0.9ß. The results

indicate that the α-Fe-O species in the pre-oxidized Fe0.9ß is reduced by CO to give CO_2. After reduction with 1% CO followed by a He purge for 900s, the reduced sample was exposed to 1% N_2O. The peak area of α-Fe-O decreased with time, and the spectrum after 3000 s was similar to the original spectrum (before CO reduction). Online MS analysis showed formation of N_2. These results suggest that N_2O reduction with CO over Fe0.9ß is based on a redox mechanism: α-Fe-O species is reduced by CO to give CO_2 and reduced Fe species, which is then re-oxidized by N_2O to regenerate the α-Fe-O species.

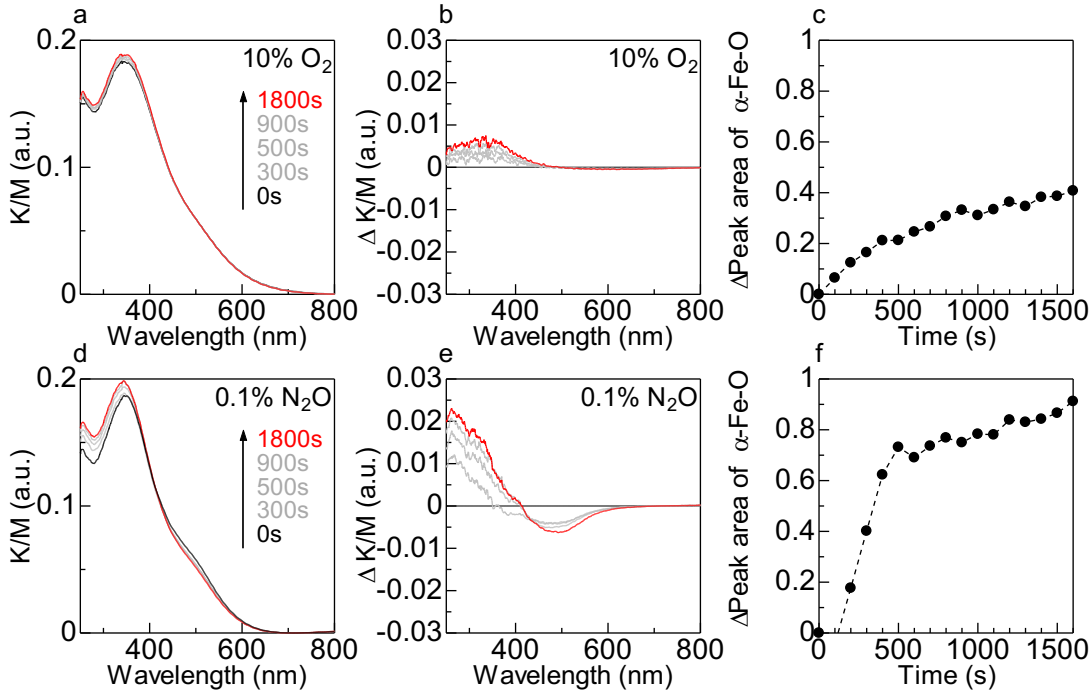

Figure 6. Selected UV-vis spectra of Fe0.9ß (a, b), difference spectra (b, e), and α-Fe-O peak area versus time (c, f) under 10% O_2 (c) or 0.1% N_2O (f) at 350 °C. The sample was pre-reduced by 1% CO for 1500 s, followed by a He purge for 900 s.

The kinetic results in Figure 3 give quantitative evidence of the higher reactivity of N_2O with CO than O_2 over Fe0.9ß. Considering the redox mechanism suggested by the above UV-vis study, we hypothesize that the reduced Fe species is oxidized by N_2O much faster than by O_2, which is the fundamental reason why Fe0.9ß catalyzes the CO + N_2O reaction under excess O_2 rather than the undesired side reaction of CO + O_2. To validate this hypothesis, we compared

kinetic curves for the re-oxidation of the reduced Fe species by 0.1% N_2O and by 10% O_2 using *in situ* UV-vis experiments on CO-reduced Fe0.9ß at 350 °C (Figure 6). The difference spectra (Figure 6b, e) were obtained by subtracting the spectra (a, d) from the initial spectrum of the CO-reduced Fe0.9ß (after reduction by 1% CO for 1500 s, followed by a He purge for 900 s). Figure 6 (c,f) plots the change in peak area of α-Fe-O. The peak at 360 nm due to the α-Fe-O species appears both under 0.1% N_2O and 10% O_2, but its formation rate is higher under 0.1% N_2O. Despite the fact that the concentration of O_2 is 100 times higher than that of N_2O, the initial rate of α-Fe-O formation under N_2O is four times higher than that under O_2. These results provide quantitative evidence of the higher reactivity of N_2O with reduced Fe species than with O_2. The higher reactivity of N_2O than O_2 for the regeneration of the α-Fe-O intermediate is the fundamental reason why the Fe0.9ß catalyst selectively promotes the CO + N_2O reaction under excess O_2 rather than the undesired side reaction of CO + O_2.

Based on the initial slopes for the kinetic plots for the CO-reduction and reoxidation, it is shown that the CO-reduction step is faster than the O_2-reoxidation step but is slower than the N_2O-reoxidation step. Hence, the CO-reduction step is the rate determining step for the CO + N_2O reaction, while the reoxidation step is the rate determining step for the CO + O_2 reaction. The lower activation energy for the CO oxidation by O_2 than that for the CO oxidation by N_2O in Figure 3 can be due to the difference in the rate determining step; the activation energy for the CO-oxidation step might be lower than those for the reoxidation steps.

4.3.3 *In situ/operando* XAS

The *in situ* UV-vis results shown above are not useful for discussing the oxidation states of the Fe species during the redox catalytic cycle. To monitor changes in the Fe oxidation state, we carried out *in situ* XAS measurements under the reduction of Fe0.9ß by 1% CO, followed by its re-oxidation by 1% N_2O at 350 °C. The outlet of the *in situ* XAS cell was connected to the MS apparatus to monitor the formation of gas-phase products. Figure 7a shows the changes in X-ray absorption near-edge structure (XANES) spectra during CO reduction. The sample was subjected to a first CO/N_2O cycle, followed by He purging for 300 s. After CO reduction for 600 s, the absorption edge was close to that of a reference compound of Fe^{2+}, $Fe_3(PO_4)_2 \bullet 8H_2O$. Figure 7b shows the spectral changes during N_2O re-oxidation of the reduced sample. Upon exposure of the sample to N_2O, the absorption edge rapidly increases. After N_2O oxidation for 450 s, the

absorption edge is close to that of the reference Fe^{3+} compound, $Fe(acac)_3$. These results suggest that the catalytic cycle for Fe0.9ß-catalyzed N_2O reduction with CO is based on the Fe^{3+}/Fe^{2+} redox couple. The energy at a normalized absorption (μ) of 0.8 was adopted to evaluate the oxidation state of the Fe species. The time dependence of the energy at μ = 0.8 and the MS intensity are shown in Figure 7 (b). Note that the edge shifts to a lower energy during the He purge after N_2O oxidation, suggesting thermal reduction of the Fe^{3+} species under He for 300 s. Then, during the CO reduction period, the energy at μ = 0.8 decreased with time, and simultaneous CO_2 formation was observed by MS. During the re-oxidation period, the energy at μ = 0.8 quickly increased within 120 s, and N_2 formation was simultaneously observed by MS. Similar kinetic results were observed in the second N_2O oxidation and CO reduction cycles (Figure S5) after the first cycle (Figure 7). The results provide direct evidence of the N_2O oxidation of Fe^{2+} to Fe^{3+} and the CO reduction of Fe^{3+} to Fe^{2+}. A comparison of the kinetic curves indicates that the N_2O oxidation of Fe^{2+} to Fe^{3+} is faster than the CO reduction of Fe^{3+} to Fe^{2+}. Combining the XANES and UV-vis results, the following mechanistic conclusions can be drawn. Fe(III)-αO (possibly Fe(III)-O^-) species are reduced by CO to yield CO_2 and reduced Fe(II) species, which are then re-oxidized by N_2O to regenerate the Fe(III)-αO species.

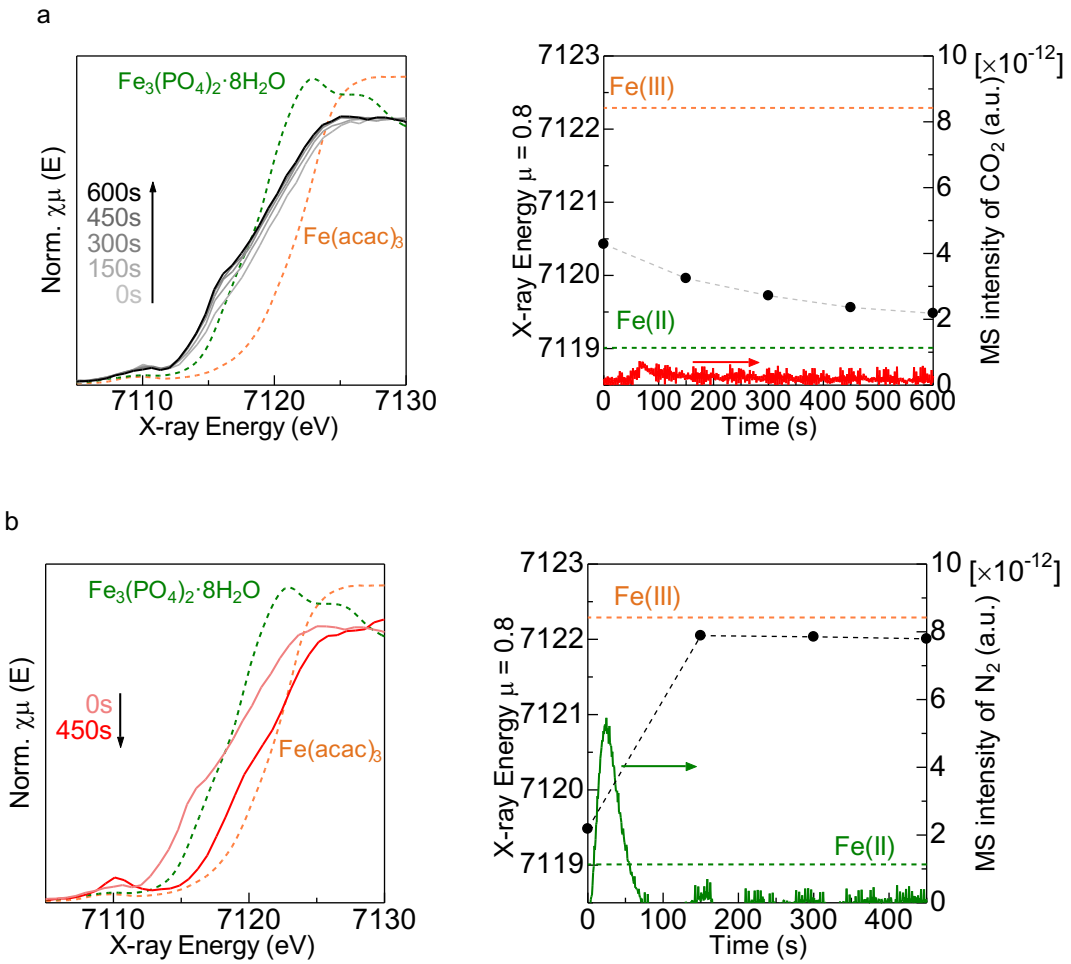

Figure 7. Evolution of the Fe K-edge XANES spectrum of Fe0.9ß during successive feeds of (a) 1% CO and (b) 1% N_2O: selected spectra (left) and energy at normalized adsorption of 0.8 and MS intensity versus time (right). Before the experiment, the pre-oxidized sample was reduced with 1% CO (950 s), followed by a He purge (300 s).

Figure 8 shows a comparison of the kinetic curves for the re-oxidation of the CO-reduced sample under 1% N_2O and 10% O_2. The slope of the re-oxidation kinetic curve under 1% N_2O is larger than that under 10% O_2. This indicates that the oxidation of Fe^{2+} under 1% N_2O is faster than that under 10% O_2, which is consistent with the UV-vis results. Combining the XANES and UV-vis results, it can be concluded that the higher reactivity of the Fe(II) species with N_2O than with O_2 for the regeneration of the Fe(III)-αO species over the CO-reduced Fe0.9ß provides a fundamental reason why Fe0.9ß selectively catalyzes the CO

+ N_2O reaction under excess O_2 rather than the undesired side reaction of CO + O_2.

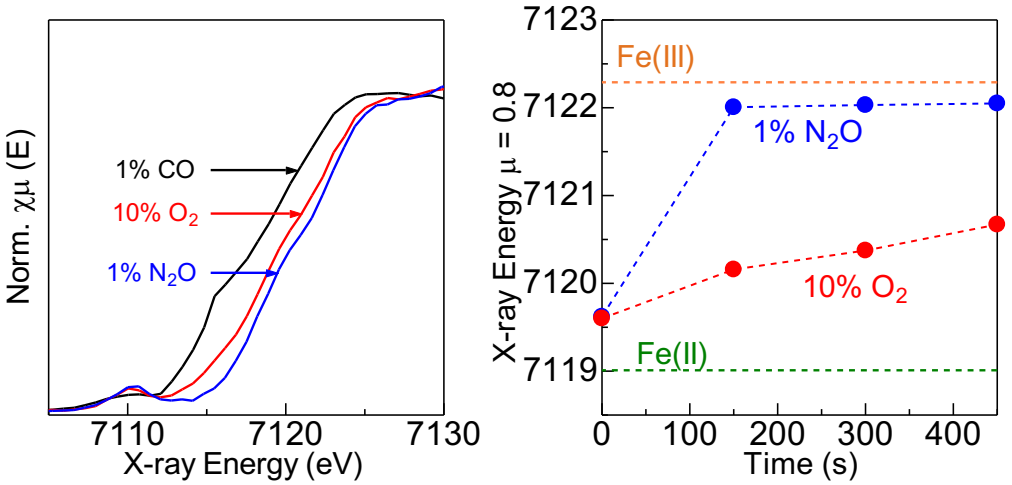

Figure 8. XANES spectra (left) of the CO-reduced Fe0.9ß, followed by re-oxidation by N_2O or O_2. Energy changes (right) at normalized absorption during re-oxidation in 1% N_2O or 10% O_2 at 350 °C.

4.4 Conclusions

Fe-exchanged ß zeolite (Fe0.9ß) effectively catalyzed the selective reduction of N_2O by CO under excess O_2. Kinetic results gave quantitative evidence for (1) a significant increase of the N_2O reduction rate by CO and (2) a significantly higher reactivity of N_2O with CO than O_2 over Fe0.9ß. Reaction order analyses showed that CO and N_2O are involved in the kinetically important steps. *Operando* UV-vis and XAS results showed a redox-based catalytic cycle; Fe(III)-αO (possibly Fe(III)-O^-) species are reduced by CO to yield CO_2 and reduced Fe(II) species, which are then re-oxidized by N_2O to regenerate the Fe(III)-αO species. Spectro-kinetic analysis provided quantitative evidence of a higher reactivity with N_2O than with O_2 for the regeneration of the Fe(III)-αO species over the CO-reduced Fe0.9ß, which provides a fundamental reason why Fe0.9ß selectively catalyzes the CO + N_2O reaction under excess O_2 rather than the undesired side reaction of CO + O_2.

4.5 References

(1) Richards, N.; Nowicka, E.; Carter, J. H.; Morgan, D. J.; Dummer, N. F.; Golunski, S.; Hutchings, G. J. *Top. Catal.* **2018**, *61* (18–19), 1983–1992.

(2) Li, Y.; Sundermann, A.; Gerlach, O.; Low, K. Bin; Zhang, C. C.; Zheng, X.; Zhu, H.; Axnanda, S. *Catal. Today* **2020**, *355*, 608–619.

(3) Jing, Y.; Taketoshi, K.; Zhang, N.; He, C.; Toyao, T.; Maeno, Z.; Ohori, T.; Ishikawa, N.; Shimizu, K. *ACS Catal.* **2022**, *12* (11), 6325–6333.

(4) Jing, Y.; He, C.; Zhang, N.; Murano, Y.; Toyoshima, R.; Kondoh, H.; Kageyama, Y.; Inomata, H.; Toyao, T.; Shimizu, K. *ACS Catal.* **2023**, *13* (19), 12983–12993.

(5) Wood, B. R.; Reimer, J. A.; Bell, A. T.; Janicke, M. T.; Ott, K. C. *J. Catal.* **2004**, *224* (1), 148–155.

(6) Wood, B. R.; Reimer, J. A.; Bell, A. T. *J. Catal.* **2002**, *209* (1), 151–158.

(7) Kim, M. J.; Kim, Y. J.; Lee, S. J.; Ryu, I. S.; Kim, H. J.; Kim, Y.; Ko, C. H.; Jeon, S. G. *Chem. Eng. Res. Des.* **2019**, *141*, 455–463.

(8) Wang, S.; Yan, B.; Chai, J.; Li, T.; Yu, H.; Li, T.; Cao, P.; Yang, F.; Yuan, X.; Yin, H. *Eur. J. Inorg. Chem.* **2021**, *2021* (23), 2201–2210.

(9) Moreau, C.; Caravaca, Á.; Vernoux, P.; Gil, S. *ChemCatChem* **2020**, *12* (11), 3042–3049.

(10) Pietrogiacomi, D.; Campa, M. C.; Carbone, L. R.; Occhiuzzi, M. *Appl. Catal., B* **2019**, *240*, 19–29.

(11) Kameoka, S.; Yuzaki, K.; Takeda, T.; Tanaka, S. I.; Ito, S. I.; Miyadera, T.; Kunimori, K. *Phys. Chem. Chem. Phys.* **2001**, *3* (2), 256–260.

(12) Zhang, X.; Shen, Q.; He, C.; Ma, C.; Cheng, J.; Li, L.; Hao, Z. *ACS Catal.* **2012**, *2* (4), 512–520.

(13) Nobukawa, T.; Yoshida, M.; Kameoka, S.; Ito, S. I.; Tomishige, K.; Kunimori, K. *J. Phys. Chem. B* **2004**, *108* (13), 4071–4079.

(14) Nobukawa, T.; Sugawara, K.; Okumura, K.; Tomishige, K.; Kunimori, K. *Appl. Catal., B* **2007**, *70* (1–4), 342–352.

(15) Zeng, J.; Wang, Y.; Diao, F.; Qiu, L.; Chang, H. *Catal. Surv. Asia* **2021**, *25*, 58–67.

(16) You, Y.; Chen, S.; Li, J.; Zeng, J.; Chang, H.; Ma, L.; Li, J. *J. Hazard. Mater.* **2020**, *383* (121117).

(17) Pacultová, K.; Obalová, L.; Kovanda, F.; Jirátová, K. *Catal. Today* **2008**,

137 (2–4), 385–389.

(18) Campa, M. C.; Pietrogiacomi, D.; Catracchia, C.; Morpurgo, S.; Olszowka, J.; Mlekodaj, K.; Lemishka, M.; Dedecek, J.; Kornas, A.; Tabor, E. *Appl. Catal., B* **2024**, *342*.

(19) Campa, M. C.; Pietrogiacomi, D.; Scarfiello, C.; Carbone, L. R.; Occhiuzzi, M. *Appl. Catal., B* **2019**, *240*, 367–372.

(20) Kiwi-Minsker, L.; Bulushev, D. A.; Renken, A. **2005**; Vol. 110, pp 191–198.

(21) Mlekodaj, K.; Lemishka, M.; Kornas, A.; Wierzbicki, D. K.; Olszowka, J. E.; Jirglová, H.; Dedecek, J.; Tabor, E. *ACS Catal.* **2023**, *13* (5), 3345–3355.

(22) Yoshida, M.; Nobukawa, T.; Ito, S. I.; Tomishige, K.; Kunimori, K. *J. Catal.* **2004**, *223* (2), 454–464.

(23) Zhao, G.; Chodyko, K.; Benhelal, E.; Adesina, A.; Kennedy, E.; Stockenhuber, M. *J. Catal.* **2021**, *400*, 10–19.

(24) Bols, M. L.; Hallaert, S. D.; Snyder, B. E. R.; Devos, J.; Plessers, D.; Rhoda, H. M.; Dusselier, M.; Schoonheydt, R. A.; Pierloot, K.; Solomon, E. I.; Sels, B. F. *J. Am. Chem. Soc.* **2018**, *140* (38), 12021–12032.

(25) Snyder, B. E. R.; Vanelderen, P.; Bols, M. L.; Hallaert, S. D.; Böttger, L. H.; Ungur, L.; Pierloot, K.; Schoonheydt, R. A.; Sels, B. F.; Solomon, E. I. *Nature* **2016**, *536* (7616), 317–321.

(26) Vitillo, J. G.; Bhan, A.; Cramer, C. J.; Lu, C. C.; Gagliardi, L. *ACS Catal.* **2019**, *9* (4), 2870–2879.

(27) Nobukawa, T.; Yoshida, M.; Okumura, K.; Tomishige, K.; Kunimori, K. *J. Catal.* **2005**, *229* (2), 374–388.

(28) Debbagh, M. N.; Lecea, C. S. M. de; Pérez-Ramírez, J. *Appl. Catal., B* **2007**, *70* (1–4), 335–341.

(29) Li, G.; Pidko, E. A.; Van Santen, R. A.; Feng, Z.; Li, C.; Hensen, E. J. M. *J. Catal.* **2011**, *284* (2), 194–206.

(30) Fellah, M. F.; Van Santen, R. A.; Onal, I. *J. Phys. Chem. C* **2009**, *113* (34), 15307–15313.

(31) Delahay, G.; Mauvezin, M.; Guzm, A.; Coq, B. *Catal. Commun.* **2002**, *3* (8), 385–389.

(32) Guzmán-Vargas, A.; Delahay, G.; Coq, B. *Appl. Catal., B* **2003**, *42* (4), 369–379.

(33) Wang, A.; Wang, Y.; Walter, E. D.; Kukkadapu, R. K.; Guo, Y.; Lu, G.; Weber, R. S.; Wang, Y.; Peden, C. H. F.; Gao, F. *J. Catal.* **2018**, *358*, 199–210.

(34) Zhang, X.; Shen, Q.; He, C.; Ma, C.; Cheng, J.; Hao, Z. *Catal. Commun.*

2012, *18*, 151–155.
(35) Mauvezin, M.; Delahay, G.; Kißlich, F.; Coq, B.; Kieger, S. *Catal. Lett.* **1999**, *62*, 41–44.
(36) Coq, B.; Mauvezin, M.; Delahay, G.; Butet, J.-B.; Kieger, S. *Appl. Catal., B* **2000**, *27*, 193–198.
(37) Boutarbouch, M. N. D.; Cortés, J. M. G.; Begrani, M. S. El; Lecea, C. S. M. De; Pérez-Ramírez, J. *Appl. Catal., B* **2004**, *54* (2), 115–123.
(38) Pérez-Ramírez, J.; Kumar, M. S.; Brückner, A. *J. Catal.* **2004**, *223* (1), 13–27.
(39) Dai, C.; Lei, Z.; Wang, Y.; Zhang, R.; Chen, B. *Microporous Mesoporous Mater.* **2013**, *167*, 254–266.
(40) Fischer, G.; Goursot, A.; Coq, B.; Delahay, G.; Pal, S. *ChemPhysChem* **2006**, *7* (8), 1795–1801.
(41) Kameoka, S.; Nobukawa, T.; Tanaka, S. I.; Ito, S. I.; Tomishige, K.; Kunimori, K. *Phys. Chem. Chem. Phys.* **2003**, *5* (15), 3328–3333.
(42) Dubkov, K. A.; Ovanesyan, N. S.; Shteinman, A. A.; Starokon, E. V.; Panov, G. I. *J. Catal.* **2002**, *207* (2), 341–352.
(43) Gokce, I.; Ozbek, M. O.; Ipek, B. *J. Catal.* **2023**, *427*.
(44) Mahyuddin, M. H.; Shiota, Y.; Staykov, A.; Yoshizawa, K. *Inorg. Chem.* **2017**, *56* (17), 10370–10380.
(45) Guo, M.; Zhou, S.; Sun, X. *J. Phys. Chem. Lett.* **2023**, *14* (6), 1633–1640.
(46) Zasada, F.; Gryboś, J.; Budiyanto, E.; Janas, J.; Sojka, Z. *J. Catal.* **2019**, *371*, 224–235.
(47) Liu, C.; Kubota, H.; Amada, T.; Kon, K.; Toyao, T.; Maeno, Z.; Ueda, K.; Ohyama, J.; Satsuma, A.; Tanigawa, T.; Tsunoji, N.; Sano, T.; Shimizu, K. *ChemCatChem* **2020**, *12* (11), 3050–3059.
(48) Kubota, H.; Toyao, T.; Maeno, Z.; Inomata, Y.; Murayama, T.; Nakazawa, N.; Inagaki, S.; Kubota, Y.; Shimizu, K. *ACS Catal.* **2021**, *11* (17), 11180–11192.
(49) Yasumura, S.; Qian, Y.; Kato, T.; Mine, S.; Toyao, T.; Maeno, Z.; Shimizu, K. I. *ACS Catal.* **2022**, *12* (16), 9983–9993.
(50) Bols, M. L.; Snyder, B. E. R.; Rhoda, H. M.; Cnudde, P.; Fayad, G.; Schoonheydt, R. A.; Van Speybroeck, V.; Solomon, E. I.; Sels, B. F. *Nat. Catal.* **2021**, *4* (4), 332–340.

Supporting information

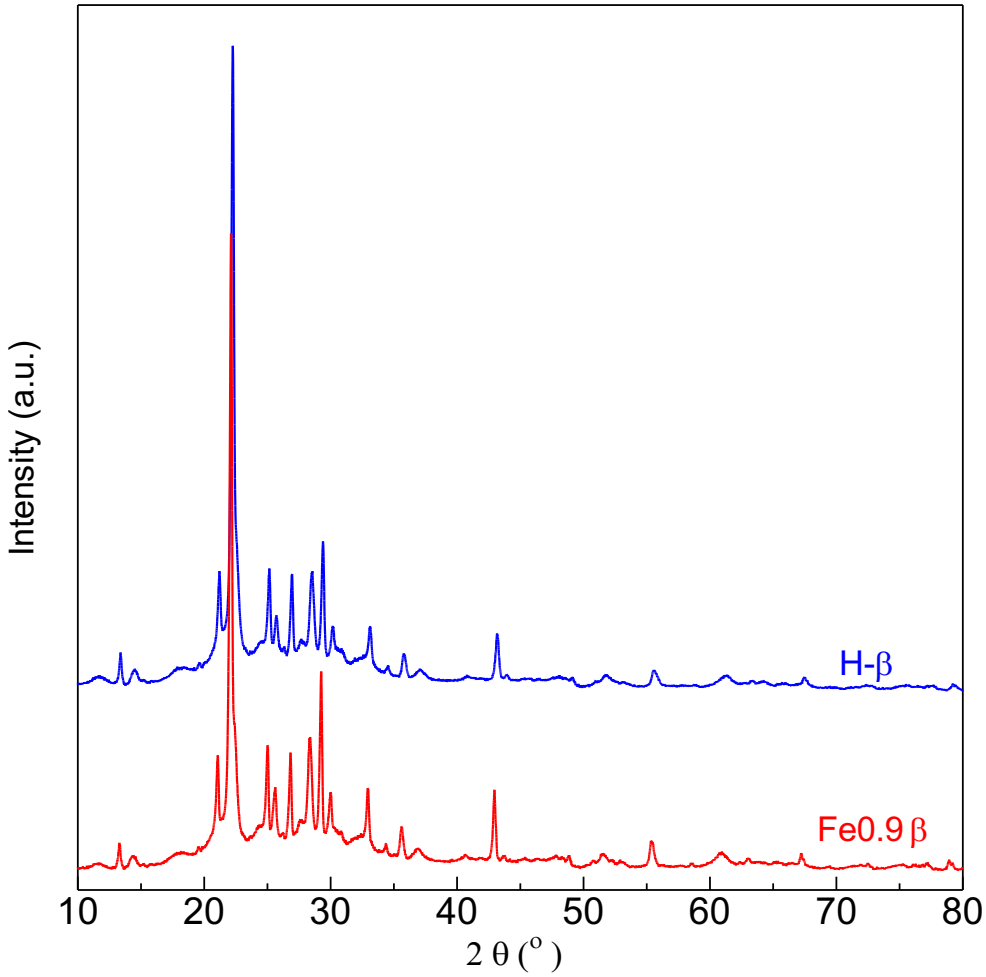

Figure S1. XRD patterns of H-β (600°C, 1h, air calcination) and Fe0.9β (as made).

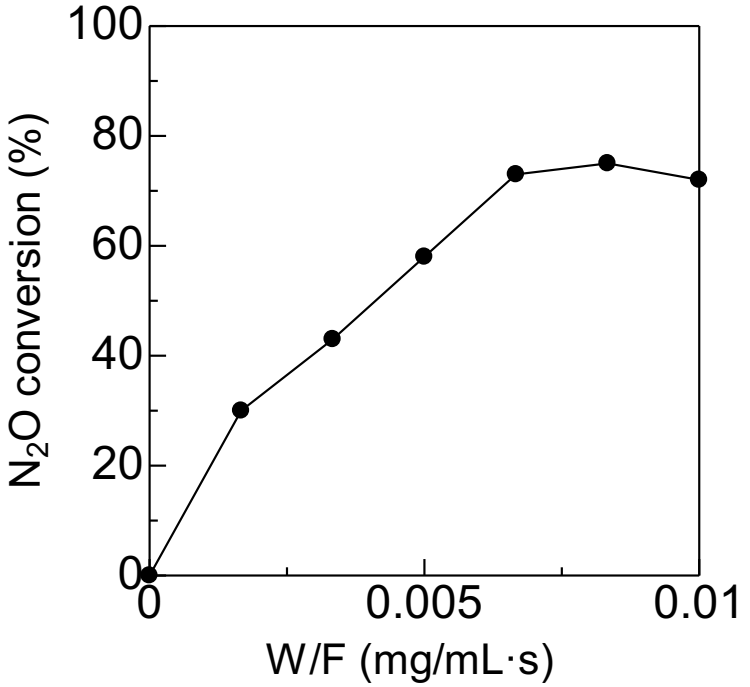

Figure S2. N_2O conversion depending on the weight/flow (contact time). Total flow 100mL/min, 350 °C, 0.1% N_2O/0.1% CO/10% O_2/ He, m(catalyst)=0-60mg.

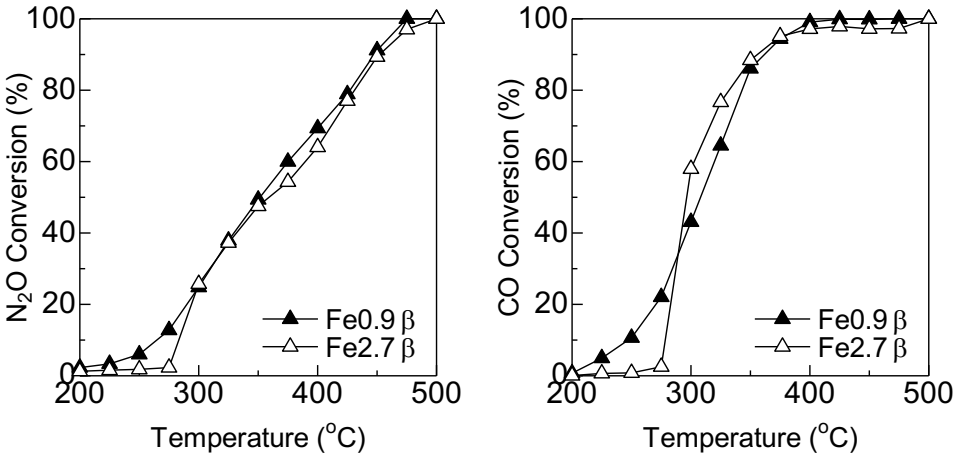

Figure S3. N_2O and CO conversion under 0.1% N_2O/0.1% CO/10% O_2 over 30 mg Fe2.7ß and Fe0.9ß versus temperature.

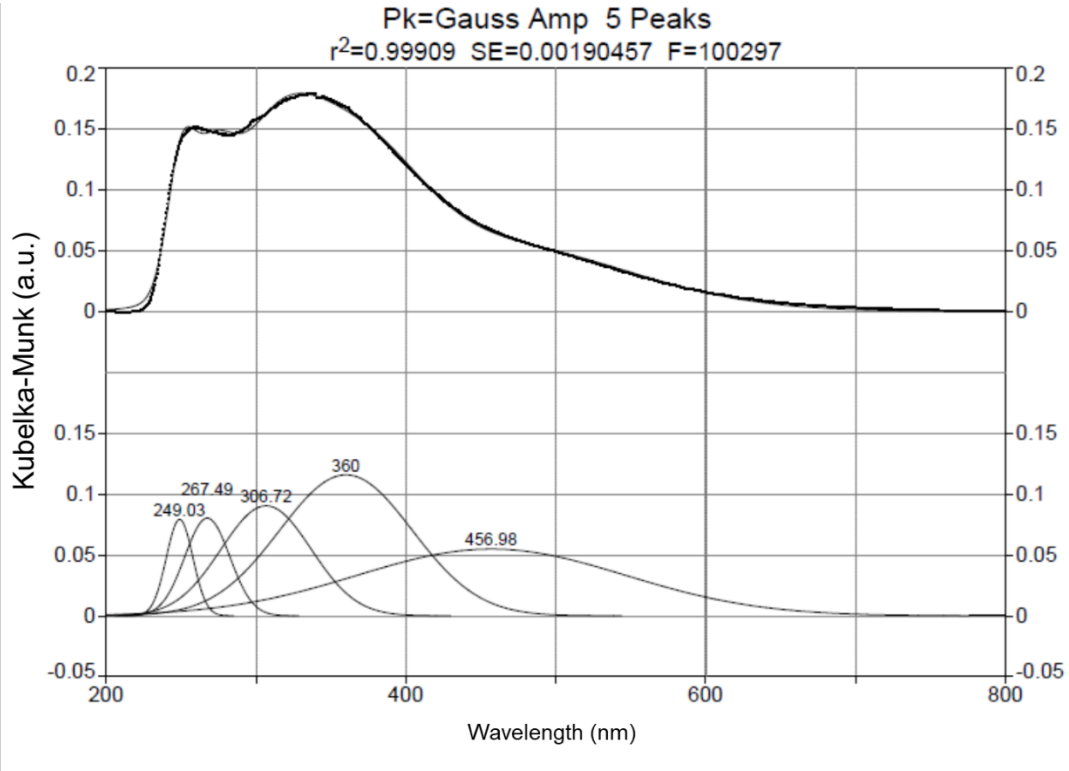

Figure S4. Gaussian peak separation result of a representative UV-vs spectrum (after re-oxidation by N_2O for 3000 s). The peak at 360 nm is due to Fe-αO. The position of each peak was fixed for all spectra.

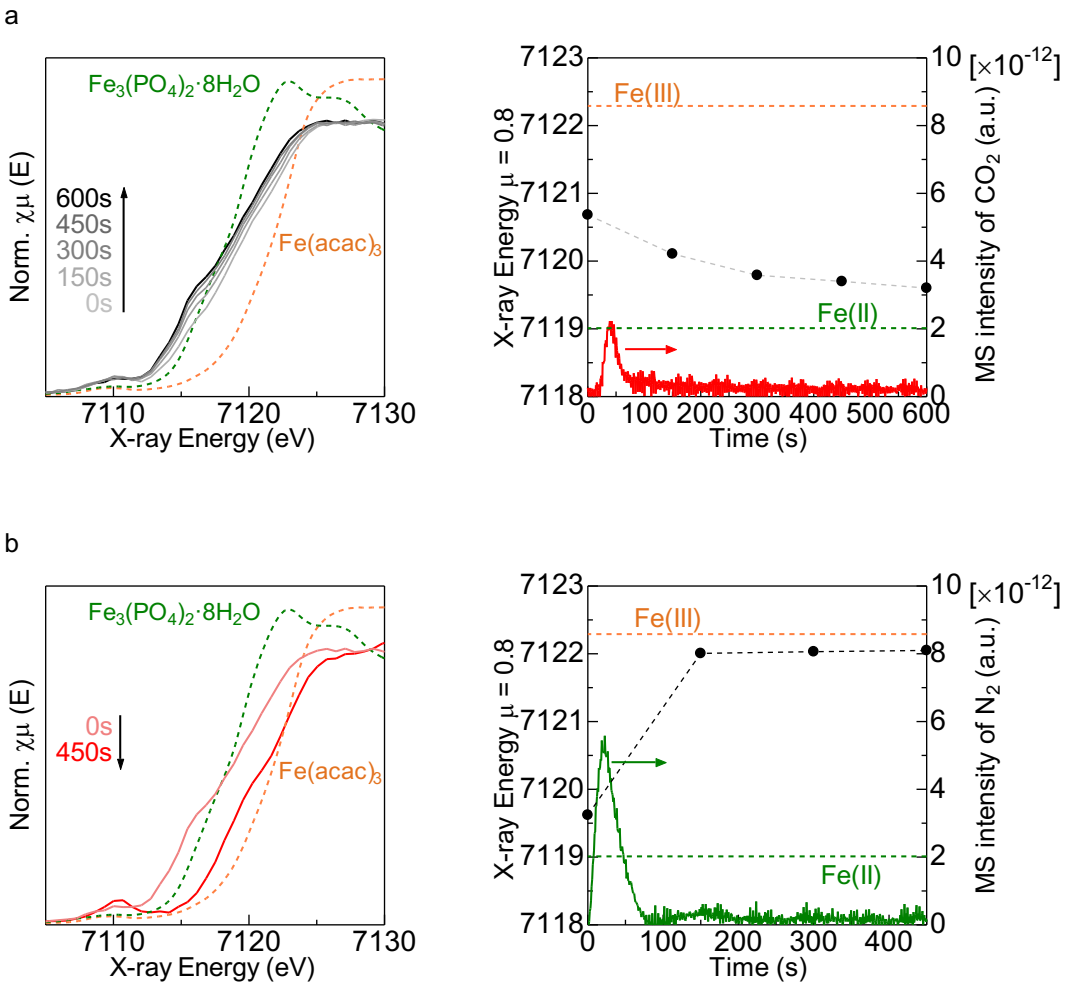

Figure S5. Evolution of the Fe K-edge XANES spectra of Fe0.9ß during successive feeds of (a) 1% CO and (b) 1% N_2O: selected spectra (left) and energy at normalized adsorption of 0.8 and MS intensity versus time (right) after the first cycle in Figure 8.

Chapter 5

General Conclusion

In this thesis, selective catalytic reduction of nitrogen oxides (NOx) and N_2O using different reducing agent (NH_3 and CO) with exceed existence of O_2 has been studied. And by applying *in situ/operando* spectroscopies, the underlying mechanisms are revealed for rational design of novel SCR catalysts and development of *in situ/operando* spectroscopic methods.

Chapter 2 concludes that Density functional theory (DFT) calculations indicate that catalyst-free oxidation of NO by O_3 proceeds readily at room temperature, yielding NO_2 at an O_3/NO ratio of 0.5, whereas higher oxidant ratios (>0.5) favor the formation of N_2O_5 via pathways with very low activation barriers (≈2 kJ mol^{-1}). Complementary *in situ/operando* FTIR measurements show that exposing Cu-CHA to 0.16% NO + 0.08% O_3 at 100 °C leads to efficient NOx storage as nitrate species bound to Cu^{2+} sites, which subsequently react with NH_3 to generate N_2 and NH_4NO_3; above 200 °C, the accumulated NH_4NO_3 further reacts with NO to produce N_2. NH_3 adsorbed on Cu-CHA is also oxidized by excess O_3 (0.7%), yielding N_2 and N_2O below 150 °C with a characteristic N_2O/N_2 ratio of 0.75, whereas lower O_3 levels (0.08%) suppress both oxidation rates to <100 ppm. Moreover, oxidation of adsorbed NH_3 by NO + O_3 selectively forms N_2 at low temperature (<150°C). These combined mechanistic insights provide a foundation for engineering unsteady-state lean deNOx strategies that exploit the controlled desorption and reaction of stored NOx with NH_3, or the reduction of NOx using captured NH_3 species.

Chapter 3 concludes that Under the employed reaction conditions, SO_4^{2-} and $S_2O_7^{2-}$ are identified as the predominant surface sulfate species on the catalyst. Mechanistically, Ce^{4+}–(OH^-) ensembles, likely positioned in proximity to these sulfate groups, undergo reduction by NO and NH_3 to generate N_2 and H_2O while forming Ce^{3+} sites, establishing the reduction half-cycle. Modulation-excitation spectroscopy (MES) resolves this half-cycle as initiating with NO activation on Ce^{4+}–(OH^-) to produce an NO^+ intermediate, followed by Ce^{3+} formation and concomitant release of gaseous HONO. The transient HONO is rapidly trapped by NH_3, proceeding through NH_4NO_2 intermediates to yield N_2 and H_2O. The resulting Ce^{3+} species are subsequently reoxidized by O_2, thereby closing the oxidation half-cycle and completing a sulfate-tuned Ce^{4+}/Ce^{3+} redox loop that drives low-temperature NO reduction.

Chapter 4 concludes that Fe-exchanged ß zeolite (Fe0.9ß) exhibits high efficiency for the selective reduction of N_2O by CO even under O_2-rich conditions.

Steady-state kinetics provide quantitative evidence that CO markedly accelerates N_2O reduction, and that N_2O reacts with CO substantially more readily than O_2 over Fe0.9ß. Reaction-order analysis further demonstrates that both CO and N_2O participate directly in the kinetically relevant elementary steps. In situ/operando UV–vis and XAS collectively reveal a redox-driven catalytic cycle in which Fe(III)–αO species (likely Fe(III)–O^-) are reduced by CO to produce CO_2 and Fe(II), followed by preferential reoxidation of Fe(II) by N_2O to regenerate Fe(III)–αO. Spectro-kinetic quantification confirms that regeneration of Fe(III)–αO by N_2O proceeds faster than by O_2 on CO-reduced Fe0.9ß, providing a mechanistic basis for the observed selectivity toward CO + N_2O conversion while suppressing the competing CO oxidation pathway in excess O_2.

To summarize this thesis, by utilizing in situ/operando and modulation excitation spectroscopies and computational science, the thesis provides a molecular-level insight into the SCR mechanism of lean deNOx catalysts and N_2O abatement catalysts. This will propose a novel guidance for the design of reaction path and catalysts at a much more fundamental, molecular, level in the field and makes a significant contribution to heterogenous catalytic chemistry and environmental catalysis.

Acknowledgement

Firstly, I would like to express gratitude to my supervisor Professor Ken-ichi Shimizu for guiding in an excellent way during my study and supervising the research so that we could achieve our goals. He gives me not only fundamental background of *in situ/operando* spectroscopies but also serves as a paragon, demonstrating the attitude of a true scientist. I would like to acknowledge the opportunity to study in Japan as a Ph.D. student.

Next, I want to thank Professor Takashi Toyao and Professor Akihiko Anzai for their help, suggestions and guidance.

I am truly grateful to all the staff and laboratory member in Shimizu Group for the kind help on the daily experiment. I would like to be thankful to Dr. Shunsaku Yasumura, Dr. Yuan Jing, Dr. Feilong Xing, Dr. Shinya Mine Dr. Kenichi Kon and Mr. Wataru Onodera for their kindness in assisting this thesis and invaluable suggestion and the great help to complete this work. I also would like to thank all other members and alumni of Prof. Shimizu's laboratory.

I would like to acknowledge the Advance Graduate School and EXEX Doctoral Fellowship of Hokkaido University for giving the precious opportunity and financial support to gain PhD degree in Institute for Catalysis, Faculty of Chemical Science and Engineering.

Last, but not least, I would like to thank my family especially my parents and all my dear friends whom I could not mention for always standing beside me to get through the ups and down.